

X-ray emitting young stars in the Orion Nebula

Eric D. Feigelson¹, Patrick Broos¹, James A. Gaffney III¹, Gordon Garmire¹, Lynne A. Hillenbrand², Steven H. Pravdo³, Leisa Townsley¹, Yohko Tsuboi¹

ABSTRACT

The Orion Nebula Cluster and the molecular cloud in its vicinity have been observed with the ACIS-I detector on board the *Chandra X-ray Observatory* with 23 hours exposure in two observations. We detect 1075 X-ray sources, most with sub-arcsecond positional accuracy. Ninety-one percent of the sources are spatially associated with known stellar members of the cluster, and an additional 7% are newly identified deeply embedded cloud members. This provides the largest X-ray study of a pre-main sequence stellar population and covers the initial mass function from brown dwarfs up to a 45 M_{\odot} O star. Source luminosities span 5 orders of magnitude from $\log L_x \simeq 28.0$ to 33.3 erg s^{-1} in the 0.5 – 8 keV band, plasma energies range from 0.2 to >10 keV, and absorption ranges from $\log N_H < 20.0$ to $\sim 23.5 \text{ cm}^{-2}$. Comprehensive tables providing X-ray and stellar characteristics are provided electronically.

We examine here the X-ray properties of Orion young stars as a function of mass; other studies of astrophysical interest will appear in companion papers. Results include: (a) the discovery of rapid variability in the O9.5 31 M_{\odot} star $\theta^2 A$ Ori, and several early B stars, inconsistent with the standard model of X-ray production in small shocks distributed throughout the radiatively accelerated wind; (b) support for the hypothesis that intermediate-mass mid-B through A type stars do not themselves produce significant X-ray emission; (c) confirmation that low-mass G- through M-type T Tauri stars exhibit powerful flaring but typically at luminosities considerably below the ‘saturation’ level; (d) confirmation that the presence or absence of a circumstellar disk has no discernable effect on X-ray

¹Department of Astronomy & Astrophysics, 525 Davey Laboratory, Pennsylvania State University, University Park PA 16802

²Department of Astronomy, MS 105-24, California Institute of Technology, Pasadena CA 91125

³Jet Propulsion Laboratory, MS 306-438, 4800 Oak Grove Drive, Pasadena CA 91109

emission; (e) evidence that T Tauri plasma temperatures are often very high with $T \geq 100$ MK, even when luminosities are modest and flaring is not evident; and (f) detection of the largest sample of pre-main sequence very low mass objects showing flaring levels similar to those seen in more massive T Tauri stars and a decline in magnetic activity as they evolve into L- and T-type brown dwarfs.

Subject headings: open clusters and associations: individual (Orion Nebula Cluster) – stars:activity – stars: early-type – stars: low mass, brown dwarfs – stars: pre–main–sequence – X-rays: stars

1. Introduction

Two decades ago, the first imaging X-ray telescope pointed at nearby star forming regions and discovered X-ray emission from low-mass pre-main sequence (PMS) stars at levels far above those seen from typical main sequence stars (Feigelson & DeCampi 1981; Feigelson & Kriss 1981; Walter & Kuhi 1981; Montmerle et al. 1983). Initially seen in T Tauri stars with roughly solar masses and characteristic ages of $\sim 10^6$ yr, the X-ray excess was later found to extend from protostars with ages $\sim 10^4 - 10^5$ yr (Koyama et al. 1996) to post-T Tauri stars with ages $\sim 10^7$ yr (Walter et al. 1988), and from substellar masses (Neuhäuser et al. 1999) to intermediate-mass Herbig Ae/Be stars (Zinnecker & Preibisch 1994) as well as high-mass OB stars (Harnden et al. 1979). The typical PMS star was found to have X-ray luminosities $10^1 - 10^4$ above those typically seen in older main sequence stars. The hot plasma temperatures in the range 0.5–5 keV and frequent high amplitude variability on timescales of hours suggested that the strong X-ray emission was due to elevated levels of magnetic reconnection flaring rather than a quiescent coronal process.

The Orion Nebula (= Messier 42), a blister HII region on the near edge of the Orion A giant molecular cloud, is illuminated by the richest PMS stellar cluster in the nearby Galaxy. Known variously as the Orion Id OB association, the Trapezium and the Orion Nebula Cluster (ONC), it has > 2000 stellar members with masses ranging from $< 0.05 M_{\odot}$ to nearly $50 M_{\odot}$ OB stars in the Trapezium (Hillenbrand 1997; Hillenbrand & Carpenter 2000). The ONC is a unique laboratory where the entire initial mass function of a young stellar cluster can be examined in a uniform fashion by an imaging X-ray telescope. While star formation appears to have ceased in the ONC itself ~ 1 Myr ago, the molecular cloud behind the ONC is actively forming stars with dozens of likely protostars both around the Becklin-Neugebauer object (Gezari et al. 1998) and elsewhere in the cloud (Lada et al. 2000).

The ONC was the first star forming region to be discovered in the X-ray band with

non-imaging instruments (Giacconi et al. 1972; den Boggende et al. 1978; Bradt & Kelley 1979) which found that the emission was extended. But these early observations could not discriminate whether the X-rays were produced by the Trapezium OB stars, the lower-mass T Tauri stars or a diffuse plasma. Observations with the *Einstein*, *ROSAT* and *ASCA* satellites resolved dozens of individual stars (e.g. Ku & Chanan 1979; Pravdo & Marshall 1981; Gagné et al. 1995; Geier et al. 1995; Yamauchi et al. 1996), but could identify X-rays from only a modest fraction of the cluster population due to sensitivity, resolution and bandwidth limitations. Due to crowding and absorption by the molecular material, high-resolution X-ray imaging at energies > 2 keV is critical for the study of the ONC and other rich star forming regions. The *Chandra X-ray Observatory* provides these capabilities and gives a greatly improved view of the ONC field (Garmire et al. 2000).

While the X-rays from low-mass T Tauri stars are recognized to arise from magnetic reconnection flares, a variety of astrophysical questions remain concerning the origins of X-ray emission as a function of stellar mass. Among young massive OB stars, *Einstein* and *ROSAT* investigations found that X-ray luminosity scales with the bolometric luminosity as $L_x \propto 10^{-7} L_{bol}$ for stars earlier than B1.5 (Harnden et al. 1979; Pallavicini et al. 1981; Berghöfer et al. 1997). The X-ray emission mechanism here is thought to be quite different from that in lower mass PMS stars, produced in shocks arising from instabilities in their radiatively driven stellar winds (e.g. Lucy & White 1980; Owocki & Cohen 1999). As these high-mass stars generally exhibited little X-ray variability, the emission was generally interpreted to arise in a myriad of little shocks, although the possibility of high-amplitude variations from large shocks is discussed by Feldmeier, Puls, & Pauldrach (1997). Recent *Chandra* and *XMM-Newton* grating spectroscopic studies confirm the basic scenario of X-ray production in the extended wind with broadened lines produced at different depths within the wind (Waldron & Cassinelli 2001; Schulz et al. 2000; Kahn et al. 2001), although evidence is growing that magnetically confined hot plasma either near the surface or in the wind plays a significant role (Babel & Montmerle 1997; Waldron & Cassinelli 2001).

The nature of the transition between OB wind-generated X-rays and T Tauri flare-generated X-rays has not been well-established. Late B and A type stars have neither strong winds nor outer convective zones where magnetic fields may be amplified by dynamo processes, and are thus predicted to be X-ray quiet. Nonetheless, a substantial number of these stars have been detected with a wide range of X-ray luminosities (Schmitt et al. 1985; Caillault & Zoonematkermani 1989; Berghöfer & Schmitt 1994a; Simon, Drake, & Kim 1995; Cohen, Cassinelli, & Macfarlane 1997). Much, but perhaps not all, of this emission can be attributed to the presence of low-mass T Tauri star companions to the intermediate mass stars. The X-ray emission is often stronger from the youngest intermediate-mass stars, Herbig Ae/Be stars, which exhibit accretion and outflows from their circumstellar disks

(Zinnecker & Preibisch 1994). In at least one case, high-amplitude flaring is clearly present (Hamaguchi et al. 2000).

The magnetic flaring model of X-ray emission from lower mass T Tauri stars has been generally interpreted as enhanced solar-type activity where fields generated by a magnetic dynamo in the stellar interior erupt and undergo violent reconnection at the stellar surface (e.g. reviews by Walter & Barry 1991; Feigelson, Giampapa, & Vrba 1991; Feigelson & Montmerle 1999). This solar activity model is supported by extensive multiwavelength evidence of enhanced chromospheric lines, rotationally modulated cool starspots, photospheric Zeeman measurements, and circularly polarized radio continuum flares in T Tauri stars. However, in support of arguments for a magnetic coupling between PMS stars and their circumstellar disks, the X-ray flares (particularly in protostars) have been alternatively attributed to reconnection in long star-disk magnetic field lines (e.g. Shu et al. 1997; Montmerle et al. 2000). The astrophysical processes giving rise to PMS magnetic fields are also uncertain. Possibilities include a standard $\alpha - \omega$ dynamo as in main sequence stars, a turbulent dynamo particular to fully convective stars, fossil fields inherited from the star forming process, or dynamo processes in the circumstellar disk. Addressing these open issues regarding the origins of the enhanced X-ray emission from PMS stars is a principal goal of the present effort. Feigelson & Montmerle (1999) give a comprehensive review of both the observational evidence and theoretical interpretations of magnetic flaring in lower mass PMS stars.

A handful of the lowest mass objects in young stellar clusters, PMS brown dwarfs, have been detected in the X-ray band at the limit of sensitivity of the *ROSAT* and *Chandra* satellites (Neuhäuser et al. 1999; Garmire et al. 2000; Imanishi, Koyama & Tsuboi 2001; Preibisch & Zinnecker 2001). One nearby older brown dwarf has also been seen with *Chandra* during a flare (Rutledge et al. 2000), and another object exhibited a powerful flare in the optical band (Liebert et al. 1999). Their X-ray behavior appears qualitatively similar to that seen in PMS stars, which is consistent with the expectation that the internal conditions of PMS brown dwarfs do not differ much from the conditions within PMS M-type stars.

The present paper is the second in a series based on *Chandra* observations with the ACIS detector obtained during the first year of the *Chandra* mission. Garmire et al. (2000, Paper I) gave an overview of the initial exposure and discussed the nature of sources in the Becklin-Neugebauer/Kleinman-Low region. The present study analyzes the full dataset (§2), presenting comprehensive tables and notes of individual source properties and counterparts (§3), providing a global X-ray view of the young stellar population (§4), and examining the X-ray properties of young stars across the initial mass function (§5). Paper III (Feigelson et al. 2002a) focuses on the magnetic activity of $\simeq 1 M_{\odot}$ analogs of the PMS Sun and discusses the implications for energetic particle radiation onto solar nebula solids as evidenced in ancient

meteorites. Paper IV (Feigelson et al. 2002b) discusses the absence of the relationship between X-ray emission and stellar rotation expected from a solar-type magnetic activity and dynamo model. Paper V (Gaffney et al., in preparation) presents detailed spectral and variability studies of the brightest ONC sources. The reader is also referred to *Chandra* ONC studies using the ACIS spectroscopic array (Schulz et al. 2000, 2001) rather than the ACIS imaging array used here.

2. Observations and data analysis

2.1. Instrumental setup

The ONC was observed with the Advanced CCD Imaging Spectrometer (ACIS) detector on board the *Chandra X-ray Observatory* (Weisskopf et al. 2001) on 12 October 1999 and 1 April 2000 (Table 1). The two images are shown at low resolution in Figure 1a and b. The principal results arise from the imaging array (ACIS-I) which consists of four abutted 1024×1024 -pixel front-side illuminated charge-coupled devices (CCDs) specially designed for X-ray studies⁴. Each CCD chip subtends $8.3'$ and, after chip gaps and satellite dithering are taken into account, the ACIS-I image covers about $17' \times 17'$ on the sky. The aimpoint of the array for both observations is $5^h35^m15.0^s$, $-5^\circ23'20''$ (J2000), $22''$ west of the brightest member of the Trapezium, $\theta^1\text{C Ori}$.

The instrument configuration during the two observations differed in a number of respects. First, the focal plane temperature was -110°C during the October 1999 observation, but was reduced to -120°C before the April 2000 observation. Consequently, the earlier observation suffers a higher charge transfer inefficiency (CTI) during readout of the CCD chips every 3.2 s. The CTI of the front-side illuminated ACIS chips deteriorated early in the *Chandra* mission due to charged particle bombardment during passage through the Earth's magnetospheric radiation belts (Prigozhin et al. 2000). Second, the satellite roll angle rotated by 183° between the two observations, resulting in an offset of the arrays and different orientations of the readout trailed events.

In addition to the ACIS-I data, the S2 and S3 chips in the spectroscopic array (ACIS-S) were also operational. These data are less useful: the telescope point spread function (PSF) is considerably degraded far off-axis; the chips cover different regions of the Orion cloud due to the roll angle change; the chips differ in background levels and CTI characteristics due to

⁴Detailed descriptions of the ACIS instrument and its operation can be found on-line at <http://www.astro.psu.edu/xray/docs/sop> and <http://www.astro.psu.edu/xray/docs/calreport>.

their construction (S3 is back-side illuminated while S2 is front-side illuminated); and the S3 chip suffered a hardware failure during the October 1999 observation (FEP0 electronics board problem). The ACIS-S results will not be reported here.

2.2. Exposure times

The satellite was pointed at the ONC for about 26 hours during the two observations (Table 1). Time series were generated to locate periods of missing or bad data. The October 1999 dataset suffered many brief periods of missing data due to the saturation of the telemetry by false events generated by the FEP0 electronics failure. We use the exposure averaged over the entire array in the analysis here and ignore the $\sim 1\%$ scatter in chip-dependent exposures. The April 2000 observation had only 6.4 s of telemetry dropouts and was thus a virtually uninterrupted datastream.

Two other exposure time corrections are applied. First, exposures are reduced by 1.3% because 0.04 s of each 3.24 s frame was devoted to chip readout, during which source photons appear as faint readout trails parallel to the chip axis. The readout trails for the brightest Trapezium stars are clearly evident in the images. Second, 1.5% (1.0%) of the time was eliminated due to software-generated glitches in the aspect solution in the October (April) datasets. With these corrections, the net exposure time averaged over the array is about 23 hours (Table 1).

The effective exposure time for a given source at some distance from the aimpoint is this array-averaged exposure time corrected for telescope vignetting, for chip-dependent telemetry dropouts and, for sources lying near chip edges, for satellite dithering motions that move the source on and off the chip. Thus, each source is accompanied by an independently calculated effective exposure time which is incorporated into the auxiliary response file (arf) generated for each source during spectral analysis (§2.8).

2.3. Data selection

Our data analysis starts with Level 1 processed event lists provided by the pipeline processing at the *Chandra* X-ray Center, which includes all events telemetered by the ACIS detector. The earlier dataset was processed with ASCDS version R4CU4 in October 1999, and the later dataset with ASCDS version R4CU5UPD2 in April 2000. Our data reduction methodology uses codes and functionalities provided by a variety of software systems: the CIAO package (version 1.0 and 2.0, <http://asc.harvard.edu/ciao>) for *Chandra* data analy-

sis produced by the *Chandra* X-ray Center at the Smithsonian Astrophysical Observatory; FTOOLS programs for FITS file manipulation produced by the HEASARC at NASA Goddard Space Flight Center (version 5.0, heasarc.gsfc.nasa.gov/docs/software/ftools/ftools_menu.html); the TARA package for interactive ACIS data analysis developed by the ACIS Team at Pennsylvania State University (version 5.8, <http://www.astro.psu.edu/xray/docs>); and the ds9 data visualization application developed at Smithsonian Astrophysical Observatory (version 1.9, <http://hea-www.harvard.edu/RD/ds9>). Technical notes on the software procedures used here can be found at <http://www.astro.psu.edu/xray/axaf/recipes>.

We first removed an artificial random offset of $\pm 0.25''$ introduced to the location of each event during Level 1 processing, as it produces an unnecessary blurring of the point spread function. Second, the energy and grade of each event was corrected with a procedure that models the CTI characteristics of each chip (Townsend et al. 2000, 2002). This not only corrects the trend of decreasing gain as one proceeds from the edge towards the center of each chip, but also accounts for changes in splitting of charge between adjacent pixels due to CTI. An important effect of the latter correction is the improvement in signal and reduction in noise at high energies towards the center of the ACIS-I array, particularly for the first observation obtained at -110°C .

Two cleaning operations were conducted to remove spurious events from the image. First, a temporal cleaning operation was conducted to remove ‘cosmic ray afterglows’ produced by high energy Galactic cosmic rays. Although the charge deposited immediately after a cosmic ray hit is almost always rejected by on-board processing, in some cases the central pixel will release residual charge over 10 – 30 s. We consider the arrival of two or more events at the same chip pixel within 30 sec to be the signature of afterglows. When these spurious charges resemble X-ray hits, they are included in the telemetry as real events. While these constitute only $\simeq 2\%$ of the background events in a typical ACIS-I observation, they can combine with ordinary background events to produce spurious weak sources. A sensitive source detection algorithm can find up to dozens of spurious sources due to cosmic ray afterglows if they are not removed.

However, two or more photons from celestial sources will sometimes arrive at the same chip pixel within 30 sec by chance. (Recall that the distribution of times between adjacent events of a Poisson process decreases exponentially with the lag time, so the probability of closely spaced events is not small.) Examination of the spatial distribution of events flagged as cosmic ray afterglows indicates that 2% – 10% of counts are flagged from real sources in the Orion field with intensities ranging from 0.001 – 0.2 counts s^{-1} . We found that the incorrect removal of these true source photons can be avoided by removing only flagged events lying more than $3''$ from identified sources.

Second, ‘hot columns’ of spurious events are removed. These arise from several flickering pixels in both the imaging and framestore regions of the CCD chips, and cosmic ray hits in the frame store area along amplifier boundaries. The location and grade classifications of these false events are known and are easily removed. Third, we select events by their ‘grades’ and their energy to remove most of the remaining events arising from charged particles and detector noise. We choose events that exhibit ‘standard *ASCA* grades’ (0, 2, 3, 4 and 6) after CTI correction and events outside the energy range 0.5 – 8.0 keV are eliminated. Fourth, the two exposures were merged into a single image after positional alignment, as described in §2.5.

The images resulting from this data selection procedure are shown in Figure 1 for the two individual exposures, and in Figures 2-3 for the merged field. The background levels are very low (except near the very bright Trapezium stars). On average, there is only one background event in a $3'' \times 3''$ region in the merged image (Table 1).

2.4. Source detection

Sources were located in the image using a wavelet transform detection algorithm implemented as the *wavdetect* program within the CIAO data analysis system (Dobrzycki et al. 1999; Freeman et al. 2002). We found that the default threshold probability of 1×10^{-6} omitted a considerable number of weak sources having stellar counterparts, while noise frequently triggered the algorithm for a threshold of 1×10^{-4} . Because of the highly crowded field and the elevated background in the central region of the ONC, the simulation that showed that a threshold probability of 1×10^{-6} gives one false detection per 10^6 pixels (Freeman et al. 2002) is inapplicable. We therefore opted to use a threshold of 1×10^{-5} and to examine each *wavdetect* source by hand, as described below.

The *wavdetect* program is very successful in detecting sources down to faint count limits across the entire ACIS array, despite the changes in PSF and variations in background due to chip gaps or overlapping arrays. However, failures or errors of several types occasionally occur. First, when the threshold is set to obtain maximum sensitivity near the field center, some false triggers of noise occur far off axis. In particular, we find that a Poissonian upward fluctuation in background noise adjacent to a downward fluctuation sometimes produces a false trigger. Second, the program sometimes consolidates closely spaced sources easily resolved by eye; this failure begins for source separations $\leq 2.5''$ on-axis. Third, the program naturally triggers spurious sources on read-out trails of strong sources. Fourth, as the source detection (in contrast to source consolidation) is done without knowledge of the varying PSF, the algorithm can locate sources smaller than the point spread function far off-axis or

larger than the PSF near the axis. Fifth, the sensitivity to sources rapidly deteriorates as one approaches within $\sim 2'$ of θ^1 C Ori due to the elevation of background from the O star's PSF wings. Sixth, as with any source detection algorithm, performance near the detection threshold is erratic and the eye can locate untriggered faint concentrations similar to those that were triggered. Seventh, *wavdetect* computes the source counts in a cell region which is not accurately scaled to the local PSF. Off-axis photometry obtained by *wavdetect* is thus not always reliable.

We address most of these problems by careful visual inspection of the image with the locations of *wavdetect* sources marked. Sources which appear spurious (clearly noise or read-out trails) are omitted, marginal sources are flagged in the table notes, and missing sources (close doubles and marginal sources missed by the algorithm) are added⁵. Several dozen sources were adjusted in some way; these adjustments are explained in the table notes. A final examination was made of sources with extracted counts (§2.6) very close to the estimated background level. None of these decisions was based on the presence or absence of counterparts at other wavelengths.

The result of this entire source detection process is 1075 sources for the merged Orion ACIS-I field, which are illustrated in Figure 3 and tabulated in Table 2.

2.5. Source positions and stellar counterparts

The *wavdetect* software provides an estimate of the source position using a simple average of event positions in pixels in its source region, where the conversion between pixel and celestial locations is based on the satellite aspect solution. These celestial locations can be further corrected to match the stellar *Hipparcos* frame of reference by associating ACIS sources with stars of known position. We proceeded as follows:

Boresight alignment An absolute translational error is frequently present in the *Chandra* aspect solution at a level around $1'' - 2''$. For the present dataset, this boresight error was corrected using twenty-two sources with > 200 counts in each exposure, lying in the inner $3'$ of the field, and having an unambiguous optical or near-infrared counterpart. We found that the October 1999 field required a translation of $0.6''$ to the SE and the April 2000 field required a translation of $1.9''$ to the NE to match the stellar positions in the 2MASS/ACT/Tycho reference frame (Hillenbrand & Carpenter 2000). When the *wavdetect*

⁵The following sources were added by hand: #148, 189, 202, 223, 241, 382, 384, 408, 420, 454, 504, 609, 614, 842 and 862.

positions from the merged image are considered, the residual offsets of the optical and X-ray positions have a standard deviation of only $0.1''$, so the formal uncertainty of the frame alignment is only $0.1/\sqrt{22-1} = 0.02''$. The alignment was later checked using $\simeq 600$ ACIS/optical positional comparisons lying within $4'$ of the field center, and was found to be excellent.

Stellar counterparts After the exposures were aligned and merged, source positions were obtained from *wavdetect* then compared to a catalog of confirmed or likely ONC members. This catalog consists of several thousand stars based on a complete $V < 20$ ONC sample (Hillenbrand 1997; Hillenbrand et al. 1998, with positions corrected in Hillenbrand & Carpenter 2000), a deep *JHK* survey of the inner $5' \times 5'$ (Hillenbrand & Carpenter 2000), and a 2MASS variability survey of the region (Carpenter et al. 2001). All ACIS/star associations with offsets $\phi < 5''$ were initially considered. Outliers with large offsets were individually examined, and were typically found to have multiple counterparts, weak X-ray sources below the completeness limit, or positions far off-axis where the PSF is broad. About 50 cases of multiple counterparts were found, typically two members of a visual binary lying within $1'' - 2''$ of an ACIS source. We generally associated the source with the brighter member of the binary, but recognize that this may be incorrect in some cases and may produce a bias in later study (e.g. a $L_x - L_{bol}$ correlation plot). These cases are noted in table footnotes. For sources without counterparts in the catalogs listed above, we also searched the USNO A-2.0, 2MASS survey and SIMBAD databases. Two new photospheric counterparts (a 2MASS survey source and the mid-infrared source IRc5) and 1 new radio counterpart were found.

After culling unreliable sources and flagging multiple counterparts, we find that 755 (70% of 1075) ACIS sources have $V < 20$ counterparts (Prosser et al. 1994; Hillenbrand 1997, 604 of these are in the early lists of Parenago 1954 and/or Jones & Walker 1988), 218 (20%) have *JHK* but no optical counterparts (Hillenbrand & Carpenter 2000; Carpenter et al. 2001), 1 has only a mid-infrared counterpart, and 101 (9%) have no photospheric counterpart. The sources with no counterparts will be discussed in detail in Section 4.1.

Astrometric accuracy The *wavdetect* centroid can, in principle, produce systematically incorrect positions for off-axis sources due to anisotropies in the *Chandra* mirror PSF. For example, a point source $5' - 10'$ off-axis will exhibit both a $2''$ asymmetric cusp and a $5'' - 10''$ elliptical halo whose orientation depends on location in the detector (see Figure 4.9, *Chandra* POG 2000). It is difficult to predict the amplitude of this systematic error, as the asymmetries may be partially erased by the merging of two exposures with opposite roll angles and by wavelet processing.

Figure 4 shows the offset ϕ between ACIS and stellar positions as a function of off-axis

angle θ ⁶. Potential matches falling to the left of the dashed line were rejected as false. In the inner region where the PSF is flat and constant in shape, the median offsets are quite small: $0.25''$ for $\theta < 1'$ rising to $0.5''$ around $\theta \simeq 4'$. However, the mean offset, and scatter about that mean, increase considerably as θ increases to $8' - 12'$ such that offsets of $2'' - 5''$ are not uncommon towards the edge of the field. Matches with $\phi > 3''$ were carefully considered; any ambiguity in the source identification is noted with an ‘id’ flag in Table 2. While some of the largest offsets can be attributed to very weak off-axis sources where the centroid is strongly affected by background contamination, half of the 15 sources with $\phi > 3''$ contain > 1000 counts.

Systematic trends in the offsets are seen. Specifically, the Star–ACIS offset in right ascension runs from $\simeq -1''$ near the NE corner of the field to $\simeq +1''$ near the SW corner. Similarly, the Star–ACIS offset in declination runs from $\simeq -1''$ near the NW corner to $\simeq +1''$ near the SE corner. These systematic offsets have two possible causes: a 0.083% error in the ACIS pixel size (not recognized until late-2001), and an interaction between the wavelet transform and asymmetries in the off-axis PSF. We have not attempted to correct these positions here.

2.6. Photon extraction

We extract counts for source analysis from circular regions centered on *wavdetect* source positions. The extraction of source photons in an optimal and reproducible way is not simple due to the non-Gaussian shape and strong variation in the PSF across the field. The behavior of the *Chandra* PSF as one proceeds off-axis is complex: the shape is nearly circular and centrally condensed in the inner $\theta < 5'$, but broadens rapidly with increasing asymmetries for $5' < \theta < 12'$. The PSF core and wing components do not evolve homologously so that the curves of full-width half maximum and various encircled energy fractions (e.g., 50%, 95%) as a function of off-axis angle are not parallel. Extraction from a large region (e.g. the radius enclosing 99% of the PSF) guarantees capture of more source photons but also includes more background events which, for weak off-axis sources, can dominate the signal. Extraction from a small region reduces background effects but loses events that can improve statistics in later spectral and variability analysis. In any case, the estimate of the source flux must account both for the loss of events from the PSF wings and the addition of background events.

⁶Throughout this study, we calculate θ from θ^1 C Ori rather than the aimpoint of the *Chandra* mirrors, which differ by $0.3'$. This permits correction for the high background caused by the wings of its PSF.

For most sources, we chose to extract events from the 95% encircled energy radius as a function of off-axis angle, based on the PSF of a 1.49 keV monochromatic source⁷. For very bright sources with > 1000 counts, the extraction radius was increased to around the 99% curve, as the benefit of increased source photons exceeds the increase in background. The radius was reduced below the 95% curve for nearly 200 sources principally due to source crowding. For each source, we extract counts C_{xtr} in the total 0.5 – 8 keV band from within radius R_{xtr} . These are the events used in all later spectral and variability analysis. For all cases, we calculate the corresponding PSF fraction f_{PSF} using the CIAO program `mkpsf`. The resulting distribution of extracted counts as a function of off-axis angle is shown in Figure 5.

The number of background counts in the extraction circle is estimated to be

$$B_{xtr} = B(\theta) \times \pi R_{xtr}^2 \quad (1)$$

where B is in counts (arcsec)⁻², R_{xtr} is in arcsec, and off-axis angle θ is in arcmin. This background level is approximately constant over most of the ACIS field with the values given in Table 1. In the inner $\theta < 3'$ the background is substantially elevated by the PSF wings of $\theta^1\text{C Ori}$. We estimate that $\sim 450,000$ photons were incident onto the detector from $\theta^1\text{C Ori}$; the next brightest sources are ~ 20 times fainter and their PSF wings are much less important (see §2.10). Background levels were measured manually at several dozen source-free locations in the inner region and an empirical fit to the wings of the $\theta^1\text{C Ori}$ point spread function gives

$$\begin{aligned} \log B(0.1' < \theta < 1.0') &= 0.6\theta^{-0.6} - 2.0, \\ \log B(1.0' < \theta < 3.0') &= -0.25\theta - 1.15. \end{aligned} \quad (2)$$

Note that this background fit is not very accurate in the inner $\theta < 0.5'$ as the steep slope to the $\theta^1\text{C Ori}$ PSF, wings and readout trails from other strong sources, and the slightly displaced chip gaps from the two observations together produce spatial variations in the background levels. Despite these complications, the background is relatively unimportant for the great majority of ONC sources.

⁷These 95% encircled energy radii were calculated using the CIAO program `mkpsf` and are consistent with those obtained with the detailed raytraces using the SAOSAC model for the *Chandra* mirror assembly (P. Zhao, private communication). The radius in arcsec is reasonably well-approximated by the quadratic function $R(95\%EE) = 2.05 - 0.55\theta + 0.18\theta^2$, where θ is the off-axis angle in arcmin. The 99% encircled energy radii used for bright sources is approximately $R(99\%EE) = 8 + 0.2\theta$ and the 50% radii used for nondetections in §2.12 is approximately $R(50\%EE) = 0.43 - 0.10\theta + 0.050\theta^2$.

The count rate CR for each source can be calculated from

$$CR(\text{ct ks}^{-1}) = (C_{xtr} - B_{xtr}) / (f_{PSF} E_{eff}) \quad (3)$$

where the effective exposure time E_{eff} is given in Table 1. Except for sources near the detector edges, $E_{eff} = 82.8$ ks. Confidence intervals of these count rates are dominated by statistical uncertainties of the extracted counts when $C_{xtr} < 500$ counts. Systematic uncertainties in the other quantities are estimated to be 5% or less and dominate for the strongest sources.

2.7. Variability analysis

Lightcurves were constructed for all sources. For the stronger sources, binsizes were chosen to give roughly 20 bins in the lightcurve. An extraordinary variety of behaviors were found including: constant sources; constant within each observation but different between observations (~ 6 months separation); slowly variable within one or both observation, consistent perhaps with rotational modulation of longitudinal structures on the stellar surface; and rapidly variable phenomena reminiscent of magnetic reconnection flares on the Sun and other late-type stars. The reader can view examples of such variations in our companion study of PMS solar analogs (Feigelson et al. 2002a) and in the ACIS-S study by Schulz et al. (2001).

No simple quantity for tabulation adequately describes the variety of phenomenology seen. The non-parametric Kolmogorov-Smirnov test, for example, does not provide a consistent distinction between variable and constant sources because of the 10^4 range in count rates and 10^1 range in accessible timescales. Parametric modeling that accounts for each source’s counting statistics, such as Bayesian Block models (Scargle 1998), would be useful but are beyond the scope of this study.

We thus provide only the average count rates in each of the two observations and a simple subjective classification of the variations. Lightcurves illustrating the four classes are shown in Figure 6:

Constant The source is approximately constant in all available observations, though for weak sources this is not a strong constraint.

Long-term variation No variation is seen within an observation, but the average count rates in the October 1999 and April 2000 observations differ at the $> 3\sigma$ level of significance; that is,

$$|(C_{xtr}(Oct) - 1.2C_{xtr}(Apr))| > 3\sqrt{C_{xtr}(Oct) + 1.2^2C_{xtr}(Apr)}, \quad (4)$$

where the constant 1.2 is the ratio of the exposure times (Table 1). Note that most sources designated ‘Flare’ or ‘Possible flare’ also show long-term variation.

Possible flare A variation is seen within an observation, but with lower signal-to-noise ratio so that quantitative descriptions are not readily obtained. Notes are not provided in most cases.

Flare A highly significant variation on timescales of hours is present within one or both observations. In these cases, the lightcurve is briefly described in a note to Table 3. When the entire event lies within the observation, the note gives peak count rate CR_p , quiescent CR_q , rise and decay timescales. However, often the events extend beyond the ~ 12 hour exposures and only partial information is available. A wide variety of flare morphologies are seen – there is no ‘typical’ flare.

2.8. Spectral analysis and absorption estimates

The spectrum of each source was evaluated by fitting simple optically thin thermal plasma models to the pulse height distribution of the extracted photons. Background contribution and variability were ignored in the fitting procedure. These omissions, combined with the diversity of observed spectra and both systematic and statistical instrumental uncertainties, mean that this spectral analysis quite likely does not reflect the complexity of the astrophysical phenomena. We therefore limit our objectives here to a basic measurement of the time-averaged temperature(s) of the emitting plasma, an estimate of the intervening interstellar column density from the soft X-ray absorption, and evaluation of time-averaged broad-band fluxes and luminosities. For the faintest sources, our objectives are further limited to a single estimate of luminosity.

Spectral fitting was performed using the XSPEC code (Arnaud 1996), version 10, assuming a uniform plasma with 0.3 times solar elemental abundances. Continuum and emission line strengths were evaluated using the MEKAL code (Mewe 1991); soft X-ray absorption was modeled using atomic cross-sections of (Morrison & McCammon 1983). The choice of sub-solar abundances was based on fits of *ASCA* CCD-resolution spectra of PMS stars (Tsuboi et al. 1998; Hamaguchi et al. 2000; Tsuboi et al. 2000, see however Kastner et al. 1999 for a case with solar abundances). Best-fit models were found by χ^2 minimization by comparing models with extracted events in the range 0.5 – 8 keV. The events are grouped into bins of 5 photons (except for the weakest sources). Free parameters of the model are the plasma energy kT , equivalent hydrogen column density of absorbing interstellar material $\log N_H$, and a normalization factor adjusting the model to the total count rate. Astrophysical

models are convolved with an auxiliary response file (arf) describing the telescope and ACIS detector effective area as a function of energy and location in the detector, and a response matrix file (rmf) describing the spectral resolution of the detector as a function of energy. The arf file includes source-specific reductions in exposure times due to off-axis telescope vignetting and (for a few sources) the effects of chip gaps or bad CCD columns convolved with satellite aspect dithering.

A problem arises here: only standard arf and rmf files from CIAO version 2 were available at the time of this analysis, which do not take into account the improvements in gain correction, hard-band sensitivity, and spectral resolution provided by the CTI correction applied to the individual events (§2.3). This discrepancy is evident in XSPEC plots comparing source and model spectra; for example, in strong sources, the data have sharper line features than the models and the data–model residuals show corresponding correlations. A potentially important source of systematic bias in the spectral fits is our use of standard CIAO curves of quantum efficiency *vs.* photon energy (incorporated into the arf files) which do not take into account the improved recovery of hard energy photons from our CTI correction procedure. This can result in overestimation of plasma energies at high temperatures. The importance of this bias is difficult to evaluate, as it is significant only for the October 1999 observation obtained with detector temperature -110°C and for sources near the detector center. Altogether, the spectral results reported here thus cannot be considered definitive and further analysis with improved calibration methods is warranted. The broad-band luminosities (§2.9) are not significantly affected by these problems.

After construction of weighted average arf and rmf files from -110°C and -120°C calibration, each source spectrum was fitted with an isothermal plasma with interstellar absorption. Satisfactory fits to the broad-band shape of the spectrum were obtained for about 80% of the sources using this one-temperature plasma fit. A two-temperature plasma model was introduced for spectra with poor fits, which gave satisfactory results for about 10% of the sources. However, although the model fits were adequate, the two-temperature results were sometimes astrophysically unrealistic: a very strong soft component ($E \sim 0.2$ keV) would sometimes be introduced with a high absorption incompatible with the known visual absorption of the star. We thus do not report the N_H values from two-temperature fits, and warn that the two-temperature kT values may not accurately reflect the astrophysical plasma.

The model fits for some sources were still poor for two reasons. First, additional broad-band components, usually a soft (< 1 keV) excess or a hard (> 4 keV) excess, were sometimes present which were not included in the model. This usually occurred because the value of χ^2 for the overall fit was satisfactory despite an apparent misfit of the spectral shape. In such

cases, mentioned individually in the notes to Table 3, the derived broad-band luminosities will be systematically underestimated. Second, the broad-band spectral shape may be well-modeled but narrow spectral features in emission or absorption appear in the data that are not present in the model. The lines can be attributed to a variety of ionized elements (e.g., neon, silicon, sulfur, argon, iron) and may arise from plasmas with unusual elemental abundances. For example, recent spectral studies of flares in magnetically active stars in the solar neighborhood using the *XMM-Newton* satellite show dramatic variations in neon and iron abundances on timescales of hours during magnetic flares (Brinkman et al. 2001; Güdel et al. 2001; Drake et al. 2001). From visual inspection of the spectra and source–model residuals, we have flagged about 15% of the sources as likely cases of plasma with narrow spectral features. Note that, in some of these cases, the plasma abundances may prove to be normal when improved arf/rmf calibration files and spectral models are used.

The individual kT and N_H values for weak sources are unreliable: they have large statistical uncertainty, and sometimes more parameters than independent spectral bins. Sources with $C_{xtr} < 30$ are omitted from scientific analysis. The reported spectral fits for faint sources, however, are not meaningless. For these faint sources, the χ^2 fitting process give a solution that passes exactly through the binned spectrum ($\chi^2 = 0.0$). The solutions represent non-unique spline-like fits to the event energy distribution, and are thus useful for the calculation of broad-band X-ray luminosities. We report the spectral parameters in the tables, even for these faint sources, so that future researchers can reproduce our luminosity values, even though the fit parameters are not individually reliable for astrophysical analysis.

The derived spectral parameters inherit a statistical uncertainty, and perhaps a bias, from the χ^2 fitting process. We therefore performed several thousand simulations with sources of known spectra and differing count rates to estimate the statistical uncertainties of $\log N_H$, kT and the broad-band luminosities (§2.9). We used the *fakeit* utility in the XSPEC package for simulations with $20 \leq \log N_H \leq 22.5 \text{ cm}^{-2}$, $1 \leq kT \leq 10 \text{ keV}$, and $10 \leq C_{xtr} \leq 1000$ counts. The results show a systematic tendency for the fitting process to systematically underestimate the energies of $kT = 10 \text{ keV}$ sources by $\simeq 10\%$ (1000 cts) to $\simeq 50\%$ (30 cts). Two effects may contribute to this bias: the sparse photon population of the uppermost channels due to the rapid decline in telescope effective area at high energies; and the incompatibility between the CTI-corrected data and the uncorrected arf/rmf files used here. Another bias occurs when $\log N_H$ values are below $\simeq 20.5 \text{ cm}^{-2}$. The fitted values are often ill-determined in these cases because we consider data only above 0.5 keV.

The statistical uncertainties of spectral parameters are estimated as follows from these simulations. The standard deviations of fitted plasma energy values range roughly from $\Delta(kT)/kT \simeq 60\%$ (30 cts) to 30% (100 cts) and 10% (1000 cts). Column density uncer-

tainties range from $\Delta(\log N_H) \simeq 0.7$ (30 cts) to 0.3 (100 cts) and 0.1 (1000 cts). Due to the nonlinearity of the models and data, correlated errors are naturally present. Broad-band luminosity values $\log L_t$ exhibit standard deviations ranging from 35% (10 cts) to 25% (30 cts), 15% (100 cts) and 4% (1000 cts). These are only somewhat larger than the optimal $\sqrt{C_{xtr}}$, even for sources with as few as 10 counts. All of these results are not substantially affected by use of the likelihood ratio (C) statistic instead of the χ^2 statistic.

We conclude from this simulation analysis that all broad-band luminosities derived here are reliable, but that the individual spectral parameters (kT and $\log N_H$) are unreliable for the faintest sources. As noted above, we include these parameters in Table 3 even for faint sources so that others may reproduce our luminosity results. To further emphasize that the spectral parameters of faint sources should not be considered accurate, a warning is given in the table notes via a faint source flag. We thus confine discussion of spectral properties to the 790 sources (74% of 1075) with $C_{xtr} \geq 30$ cts, for which estimated errors are much smaller than the parameter ranges. Finally, we note that even well-determined spectral parameters may not have a clear astrophysical meaning, as they often are the sums of photons from different stages of flare evolution and/or different physical structures in the active young stellar system.

Figure 7 shows three spectra that exemplify some of the characteristics of ACIS ONC spectra. The top panel shows a fairly typical spectrum: 91 counts are extracted and successfully modeled with a plasma at $kT = 1.1$ keV with moderate absorption of $\log N_H = 20.8$ cm^{-2} . The counterpart is a very young ($t \leq 0.1$ Myr) low mass ($0.2 M_\odot$) star with little visual absorption, a 3.2 day rotational period, and a possible X-ray flare. The middle panel shows a deeply embedded faint source: 17 counts are extracted and are modeled with a $kT = 2.8$ keV plasma with high absorption of $\log N_H = 22.8$ cm^{-2} . The spectral fit (not shown) passes directly through the data values as there are no degrees of freedom (3 fit parameters and 3 bins). These spectral parameters are not individually reliable and are only used to infer the luminosity of the source. The counterpart here is IRc 3 = Source i, an important luminous and massive member of the BN/KL embedded cluster responsible for at least some of the molecular outflows in the region. The bottom panel shows a bright source with high signal-to-noise across the spectrum: 3469 counts are extracted and modeled with only partial success using a $kT = 2.1$ keV plasma and moderate absorption of $\log N_H = 21.5$ cm^{-2} . The spectrum shows strong excess emission around 0.8 – 1.0 keV (attributable perhaps to Fe-L, Ne IX and Ne X lines) and perhaps also around 3 – 4 keV. The counterpart here is a $2 M_\odot$ star with age around 1 Myr, rotational period of 9.2 days, $A_V = 3.2$ mag absorption, and an infrared excess $\Delta(I - K) = 0.7$ mag indicating a circumstellar disk.

The reliability of one aspect of the spectral analysis is subject to independent test.

Figure 8 compares the column absorption $\log N_H$ (in cm^{-2}) obtained here with the visual absorption A_V (in mag) obtained by Hillenbrand (1997) from optical spectroscopy and photometry. The dashed curve shows the conversion relationship $N_H = 2 \times 10^{21} A_V$ for interstellar material with a standard gas-to-dust ratio (Savage & Mathis 1979). It suggests that visual absorption may be systematically slightly higher than expected from the X-ray absorption for a standard gas-to-dust ratio. The scatter is consistent with expected errors in most cases, but some $\log N_H$ values are completely incorrect with values around $\log N_H \simeq 22$ when $A_V \simeq 0$ or $\log N_H < 20$ when $A_V \geq 2$. Gross errors of this type may arise from our use of simplistic one-temperature plasma models, or incorrect A_V values due to optical veiling or spectral typing errors. We conclude that the $\log N_H$ values derived here should only be used as a rough guide to the true absorption to each source.

2.9. Broad-band luminosities

Despite the difficulties of producing spectral fits of a quality necessary for detailed study of plasma properties, the fits provide reliable broad-band luminosities. Effectively, the spectral model is treated here as a spline fit to the data, and we integrate under the fitted curve to obtain the broad-band fluxes in the soft 0.5 – 2 keV and hard 2 – 8 keV bands. The fluxes are converted to luminosities assuming a distance of 450 pc to the ONC, although we recognize that this distance is not precisely established and could be as high as 480 pc.

For sources with ≥ 30 counts, we provide four log luminosity values: soft band $\log L_s$ covering 0.5 – 2 keV, hard band $\log L_h$ covering 2 – 8 keV, total band $\log L_t$ covering 0.5 – 8 keV, and the total band after correction of absorption $\log L_c$. These values have complementary uses: L_s allows comparison with earlier measurements from the *Einstein* and *ROSAT* satellites, but is most vulnerable to differences in absorption between sources; L_h is nearly unaffected by absorption but measures only very hot flare-generated plasma; L_t most closely represents all of the emission directly observed by *Chandra*, but underestimates the true luminosity due to soft-energy absorption; and L_c attempts to correct for the absorption. Note that the wide dispersion and not-infrequent errors in $\log N_H$ values (Figure 8) suggests that L_c values should be used with considerable caution. For faint ($C_{xtr} < 30$ counts) sources, only L_t is reported.

All luminosity values have been corrected for the contribution of background emission and the counts in the wings of the PSF by scaling the luminosity derived from the spectral fit by the factor $(C_{xtr} - B_{xtr}) / (C_{xtr} f_{PSF})$ (see §2.6). These corrections are small, < 0.1 in $\log L$, for most sources. The formal uncertainties to the luminosities are also estimated to be small for most sources, roughly ± 0.1 in $\log L$, though higher for the weakest sources with

poor statistics and those with inaccurate spectral fits (see footnotes to Table 3). However, the *astrophysical* accuracy of the luminosities, in the sense of the reproducibility of the measurements in independent observations, is much worse due to intrinsic variability. About half of the sources showed significant variability during our two ~ 12 -hour observations, with many of these changing in brightness by more than a factor of two or > 0.3 in $\log L$. It is therefore reasonable to expect scatter of several tenths in scatter plots involving $\log L$ values due in part to uncertainties in the analysis but mostly to source variability.

The reader can calculate an approximate hardness ratio for each source using $(\log L_h - \log L_s)$ or $(\log L_h - \log L_t)$. However, we caution that the hardness ratio is difficult to interpret here as the effects of different absorptions and different intrinsic spectral hardnesses are intermingled. A bias in this hardness ratio will be present in sources far off-axis as we do not correct for the energy dependence of the telescope vignetting. An absorption-corrected soft X-ray luminosity can also be calculated from $L_c - L_h$, as the correction rarely has significant effect above 2 keV. But we caution again that the corrected soft-band luminosity is particularly sensitive to errors in $\log N_H$ (Figure 8).

2.10. Very bright sources and photon pileup

$\theta^1\text{C Ori}$ (source #542), the massive O6 star dominating the Trapezium at virtually all wavelengths, suffers very significant pileup in the CCD detector. That is, several photons arrived in the same pixel during a 3.2 s frame resulting in an incorrect evaluation of the photon energy and exclusion by the on-board event processor. Most of the real events from $\theta^1\text{C Ori}$ were lost in this way; we estimate that $\simeq 450,000$ source photons were incident on the detector. We recover from this problem in an approximate fashion by extracting $\simeq 9,000$ events from a $2'' - 4''$ annulus around the source which contains 1%–3% of the PSF encircled energy (the exact fraction varies with photon energy), creating a special arf file appropriate for this annulus using the IDL program *xpsf.pro* (G. Chartas, private communication), and calculating a corrected spectral fit. Several other sources, notably the massive stars $\theta^1\text{A Ori}$ (#498) and $\theta^2\text{A Ori}$ (#828) and the late-type stars JW 567 (= MT Ori, #626) and P 1771 (#243) suffer mild photon pileup and the resulting luminosities are likely underestimated by 10–30%. The spectral fits and variability measurements may also be affected in complex ways. Bright off-axis sources like KM Ori (#77) are less affected because the photons are distributed over many pixels by the broadened PSF. Pileup warnings are provided in Table 3 notes whenever $CR_1 > 100$ or $CR_2 > 100$ cts ks^{-1} .

2.11. Completeness and reliability of the catalog

To assess the level of contamination of the ACIS ONC catalog from spurious sources, we examined the faintest 50 sources with $(C_{xtr} - B_{xtr})/f_{psf} \leq 10$ in some detail:

Spatial distribution Three spatial components are seen: half are clustered around the Trapezium region, a group of ~ 13 are in the BN/KL region, and ~ 15 are distributed randomly in the field. Naturally they avoid a strong concentration in the inner $1-2'$ as the background from $\theta^1\text{C Ori}$ precludes finding very faint sources there. The observed pattern makes sense if the sources are nearly all real: some ONC members, some embedded members, and some extragalactic sources. In particular, it suggests that an ultra-deep observation will see many more sources in the embedded BN/KL cluster.

Counterparts One-third (16/50) do not have stellar counterparts, compared to 8% in the full sample. This does not necessarily mean that all faint sources lacking counterparts are spurious; due to the L_x-L_{bol} correlation, the fainter sources are less likely to appear in flux limited optical and infrared catalogs.

Counterpart offset Of the 34 sources with listed stellar counterparts, in all but 8 the counterpart offset lies within the dense concentration in Figure 4. This, we believe, is strong evidence that these sources are real Orion stars. The eight outliers ($\# 137, 198, 303, 545, 827, 930, 943, \text{ and } 1073$) with offsets ranging from $0.9''$ to $3.1''$ are the strongest candidates for spurious sources in the catalog. If drawn randomly from the full sample, only 2 – 3 sources should be present with these large offsets.

This last test is the clearest indication that several spurious sources are likely present in the catalog. When a few additional spurious sources without stellar counterparts or with slightly higher count rates are considered, we estimate that $\simeq 10$ of the faintest sources, or 1% of the entire source catalog, are likely spurious.

2.12. Detection limit of the catalog

Given the complexities of the *wavdetect* algorithm applied to the spatially varying PSF (§2.4), the subjective nature of our corrections to the source list (§2.4), the position-dependent extraction radii and background levels (§2.6), and the wide range of source spectra (§2.8), it is not simple to establish an astronomically useful detection limit. One procedure might be to set an extraction circle onto the image at the location of a specific source, determine the Poissonian 99th-percentile upper limit in counts, divide by the effective exposure time at that location in the image, and convert to a luminosity limit using a spectral model.

But, as there are hundreds of faint or embedded ONC members which are undetected in our image, we provide here a more general method that can be applied to any location of interest.

First we determine the count limit of the *wavdetect* source detection algorithm (§2.4). Figure 5 shows the distribution of extracted source counts as a function of off-axis angle θ . From careful examination of the image, we are very confident that all sources brighter than the plotted curve,

$$C_{lim}(\theta) = 9 + 0.16\theta + 0.28\theta^2 \quad (5)$$

in the full band are detected. Note that the sources found below this curve are still reliable; we just can not be sure that all such sources have been found.

For sources of marginal significance, one empirically achieves a better signal-to-noise ratio by evaluating the source counts (or limits thereof) using an extraction radius with 50% of the encircled energy rather than the usual 95% extraction radius; this is most likely due to background variations. The limiting background-corrected source count rate is then

$$CR_{lim}(\theta) = [C_{lim}(\theta)(0.95/0.50) - \pi R_{xtr,50\%}(\theta)^2 B(\theta)] / (f_{PSF} f_{vig} E_{eff}) \quad (6)$$

where $R_{xtr,50\%}$ is the 50% extraction radius given in footnote 7, $B(\theta)$ is given by the background fits in §2.6, $f_{PSF} = 0.50$, $f_{vig} \simeq 1.00 - 0.014\theta$ is an approximate correction for telescope vignetting at 1.5 keV, and E_{eff} is the exposure time in ks given in Table 1.

While the limiting count rate calculated in this fashion is accurate to about $\pm 30\%$, there is considerably more uncertainty in converting this to a limiting astrophysical luminosity given the wide range in spectral shapes and foreground absorptions. If we assume a plasma energy of $kT = 3$ keV, then the conversions between CR_{lim} (in counts ks^{-1}) and $\log L_{t,lim}$ (in erg s^{-1} in the full 0.5 – 8 keV band) can be approximately expressed as

$$\log L_{t,lim} \simeq 28.9 + \log CR_{lim} + 0.3(\log N_H - 20.0) \text{ erg s}^{-1}. \quad (7)$$

For stars with absorptions measured from optical or infrared measurements, N_H can be estimated from the relationship $N_H = 2 \times 10^{21} A_V \text{ cm}^{-2}$ (see Figure 8). We caution that this $L_{t,lim}$ value for a given star could be seriously in error if the intrinsic spectrum differs from the assumed 3 keV plasma or if the absorption estimate is inaccurate.

The result of these computations is that undetected stars with negligible interstellar absorption have upper limits of $\log L_t < 28.0 \text{ erg s}^{-1}$ in the inner region of the detector (except close to $\theta^1\text{C Ori}$) and $\log L_t < 28.6 \text{ erg s}^{-1}$ near the edge of the field. At a given θ , the limiting observed luminosity rises by $\log L_t \simeq 0.5$ if $A_V \simeq 1 - 2$ compared to $A_V = 0$.

Statistical study of ONC subpopulations, such as the measure of X-ray luminosity functions, requires consideration of both X-ray nondetections of catalogued stars (in statistical

parlance, censored bias) and on incompleteness of the catalogued sample (truncation bias). The techniques of survival analysis provide strategies for treating censoring, but it is more difficult to overcome truncation biases (Feigelson 1990, 1992). The sample of 1576 stars with $V < 20$ by Hillenbrand (1997), for example, should be virtually complete for ONC members with masses $M > 0.1 M_{\odot}$ and absorptions $A_V < 2.5$ mag. The ACIS observation detects X-rays from nearly this entire sample: only 8 stars from Hillenbrand (1997) with $M > 0.7 M_{\odot}$ and high membership probabilities inferred from proper motion measurements are absent from the X-ray source tables (JW 62, 108, 407, 479, 531, 593, 608, and Parenago 1772). Ninety-two additional stars with smaller masses are absent. Statistical analysis of ACIS results based on the $V < 20$ sample should therefore be reliable if one avoids stars with low stellar masses and high absorption. Statistical analysis of other samples, such as brown dwarfs and deeply embedded protostars, may be subject to considerable bias.

3. Source list and properties

The database of sources found in the merged Orion fields is provided in Tables 2 and 3 which appear in their entirety in the electronic edition. The first of these large tables gives source positions, stellar identifications, and multiwavelength stellar properties while the second table gives source count rates, luminosity, spectral and variability information. Some stellar properties like mass and age are given to higher precision than we believe is scientifically warranted. This is done to reduce the number of overlapping points in scatter plots. Specifics regarding table entries follow.

Table 2, column 1 Source name in the form CXOONC Jhhmmss.s-ddmmss (*Chandra X-ray Observatory* Orion Nebula Cluster). These names supercede those given by Garmire et al. (2000), which often differ in the last digit.

Columns 2-3 Source position in decimal degrees in epoch J2000. The field is aligned to the 2MASS/ACT/Tycho reference frame to within $\pm 0.1''$ (§2.5), and individual source positional accuracies vary between about $0.1'' - 3''$ depending on the signal strength and off-axis distance. See table notes ('x' in column 17) for cases of crowding, location on bright source readout trail, or other issue regarding the X-ray image.

Column 4 Distance from the cluster center in arcminutes, measured from θ^1 C Ori. This quantity is useful for evaluating point spread function and completeness effects (§2.6 and §2.4).

Column 5 Detection in previous X-ray studies of the Orion Nebula: a = *Einstein Observatory* (Ku & Chanan 1979; Ku, Righini-Cohen, & Simon 1982; Gagné & Caillault 1994);

b = *ROSAT* Position Sensitive Proportional Counter (Geier et al. 1995; Lohmann & Wendker 2000); c = *ROSAT* High Resolution Imager (Gagné et al. 1995); d = *ASCA* satellite (Yamauchi et al. 1996); e = *Chandra X-ray Observatory* ACIS-I (Garmire et al. 2000); and f = *Chandra X-ray Observatory* ACIS-S3 (Schulz et al. 2001). The associations between the older lower-resolution sources and CXOONC sources are sometimes uncertain due to confusion.

Column 6 Stellar identification of the X-ray source (§2.5): P = Parenago (1954); JW = Jones & Walker (1988); PSH = Prosser et al. (1994); H = Hillenbrand (1997); HC = Hillenbrand & Carpenter (2000); CHS = Carpenter et al. (2001). JW designations are preferentially listed when available. See table notes (‘id’ in column 17) for cases of multiple counterparts and for Greek letter labels (e.g., θ^1 G Ori).

Column 7 Offset ϕ between the X-ray and stellar source in arcseconds. Star positions from Hillenbrand & Carpenter (2000) are preferentially adopted when multiple values are available. Potential uncertainties in source identification due to large offsets are noted (‘id’ in column 17).

Column 8-10 Effective surface temperature $\log T_{eff}$, bolometric luminosity $\log L_{bol}$, and visual absorption A_V from Hillenbrand (1997) and subsequent additions and updates to the database. These stellar properties, derived from spectroscopy of $V < 20$ stars and V band photometry, locate the star on the HR diagram.

Column 11-12 Logarithm of the stellar mass (in M_\odot) and age (in years) obtained from the HR diagram location and the PMS evolutionary tracks of D’Antona & Mazzitelli (1997). These values are updated from those given by Hillenbrand (1997) using older tracks. Note that considerable debate exists over the accuracy of PMS evolutionary tracks and systematic errors may be present. In particular, it is difficult to distinguish stellar ages $\log t < 5.5$ due to uncertainties in initial conditions (Stahler 1983).

Column 13 K band ($2.2 \mu\text{m}$) excess, $\Delta(I - K)$, over the value expected for a photosphere with temperature $\log T_{eff}$, based on the infrared photometry of Hillenbrand et al. (1998) and Hillenbrand & Carpenter (2000). Values of $\Delta(I - K) > 0.3$ are widely considered to indicate warm dust in a circumstellar disk.

Column 14 Additional stellar properties: FIR = possible counterpart mid- and far-infrared source (see footnote for details); HH = Herbig-Haro objects or their host star from Hubble Space Telescope (HST) images (Bally et al. 1998; Bally, O’Dell, & McCaughrean 2000; Bally & Reipurth 2001); L = L band ($3.5 \mu\text{m}$) excess interpreted as protostellar candidate (Lada et al. 2000); N = N band ($10 \mu\text{m}$) excess interpreted as truncated disk

(Stassun et al. 2001); pd = proplyd and/or disk imaged by the HST in emission and/or silhouette (O’Dell & Wen 1994; O’Dell & Wong 1996; Bally, O’Dell, & McCaughrean 2000; Bally & Reipurth 2001); r = radio continuum source detected at centimeter (Felli et al. 1993) or millimeter (Mundy et al. 1995) wavelengths; and wc = star with wind collision front (Bally, O’Dell, & McCaughrean 2000). Identifications are based on positional coincidences consistent with the X-ray positional accuracies shown in Figure 4, and may not always represent physical associations.

Column 15 Rotational period obtained from photometric modulations of starspots. Uncertain or multiple periods are discussed in the table notes (‘p’ in column 17).

Column 16 Source of the rotational period: C = Carpenter et al. (2001); H = Herbst et al. (2000) and Herbst, Bailer-Jones, & Mundt (2001); S = Stassun et al. (1999).

Column 17 Footnote indicator: x = X-ray image issue; id = stellar identification issue; and p = rotational period issue.

Table 3, column 1 Source number from Table 2.

Columns 2-5 Quantities associated with event extraction from the full band (0.5 – 8 keV) image described in §2.6: total extracted counts C_{xtr} and estimated background counts B_{xtr} in a circle of radius R_{xtr} centered on the source position given in Table 2, and the fraction of the point spread function f_{PSF} encircled by R_{xtr} at the source location in the ACIS field.

Columns 6-7 Average source count rates CR_1 during the October 1999 and CR_2 during the April 2000 observations. CR is defined in §2.6. Location-dependent exposure variations are not included in these values.

Column 8 Variability class defined in §2.7: Const (constant); LT Var (long-term variability); Pos flare (possible flare); and Flare.

Columns 9-10 Spectral parameters from one-temperature plasma models, when the fit to the source spectrum is satisfactory (§2.8). $\log N_H$ (in cm^{-2}) is the equivalent hydrogen column density of intervening interstellar material producing soft X-ray absorption, and kT (in keV) is the energy of the plasma. See §2.8 regarding the reliability of these values. For faint sources, these quantities are highly uncertain and are used only as rough characterizations of spectral shape.

Column 11 Lower and upper plasma energies (in keV) for sources fit with two-temperature plasma models. Again, these values are only suggestive for faint sources.

Column 12 Flag indicating the presence of spectral features indicative perhaps of specific elemental abundances enhanced over the assumed 0.3 times solar levels.

Columns 13-16 X-ray luminosities of the source assuming a distance of 450 pc averaged over both observations: L_s = soft-band (0.5 – 2 keV) luminosity; L_h = hard-band (2 – 8 keV) luminosity; L_t = total band (0.5 – 8 keV) luminosity; and L_c = total band luminosity corrected for the estimated interstellar absorption. These values are corrected for all telescope and detector efficiencies convolved with the spectral model indicated in columns 9 – 11. For faint sources, only L_t is given.

Column 17 Footnote indicator: f = faint source warning (spectral parameters are only used as a spline fit for obtaining L_t); p = photon pileup warning; s = spectral issue; v = variability issue. The table notes give details for spectral and variability issues, in particularly describing temporal variations when the Variability Class is ‘Flare’.

4. Demographics of the X-ray population

4.1. Sources without stellar counterparts

Before examining the broad X-ray properties of the ONC and its molecular cloud environs, we seek to establish the level of contamination by extraneous sources. Table 4 presents the 101 CXOONC sources that have no detection in the available optical and near-infrared catalogs (§2.5). Most of these unidentified sources are heavily absorbed with $\log N_H \geq 22.0$ cm^{-2} and thus lie behind or deeply embedded within the Orion molecular cloud.

Some of these must be members of an extragalactic (mainly active galactic nuclei) or background Galactic source population seen through the cloud (Garmire et al. 2000). However, Figure 9 shows that most are too clustered towards the field center for an isotropic extragalactic population. This is further confirmed by comparison of the source fluxes with the extragalactic $\log N - \log S$ distribution. From CO surveys, we estimate that the depth through the cloud ranges from $\log N_H \simeq 22$ cm^{-2} near the edges of the ACIS field to $\log N_H \simeq 23$ cm^{-2} near the center. Thus emission from extragalactic sources will be absorbed below 2 – 4 keV at different locations in the field. From the 2 – 10 keV extragalactic $\log N - \log S$ curve derived with ACIS-I from the northern Hubble Deep Field, we estimate that extragalactic sources can not account for more than 25 heavily absorbed sources present in the ONC image, and nearly all of these will have $C_{xtr} < 25$ counts. As most of the faint sources in Table 4 have 25 – 100 counts (plus 14 that lie in the range $100 < C_{xtr} < 3700$) and are concentrated towards the field center, we estimate that there are only 10 – 15 extragalactic sources in the entire field. The contribution of background Galactic sources

can not be confidently estimated as their $\log N - \log S$ distribution has not been reported at these faint flux levels for this Galactic latitude. Altogether, the contamination from extragalactic or background Galactic X-ray sources probably accounts for $\simeq 20$ sources or $\simeq 2\%$ of the full ONC source sample.

The $\simeq 80\%$ of the ACIS sources without catalogued stellar counterparts which are not contaminants must be new young stars associated with the Orion cloud. In column 8 of Table 4, we suggest a tentative classification for these sources based on location and absorption. Twenty-six sources are lightly absorbed with $\log N_H < 22.0 \text{ cm}^{-2}$; most of these are probably new low-mass members of the ONC. Several are concentrated within $\sim 0.5'$ around $\theta^1\text{C Ori}$, while others are distributed across the ACIS field.

The remaining 75 sources are deeply embedded or behind the cloud with $\log N_H > 22.0 \text{ cm}^{-2}$, some of which are probably protostars very recently formed in dense molecular cores. Ten lie on the OMC 1 (= Orion KL) molecular core (Figure 9) and are likely new members of the BN/KL young stellar cluster. These are among the first clearly identified low mass members of this cluster, as it is too obscured for complete JHK band study and mid-infrared observations to date have been sensitive only to the $L \geq 1000 L_\odot$ high-mass stars (Gezari et al. 1998). Five of the sources coincide with the OMC 1S (= Orion S) molecular core. Little is known about the young stellar population of OMC 1S other than a luminous protostar FIR 4 and an unknown protostar producing an unusually fast and young bipolar flow (Rodríguez-Franco Martín-Pintado & Wilson 1999). Nine embedded sources lie along the dense molecular filament running north from OMC 1 towards OMC 2/3. A small concentration of infrared-excess and photometrically variable young stars has also been found in this region from observations with the 2MASS telescope (Carpenter et al. 2001). This molecular concentration is thus likely a separate star forming region, and we classify these ACIS sources ‘OMC 1N’ (analogous to the OMC 1S designation) in Table 4. No unidentified embedded X-ray sources are associated with the Orion Bar (the NE-SW molecular structure south of the OMC 1 and OMC 1S concentrations in Figure 9), suggesting that it is not an active region of star formation.

Finally, we classify the 51 heavily absorbed ACIS sources which do not coincide with dense molecular cloud cores as ‘Embd/Bk’. Roughly 20 of these are contaminants (see above) and the others are likely new PMS stars, perhaps embedded low-mass ONC members or somewhat older members of the star forming cores.

While the luminosity distribution for the unidentified ACIS sources is similar to that of the identified sources, their spectral properties differ: nearly 60% have plasma components with fitted energies $>10 \text{ keV}$ compared to only 10% for identified sources. This suggests that at least 300 additional embedded X-ray emitting stars with lower plasma temperatures exist

in the field but are undetected due to the high column densities. Most of these will likely have counterparts among the hundreds of heavily absorbed low-mass and VLM ONC stars (Hillenbrand & Carpenter 2000). Many of these would likely be detected with longer ACIS exposures to increase sensitivity and repeated observations to catch flares.

One unidentified source, #881 or CXOONC 053524.6-052759, deserves special note due to its extraordinarily high and constant flux. It has $\simeq 3700$ total counts, $\log N_H = 22.2$ cm^{-2} , $kT > 10$ keV, and $\log L_t = 31.3$ erg s^{-1} (assuming $d = 450$ pc), placing it among the brightest 2% of sources in the field. The spectrum is also well-fit by a powerlaw model with photon index $\Gamma = 1.5$ over the range 1 – 8 keV, but an additional soft component may be present from 0.5 – 1 keV. There is no evidence for spatial extent larger than $\simeq 2''$; this limit is high because the source lies $5'$ off-axis. No flux variations above $\simeq 10\%$ are present within an observation, and $< 7\%$ (3σ) flux difference is seen between the two observations. The source was detected with the *ROSAT* HRI instrument at a level consistent with the $\log L_s = 30.1$ erg s^{-1} found with ACIS in the soft band (Gagné et al. 1995).

The properties of this source do not readily fit most categories of X-ray sources. It is: too constant and with a $\log L_t/L_{bol}$ ratio too high for a typical ONC PMS star or protostar; too bright and hard compared to typical extragalactic background sources; too constant for a typical Galactic accretion X-ray binary system; too bright and too hard for blackbody emission from an isolated young neutron star; and too hard for Bondi-Hoyle accretion of molecular gas onto an isolated neutron star. Perhaps the most likely possibility is the hard powerlaw component of a transient, low magnetic field, neutron star binary system seen during quiescence. Several examples of such systems are known in the Galaxy including Cen X-4 and Aql X-1 (Rutledge et al. 2001, and references therein). The soft spectral component seen in CXOONC 053524.6-052759, with $L_x \simeq \text{several} \times 10^{32}$ erg s^{-1} (0.1 – 1 keV assuming a blackbody or thermal temperature around 0.1 keV) after correcting for absorption, would then arise from the neutron star surface or atmosphere. We note that, if the transient neutron star binary model is correct, then the system has not emerged out of quiescence above $L_x \sim 10^{34}(d/\text{kpc})^2$ erg s^{-1} during the past ~ 30 years.

4.2. Global X-ray properties

Having established that 98% of the CXOONC sources are young stars from the ONC or nearby Orion star forming cores (91% by precise spatial coincidence with catalogued stars and 7% by inference in §4.1), we can treat the entire ACIS source population as a unified sample of young Orion stars with considerable reliability. We consider here only univariate distributions of X-ray properties such as flux, luminosity, variability and spectra. Bivariate

distributions comparing the X-ray properties with other stellar properties are considered in Feigelson et al. (2002b).

The distribution of source fluxes (Figure 10, left panel), where $F_t = L_t/4\pi(450 \text{ pc})^2$, is better described as a lognormal rather than a power law as commonly seen in extragalactic source populations. The mean and standard deviation are $\langle \log F_t \rangle = -12.9 \pm 0.7 \text{ erg s}^{-1} \text{ cm}^{-2}$. The hatched region denotes the completeness limit, which ranges from $\log F_t = -14.4$ to $-14.9 \text{ erg s}^{-1} \text{ cm}^{-2}$ depending on location in the field (§2.12). We emphasize that the fall in source counts in the $-15.5 < \log F_t < -14.5 \text{ erg s}^{-1} \text{ cm}^{-2}$ interval (and the corresponding fall in luminosity counts in the $28.0 < \log L_t < 29.0 \text{ erg s}^{-1}$ interval) is intrinsic to the source population and is not caused by sensitivity limitations.

The luminosity distribution (middle panel) of course has a similar shape, with $\langle \log L_t \rangle = 29.4 \pm 0.7 \text{ erg s}^{-1}$. A link to another stellar property is easily found: the most luminous sources are also the high- and intermediate-mass stars (hatched region, see §5.1-5.2). Further analysis shows that stellar mass accounts for more of the variance in X-ray luminosity than any other stellar property (Feigelson et al. 2002b). The total luminosity of all 1075 sources is $L_t = 3.2 \times 10^{33} \text{ erg s}^{-1}$ in the total (0.5 – 8 keV) band and $L_h = 1.3 \times 10^{33} \text{ erg s}^{-1}$ in the hard (2 – 8 keV) band. The latter value compares very well to the integrated luminosity of $1.3 \times 10^{33} \text{ erg s}^{-1}$ (adjusted for a distance of 450 pc) in the 2 – 10 keV band found with the non-imaging *Ginga* satellite in a 0.2° region around the Trapezium stars (Yamauchi & Koyama 1993). The dominant star of the Trapezium, $\theta^1\text{C Ori}$, contributes $L_t = 2 \times 10^{33} \text{ erg s}^{-1}$ or $\simeq 60\%$ of the total band luminosity and $L_h = 5 \times 10^{32} \text{ erg s}^{-1}$ or $\simeq 40\%$ of the hard band luminosity.

Figure 10 (middle panel) indicates that the presence or absence of an infrared excess, an indicator of a circumstellar disk, has no discernable effect on the distribution of X-ray luminosities. Similarly, no effect is seen in $\log L_t/L_{bol}$. There is thus no evidence that a circumstellar disk, at least one sufficiently massive and dusty to produce excess K-band emission, is required for the elevated X-ray emission of PMS stars. A similar result was found in several *Einstein* and *ROSAT* studies of nearby T Tauri stellar populations (Feigelson & Montmerle 1999), although Stelzer & Neuhäuser (2001) find that weak-lined T Tauri stars are several-fold more X-ray luminous than classical T Tauri stars in the Taurus-Auriga complex.

The distribution of the ratio of X-ray to stellar bolometric luminosity has a mean and standard deviation of $\log L_t/L_{bol} = -3.9 \pm 0.7$ (Figure 10, right panel). The non-Gaussian tail around $-9 < \log L_t/L_{bol} < -6$ is due to mid-A to late-O type stars which have high L_{bol} but modest L_t values (see Figure 12, left panel). Several dozen low mass stars have high values above the ‘saturation’ level $\log L_t/L_{bol} \simeq -3.0$ that defines the maximum X-ray

emission seen in magnetically active main sequence stars (e.g. Vilhu & Walter 1987; Fleming, Schmitt, & Giampapa 1995; Randich 1997). Some of these were observed during a flare, but others exhibit high but relatively constant emission.

The variability class distribution is shown in Figure 11 (left panel). The excess of sources with ‘Constant’ emission compared to the other classes is a selection effect: the ‘Constant’ sources are dominated by sources with $C_{xtr} < 50$ counts which are too weak to clearly show flaring activity (hatched region). If these weak sources are ignored, the distribution among the four variability classes becomes roughly equal. If we group ‘Flare’ and ‘Possible flare’ sources together into a single category, then 55% of the stronger sources in the field exhibit some form of intra-day variability. It is difficult to convert this number into a flare duty cycle because of the great range of flare durations seen in the source lightcurves.

Figure 11 (middle panel) show the distribution of plasma energies for sources with ≥ 30 extracted counts and satisfactory one-temperature fits. (Recall that there may be systematic errors in kT values; §2.8). The median plasma energy $kT = 2.6$ keV, and the distribution is asymmetrical with a heavy tail to higher energies. There is no apparent trend that flaring sources exhibit harder spectra.

Two results emerge from these source temperatures. First, nearly all PMS stars have plasmas hotter than seen in the Sun, even during its most powerful contemporary flares. Integrated over its disk and viewed with CCD spectral resolution, the Sun typically would be seen at a plasma energy ≤ 0.2 keV, rising to 0.6 keV during powerful flares (Peres et al. 2000; Reale, Peres & Orlando 2001). Note, however, that a soft solar-type spectral component would often be undetectable in Orion stars due to interstellar absorption.

Second, while $kT \simeq 10$ keV energies were found during an extremely powerful T Tauri flare with the *ASCA* satellite (Tsuboi et al. 1998), we find that such high temperatures are commonly present even at moderate X- ray luminosities and in stars not exhibiting flaring lightcurves. The plasma temperatures of sources with intraday variability (‘Flare’ and ‘Possible flare’ variability classes) are nearly indistinguishable from those of non-flaring sources. This implies that the X-ray emission from pre-main sequence stars, even those without apparent variations during an observation, is predominantly flare emission with negligible contribution by a softer ‘coronal’ component. This supports current ideas that the ‘quiescent’ emission in magnetically active stars arises from microflares rather than coronal processes (Drake et al. 2000, and references therein). The high ONC temperatures also indicate that stellar flares during their formative years are considerably hotter than in the later main sequence phase. This extends a similar earlier finding among main sequence stars (Güdel, Guinan, & Skinner 1997).

The interstellar column densities derived from X-ray spectral fitting (Figure 11, right panel) are not an intrinsic property of PMS X-ray emission, but rather reflect the location of each star in relation to the blister HII region and the bulk of molecular cloud material behind the HII region. The median $\log N_H = 21.7 \text{ cm}^{-2}$ and most values lie in a lognormal distribution with a FWHM of 1.6 in $\log N_H$, but about one tenth of the sources suffer no detectable absorption with $\log N_H < 20.0 \text{ cm}^{-2}$. Other sources have absorptions equivalent to $A_V \sim 10 - 100$; these are likely to include very young protostars recently emerged from the active star forming molecular cores, many of which are previously unidentified (see §4.1).

5. X-ray emission along the Initial Mass Function

5.1. High-mass stars

It is well-accepted that X-ray emission from stars earlier than B1.5–B2 arises from processes in their radiation-driven stellar winds, in contrast to X-ray emission from lower mass T Tauri stars which arises from magnetic reconnection activity (§1). These models are supported by extensive data from the *Einstein* and *ROSAT* satellites; for example, X-ray emission from O stars have showed very little variability and their emission lines exhibit Doppler broadening. While the sample of OB stars in the ONC is small, it is complete for low-obscuration regions. We also have uniform spectral and variability data with higher signal-to-noise ratios than available from previous satellite observations.

We consider here and in §5.2 a sample of 53 ONC stars with $M > 1.5 M_\odot$ with $V < 20$ lying in the ACIS field of view (Hillenbrand 1997). These are listed in Table 5, ordered by decreasing mass. Forty-eight are detected with ACIS and appear in Tables 2 and 3, while five are undetected: P 1772, JW 108, P 1892, JW 531 and JW 608⁸. For the undetected sources, full-band X-ray upper limits $L_{t,lim}$ were calculated as described in §2.12⁹ with values in the range $28.4 < \log L_{t,lim} < 29.2 \text{ erg s}^{-1}$. We adopt a soft-band upper limit

$$\log L_{s,lim} = \log L_{t,lim} - 0.3 \quad (8)$$

for the undetected stars based on typical values seen in the detected stars. No significant differences are seen in the scatter plots made using X-ray luminosities from the different

⁸Two other undetected stars, JW 794 and JW 997, are omitted from the sample due to low probability of ONC membership based on proper motions (Jones & Walker 1988).

⁹Parento 1892, which lies in the PSF wings of $\theta^1\text{C Ori}$, was treated manually and assigned an upper limit of 40 source counts.

bands, so we adopt the soft band L_s values to facilitate comparison with *Einstein* and *ROSAT* studies.

Figure 12 (left panel) shows the dependence of L_s/L_{bol} on mass superposed on the loci of stars reported in previous studies. The average of the six ONC stars with spectral types earlier than B2 is $\langle \log(L_s/L_{bol}) \rangle \simeq -7.6$. This is understandably several fold lower than $\langle \log(L_s/L_{bol}) \rangle \simeq -7.1$ found for a large sample of O stars by Berghöfer et al. (1997), shown as a dashed line in the diagram, as their value is based only on stars detected in the shallow *ROSAT* All-Sky Survey and overestimates the true mean of the underlying population. Perhaps more important is the wide scatter of 3 orders of magnitude about this mean for the ONC stars. In the standard theory of X-ray emission from many spatially distributed shocks in the stellar wind, this scatter would be explained by a wide range of shock filling factors (Owocki & Cohen 1999).

However, our variability results cast doubt on the standard model for some massive stars. Figure 13 shows that most of the 8 B2–O6 ONC stars which should be dominated by extended wind emission exhibit variability within a 12-hour observation¹⁰. Indeed, the second-most massive star in the cluster – P 1993 = θ^2 A Ori, O9.5Vpe, $V=5.1$, with $M=31 M_\odot$ and time-averaged $\log L_t = 31.6 \text{ erg s}^{-1}$ – exhibits the most dramatic X-ray variability ever recorded from an O star, with a 50% drop in 10 hours superposed by multiple 10 – 20% flares with 1–3 hour durations. The best previous case for rapid variations was a $\Delta L_s \simeq 30\%$ rise during 2 days in the $V = 1.8$ O9.5Ib supergiant ζ Ori (Berghöfer & Schmitt 1994b). Parenago 2031 (= θ^2 B Ori, B1V, $V=6.0$, $M=12 M_\odot$, $\log L_t = 29.5 \text{ erg s}^{-1}$) shows a very high-amplitude but low luminosity flare similar to many others seen from ONC T Tauri stars. Other less dramatic cases of intra-day variations, also at low luminosity levels, are seen in P 1889, P 2074, P 1863a and P 2085. Except for θ^1 C Ori, all of these stars have X-ray luminosities consistent with those of lower mass cluster members (Figure 12, right panel).

We consider three explanations for the rapid variable behavior seen in these Trapezium B2–O6 stars.

1. Hydrodynamic calculations have shown that strong events as seen in P 1993 can be produced in the occasional large shocks that may propagate through a massive stellar wind (Feldmeier, Puls, & Pauldrach 1997). However, the characteristic temperature of the emitting regions is $\sim 10^6$ K in these models, while the ACIS spectra of the Trapezium sources require 1 – 2 keV plasmas and three (P 1685, P 1993 and P 2074)

¹⁰The fluctuations seen in the lightcurve of P 1891 = θ^1 C Ori may be of instrumental origin, as these counts have been extracted from the wings of a severely piled up ACIS source. P 1993 and P 1889 suffer mild pileup such that the amplitudes, but not general characteristics, of the variations may be affected.

show hot components around 5 – 7 keV. These stars have rather modest winds which may not be capable of producing sufficiently powerful shocks to account for the X-ray flares. For example, the wind of P 1993 has $\log \dot{M} = -7.5 M_{\odot} \text{ yr}^{-1}$ and $v_{\infty} = 700 \text{ km s}^{-1}$ (Howarth & Prinja 1989).

2. The X-ray variation and hard spectrum may be produced by a stellar companion rather than by the massive star that dominates the optical light. For example, spectroscopy and speckle interferometry have established that P 1993 is at least a triple system with a $\sim 10 - 15 M_{\odot}$ close secondary in an eccentric 21 day orbit and a more distant 3 – 7 M_{\odot} companion (Preibisch et al. 1999). Similarly, P 1891 is at least a binary, P 1865 is at least a triple, P 2074 is at least a triple, and P 1863 has at least 5 components. Only P 1889 and P 2031 do not have known companions among the Trapezium B2–O6 stars (Preibisch et al. 1999). The companion model is attractive for most of these systems where the X-ray luminosity is $\log L_t \simeq 29 - 30 \text{ erg s}^{-1}$, similar to hundreds of other lower-mass T Tauri stars in the ONC (Figure 12, right panel). However, this model has difficulty explaining the flare of P 1993 where, with time-averaged $\log L_t = 31.6 \text{ erg s}^{-1}$, it would be in the top $\simeq 0.2\%$ of the lower-mass ONC X-ray luminosity function.
3. The X-ray flares may arise from magnetic reconnection events near the stellar surface of the OB stars themselves. While OB X-ray phenomenology is generally attributed to thermal wind rather than magnetic processes, there is some evidence for solar-type magnetic activity on such stars. This includes: optical spectroscopic and X-ray variability evidence for magnetically confined plasma on the B0.5 IVe star γ Cas (Smith & Robinson 1999); X-ray spectroscopic evidence for very high-density plasma in the O9.7 Ib supergiant ζ Ori (Waldron & Cassinelli 2001); and variable nonthermal radio continuum emission from 25% of OB stars (Bieging, Abbott, & Churchwell 1989). If a sufficiently strong dipole field is present, OB winds may be guided into an equatorial disk structure with shocks heating the gas to X-ray temperatures (Babel & Montmerle 1997). We note that the column density of the wind of P 1993 should be relatively transparent to X-ray emission near the stellar surface, with

$$N_H = \frac{\dot{M}}{4\pi\mu m_p v_{\infty} R_*} \simeq 2 \times 10^{21} \text{ cm}^{-2}, \quad (9)$$

assuming $\log \dot{M} = -7.5 M_{\odot} \text{ yr}^{-1}$, $v_{\infty} = 700 \text{ km s}^{-1}$, $\mu = 1.3$, $R_* = 8 M_{\odot}$, unity filling factor and an isotropic geometry.

We tentatively reach the following conclusions. The three O stars exhibit X-ray properties consistent with the strong and constant emission expected from distributed shocks in line-driven stellar winds. During one of the two observations, however, the O9.5 star P 1993

exhibited a remarkable rapid flaring behavior. From the discussion above, perhaps the most reasonable explanation is that the lower constant level seen in the October 1999 exposure represents the underlying emission from the O star wind, while the April 2000 flare arises from a magnetic process (either reconnection event or shock from magnetically funneled wind material) near the base of the P 1993 wind. The emission from early B stars, despite previous reports that they lie on a $L_x/L_{bol} \simeq 10^{-7}$ locus associated with wind emission, generally exhibits rapid variability and lower X-ray luminosities similar to that commonly seen in ONC T Tauri stars. Their X-ray emission thus likely arises from lower mass companions. The wind emission from B0–B2 stars themselves thus probably has been undetected and lies below $\log L_s < 29 \text{ erg s}^{-1}$ and their $L_x/L_{bol} < -8$ or even < -9 .

5.2. Intermediate-mass stars

The source of X-rays from late B and A type stars, which have neither strong winds nor outer convective zones conducive to a magnetic dynamo, has been the subject of some concern (§1). While some researchers have argued that the emission arises from late-type companions, others call this model into question. The hypothesis is more readily testable in a PMS population like the ONC than in the field main sequence stars that are usually examined, as the T Tauri emission is elevated and more easily studied in very young stars.

Figure 12 (left panel) compares the distribution of L_s/L_{bol} for ONC BA stars with the loci of stars from past studies: the regression line for B stars detected in the *ROSAT* All-Sky Survey (dashed line; Berghöfer et al. 1997), a pointed *ROSAT* survey of mid-B stars (lower open region; Cohen, Cassinelli, & Macfarlane 1997), and several pointed *Einstein* and *ROSAT* surveys of late-B and A stars (upper open region; Caillault & Zoonematkermani 1989; Berghöfer & Schmitt 1994a; Zinnecker & Preibisch 1994; Simon, Drake, & Kim 1995).

While the L_s/L_{bol} diagram appears to show a huge rise in X-ray emissivity as one considers stars of decreasing mass, this effect is entirely due to changes in the bolometric luminosity rather than the X-ray luminosity. This is clearly seen in Figure 12 (right panel) which plots L_s against mass. Here we see that the distribution of X-ray luminosities is virually unchanged from spectral types F5 ($M \simeq 1.5 M_\odot$) through B0 ($M \simeq 20 M_\odot$) with a mean $\langle \log L_s \rangle \simeq 30.4 \text{ erg s}^{-1}$, and remains at a similar level for the $0.7 < M < 1.4 M_\odot$ mass range where the emission clearly arises from magnetic flaring (§5.3 and Feigelson et al. 2002a).

Although our findings do not conclusively exclude intrinsic X-ray emission from late-B and A stars, the ONC intermediate mass star properties can be fully attributed to G and

F companions¹¹. Note that the level of X-ray emission we see in the late-B and A stars cannot be explained by lower mass K and M companions. This implies either that each intermediate-mass star is preferentially formed with a star with higher than average mass, or is accompanied by several companions, one of which is likely to be a G or F star. The presence of F5–A0 ONC stars with somewhat stronger X-ray emission ($\log L_s/L_{bol} \simeq -4$) than reported in *ROSAT* studies is likely due to the higher X-ray emission in ONC PMS compared to the main sequence companion stars that dominate the earlier samples. We cannot address here whether Herbig Ae/Be stars produce extra X-rays than ordinary young A/B stars, as there is no well-established subsample of Herbig Ae/Be stars in the ONC.

5.3. Low mass stars

Figure 14 shows the distribution of soft X-ray flux as a function of mass for $M < 1.5 M_\odot$ stars in the $V < 20$ sample of Hillenbrand (1997)¹². Whereas for higher mass stars L_s/L_{bol} varies with mass and L_s was invariant, the opposite pattern is seen here. Over the mass range $0.1 < M < 1 M_\odot$, the fraction of bolometric energy emerging in the X-ray band is invariant with mean and standard deviation $\langle L_s/L_{bol} \rangle = -4.2 \pm 0.6$, while the X-ray luminosity rises steeply with mass. The behavior of these relations for higher mass stars was explained by the inappropriate use of the easily measured L_{bol} value of the massive companion rather than the unavailable L_{bol} value of a lower mass companion (§5.1). For low mass stars, it is likely that the star that dominates the optical luminosity L_{bol} also dominates the X-ray luminosity L_s , so that the constancy of L_s/L_{bol} for a wide range of low mass stars should be astrophysically meaningful. A steep L_x –mass relation was seen in *ROSAT* study of the Chamaeleon I cloud (Feigelson et al. 1993).

A constant value of L_s/L_{bol} is usually interpreted as a constant X-ray surface flux¹³

¹¹A *Chandra* ACIS study of the central region of the Pleiades cluster finds that sources associated with B6–F4 stars have high fluxes, non-variable light curves, and soft hardness ratios which point to intrinsic emission by the intermediate mass stars not by low mass companions (Krishnamurthi et al. 2001). However, their result is based on only four stars in this mass range and is considered tentative.

¹²Versions of Figures 12 and 14 based on *ROSAT* observations of the ONC and its vicinity are given by Gagné et al. (1995). They show some of the effects discussed here, with a larger sample of high luminosity sources due to a wider field of study, but with a factor $\simeq 100$ lower sensitivity to low luminosity sources than achieved here.

¹³The quantities L_s/L_{bol} and F_s are related to each other according to $F_s = \sigma T_{eff}^4 (L_s/L_{bol})$ where σ is the Stefan-Boltzmann constant and T_{eff} is the effective temperature given in Table 2. $\log F_s$ and $\log L_s/L_{bol}$ do not differ by more than ± 0.3 for ONC stars in the $0.1 < M < 1 M_\odot$ mass range, and correlation plots of

so that X-ray luminosity L_s scales with the surface areas of different stars. Although this accounts for the general behavior of stars in Figure 14, we recognize that the average ONC low mass star has a L_s/L_{bol} value an order of magnitude below the ‘saturation’ value around $L_s/L_{bol} \simeq -3.0$ seen in samples of main sequence G–M stars (e.g. Vilhu & Walter 1987; Fleming, Schmitt, & Giampapa 1995; Randich 1997). This result is not unique to the ONC: sufficiently sensitive *ROSAT* studies of nearby young stellar clusters showed a similar effect. We conclude that low mass T Tauri X-ray emission appears to scale with stellar surface area but, if the mechanism is similar to that in main sequence stars, in most T Tauri stars the magnetic activity may saturate at a level $\simeq 10$ times lower than in main sequence stars. This issue is discussed further in Feigelson et al. (2002b).

The X-ray spectral characteristics of low mass ONC stars also confirm results obtained in earlier work, though with some additional insights. Both the Sun and late-type stars exhibit a scaling between plasma temperature and X-ray emission, roughly $L_s \propto T^{3\pm 1}$, that emerges from simple models of plasma heated in magnetic loops (Rosner, Tucker, & Vaiana 1978). Figure 15 shows such an association as a rise in the lower envelope of the kT distribution with increasing X-ray luminosity, which agrees with the locus found with *ROSAT* for magnetically active late-type stars (Preibisch 1997, heavy dashed line). The effect is also present, though less clearly, in a L_s/L_{bol} vs. L_t diagram. While the majority of sources follow the standard $L_x - T$ correlation, 10% of the ONC sources have fitted plasma energies $kT > 10$ keV and another $\sim 10\%$ have energies considerably higher than expected from the standard $L_x - T$ relation. These temperatures are too high to have been measured with *ROSAT*. Such ultra-hot plasmas have been found in *ASCA* studies during powerful T Tauri and protostar flares (e.g. Koyama et al. 1996; Tsuboi et al. 1998) but have not been previously reported for T Tauri stars with relatively constant lightcurves and ordinary luminosities around $\log L_t \simeq 28 - 30$ erg s $^{-1}$.

We find no clear pattern in the properties of these ultra-hot ONC stars. While a few are attributable to unusually violent flares, most of these stars are deeply embedded with average X-ray luminosities. Many may also have soft components that we can not observe, similar to the ONC stars with two-temperature spectral fits which include a hot component above 5 keV. There is no evidence for the simple solar-type model of a hotter, high-luminosity, high-variability ‘flare’ component superposed on a cooler, low-luminosity, low-variability ‘coronal’ component. We conclude that T Tauri stars of all types can produce ultrahot plasmas, even at modest X-ray luminosities.

low mass ONC stars using the two variables look very similar.

5.4. Very low mass objects (brown dwarfs)

The ONC is perhaps the best laboratory available to study the magnetic activity of PMS brown dwarfs (BDs) as over 100 such objects have been found in recent deep near-infrared imaging of the cluster (Hillenbrand & Carpenter 2000; Luhman et al. 2000; Lucas & Roche 2000). As noted in Paper I, relatively few of these young (proto) BDs appeared in the first ACIS-I image. Here we consider the merged ACIS dataset and discuss in detail the frequency and properties of X-ray detected BDs (see §1).

Table 6 lists, in right ascension order, the 30 ACIS sources associated with very low mass (VLM) ONC objects. By a considerable factor, this is the largest sample of X-ray detected PMS VLM objects yet obtained; previously samples are reported by Neuhäuser et al. (1999), Imanishi, Koyama & Tsuboi (2001) and Preibisch & Zinnecker (2001). An asterisk in column 1 indicates that the source lies in the central $5' \times 5'$ region with deep *JHK* coverage by Hillenbrand & Carpenter (2000). Columns 3 – 6 give *K* and *H – K* apparent magnitudes from Hillenbrand & Carpenter (2000) and Carpenter et al. (2001)¹⁴, photometrically dereddened M_K absolute magnitudes, and corresponding masses from Figure 8 of Hillenbrand & Carpenter (2000), assuming no *K*-band excess from a disk and ages between 0.1-1 Myr. If the age is older, the mass would be larger than the listed value, while if an excess is present the mass would be smaller than the listed value. For comparison, masses estimated from the optical spectroscopy of Hillenbrand (1997) are given in table notes.

We emphasize the difficulty in establishing the masses of young pre-main sequence stars when only near-infrared photometry is available. For example, ACIS sources associated with PSH 116 and H 5096 (found by Garmire et al. 2000) lie considerably above the stellar boundary in the *K vs. H – K* diagram but have spectroscopic temperatures corresponding to $M \simeq 0.05 M_\odot$ PMS BDs. Such misleading infrared magnitudes and colors may be attributed to circumstellar disks. In contrast, an optical or near-infrared spectrum with type $\sim M6$ or later places objects securely on a sub-stellar BD mass track for ages < 1 Myr (Burrows et al. 1997), even accounting for uncertainty in both the empirical measurements (surface temperatures from spectroscopy and bolometric luminosities from reddening-corrected photometry and a bolometric correction) and the theoretical tracks. We acknowledge these uncertainties by adopting the neutral label ‘very low mass objects’ (VLM objects) rather than ‘candidate BDs’ and ‘BDs’. Despite these cautions, the preponderance of evidence indicates that most of the objects listed in Table 6 will never undergo hydrogen ignition and thus are *bona fide*

¹⁴Magnitudes for 2MASS sources not identified as infrared variables were not published in the tables of Carpenter et al. (2001) but can be found at http://astro.caltech.edu/~jmc/papers/variables_orion

PMS BDs.

Columns 7 – 11 of Table 6 reproduce X-ray properties given in Table 3. The bolometric luminosity values used in the final column are estimated from

$$\log L_{bol} \simeq 0.4(M_{\odot,bol} - M_K - BC_K) + \log L_{\odot,bol} \quad \text{erg s}^{-1}, \quad (10)$$

where $BC_K \simeq 2.9$ for a dwarf star with spectral type M7 (Leggett 1992; Leggett et al. 2001). If a disk K -band excess is present, the true value of L_t/L_{bol} is larger than the listed value.

The distinctive X-ray characteristic of the 30 X-ray detected PMS VLM objects in the ONC is their faintness: only 7% (2/30) have total band time-averaged luminosities $\log L_t \geq 29.5$ erg s⁻¹ compared to 37% (136/369) of well-characterized $-1.0 < \log M < -0.5$ M_⊙ ONC stars. However, when considered in terms of X-ray luminosity per unit bolometric luminosity (or, nearly equivalently, X-ray flux per unit surface area), the VLM objects are X-ray luminous: 53% (16/30) have $\log L_t/L_{bol} \geq -3.5$ compared to 34% (124/369) for the low-mass PMS stars. Several of the VLM objects lie above the $\log L_t/L_{bol} \simeq -3.0$ ‘saturation’ level for late-type stars. These strongest emitters are typically caught during a flare, shown in Figure 16. VLM flaring is comparable in frequency and morphology to flares from similarly weak low-mass ONC stars. Most have several hours of elevated emission and are often truncated by the limited duration of the observation. Spectral characteristics are also similar to the general ONC low mass population: the VLM objects are about equally divided between light and heavy absorption; and the plasma temperatures range from <1 to >10 keV.

Comparing the $\log L_t/L_{bol}$ values in Table 6 to the (somewhat uncertain) underlying VLM population, we find that roughly 1/4 of ONC VLM objects have X-ray emission within an order of magnitude of the saturation level. This is comparable to the fraction near saturation for the lowest mass PMS stars which will evolve into late-M main sequence stars. It thus appears that the future turn-on of hydrogen fusion in the core has no effect on the magnetic dynamo or other processes leading to surface activity in PMS objects.

The situation is dramatically different in older (roughly gigayear) L- and T-type field BDs, where surface magnetic activity traced by H α emission nearly always lies 10² or more below saturation levels (Gizis et al. 2000). This decline in magnetic activity might be a consequence of the drop of ionization fraction in the outer layers of $M < 0.08$ M_⊙ objects as they descend their Hayashi tracks and cool. While a magnetic dynamo may still be present in the ionized interiors of older BDs, the eruption and reconnection of surface magnetic structures is impeded by their thick neutral atmospheres (G. Basri, private communication).

6. Summary

The Orion Nebula Cluster is the closest and most spatially concentrated rich young star cluster. It is thus the best available laboratory for studying large samples of stars in a single CCD field, providing impressive subsamples of stars covering all phases of PMS evolution, masses from <0.05 to nearly $50 M_{\odot}$, and ages from 10^5 to 10^7 yr. The value of the present *Chandra* study is greatly amplified by extensive studies of the stellar population in the optical and infrared bands. With 1075 CXOONC sources detecting nearly all low-obscuration $V < 20$ stars, and a considerable number of embedded stars, we present here the largest and most homogeneous sample of PMS stars yet studied in the X-ray band. The ACIS detector provides variability and spectral properties as well as precise positions and broad-band X-ray luminosities.

In addition to an X-ray atlas of the region (Figures 1-3), detailed description of our data analysis (§2, Table 1, Figures 4-8), and a comprehensive database of X-ray sources and properties (Tables 2 and 3, available in full in the electronic edition), we present some of the many results that will emerge from these observations. Other results will appear in forthcoming papers (e.g. Feigelson et al. 2002a,b).

1. We detect 1075 X-ray sources with sub-arcsecond on-axis (arcsecond off-axis) precision in absolute celestial positions (§2.4). The limiting sensitivity is 9 counts on-axis (15–30 counts off-axis) corresponding to a limiting luminosity of $\log L_t = 28.0 \text{ erg s}^{-1}$ on-axis for a lightly absorbed star in the total 0.5 – 8 keV band (§2.9-2.12). Relatively few sources are seen near the detection limit: only 12% have < 20 extracted counts compared to 47% with > 100 counts and 9% with > 1000 counts. The X-ray catalog is estimated to be 99% reliable (§2.11).
2. Ninety-one percent of the ACIS sources are confidently associated with young Orion stars catalogued in optical and near-infrared surveys (§2.5, §4.1, Tables 2 and Figure 4). While most are members of the ONC that ionizes the Orion Nebula, both massive and low-mass members of deeply embedded populations around the OMC 1, OMC 1S and OMC 1N molecular cloud cores (but not the Orion Bar) are seen. Some of these were previously catalogued but others are discovered in the ACIS image (Table 4 and Figure 9). Hundreds of additional sources, mainly deeply embedded and VLM stars, should emerge in deeper *Chandra* exposures of the region. One of the unidentified sources, CXOONC 053524.6-052759, has an unusual combination of high and constant flux, hard spectrum, and no stellar counterpart. It may be a background transient neutron star binary system in quiescence.
3. The X-ray luminosity function of the full sample is approximately lognormal with mean

and standard deviation $\langle \log L_t \rangle = 29.4 \pm 0.7 \text{ erg s}^{-1}$ and X-ray to bolometric ratio $\langle \log L_t/L_{bol} \rangle = -3.9 \pm 0.7$ (§4.2 and Figure 10). The corresponding values for the full underlying population of ONC and Orion cloud stars is uncertain, as the means will drop with inclusion of undetected stars but increase with compensation for low energy absorption. Half of the observed X-ray emission is produced by the luminous O6 star $\theta^1\text{C Ori}$, and half by the remaining 1074 sources.

4. More than half of PMS stars with > 50 counts show intraday flux variations, often exhibiting dramatic flaring on timescale of 2 to > 12 hours, in our 13 and 10 hour observations (§4.2 and Figure 11). Half of the remaining sources showed different flux levels in the observations separated by 6 months.
5. There is no indication that the presence or absence of a circumstellar disk significantly affects the X-ray luminosities of PMS stars (Figure 10, middle panel).
6. The X-ray emission from 5 of the 7 B2–O6 stars constituting the Orion Trapezium shows surprising variability (§5.1, Table 5 and Figures 12 and 13). The $M \simeq 31 M_\odot$ O9.5 star $\theta^2\text{A Ori}$ (P 1993), in particular, exhibited multiple flares on timescales of hours during one observation. This result either requires an extraordinary flare from a lower mass stellar companion, or revision of the conventional model of OB stellar X-ray production in a myriad small-scale wind shocks. The X-ray emission from B0–B2 stars can be attributed to T Tauri companions, and their intrinsic emission is much weaker than predicted by the long-standing $\log L_s/L_{bol} = -7$ relation for wind-dominated OB stars.
7. The X-ray emission from intermediate-mass stars with spectral types from mid-B through A is consistent with emission from lower mass companions, although it requires that most stars have companions of a solar mass or greater (§5.2, Table 5, Figure 12). This supports well-accepted views that mid-B to A stars themselves are X-ray quiet, as they are insufficiently luminous to radiatively accelerate massive winds and lack outer convection zones that generate magnetic activity via a dynamo.
8. The average low mass G–M PMS star exhibits a moderate level of X-ray emission with $\langle \log L_s/L_{bol} \rangle = -4.2$, an order of magnitude below the ‘saturation’ level seen in magnetically active main sequence stars (§5.3, Figures 14–15). In contrast, plasma energies of PMS stars are often remarkably high, with $kT \simeq 5$ to >10 keV ($T \simeq 60$ to >120 MK) components often dominating the spectrum of even low-luminosity T Tauri stars. These high temperatures appear to violate the standard $L_x - T$ relation seen in the Sun and magnetically active stars. Abundance anomalies may also be present in

many of the brighter sources, consistent with recent high-resolution spectroscopic studies of nearby older magnetically active stars. Implications for the astrophysical origins of low mass PMS X-ray emission based on the absence of a statistical X-ray/rotation relation are discussed in Feigelson et al. (2002b).

9. We present the largest sample to date of X-ray detected very low mass pre-main sequence objects, most of which will probably evolve into brown dwarfs rather than stars (§5.4, Table 6, Figure 16). Though typically having low X-ray luminosities near our detection limit, the detected objects have X-ray surface fluxes near the saturation level $\log L_t/L_{bol} \simeq -3$ and exhibit flaring. The underlying VLM population appears to have X-ray properties similar to the lower mass PMS stars, indicating that the processes giving rise to magnetic activity in the PMS phase are independent of whether hydrogen burning will eventually turn-on in the stellar core. Magnetic activity appears to decline as the VLM objects evolve into older brown dwarfs, which is attributable to the drop in ionization fraction in their cooling atmospheres.

We thank: George Chartas and Konstantin Getman (Penn State) for expert assistance with data analysis; William Herbst (Wesleyan) for access to rotation data prior to publication; participants of the 12th Cool Star Workshop (including Gibor Basri of Berkeley, James Liebert of Arizona and Hans Zinnecker of Potsdam) for thoughtful comments; advice from Deepto Chakrabarty (MIT), David Cohen (Swarthmore) and George Pavlov (Penn State) concerning unusual sources; and Thierry Montmerle (Saclay) and the anonymous referee for helpful critiques of the entire manuscript. This work was principally supported by NASA grant NAS 8-38252 (Garmire, PI). Additional support was obtained from the Japan Society for the Promotion of Science (YT) and the Jet Propulsion Laboratory, California Institute of Technology, under contract with the National Aeronautics and Space Administration (SHP). The study benefited from on-line databases including SIMBAD, Astronomical Data Center and the Astrophysics Data System.

REFERENCES

- Ali, B. & Depoy, D. L. 1995, *AJ*, 109, 709
- Anders, E. & Grevesse, N. 1989, *Geochim. Cosmochim. Acta*, 53, 197
- Arnaud, K. A. 1996, in *Data Analysis Software and Systems V*, ed. G. H. Jacoby & J. Barnes (San Francisco:ASP), 17
- Babel, J. & Montmerle, T. 1997, *ApJ*, 485, L29
- Bally, J., Sutherland, R. S., Devine, D., & Johnstone, D. 1998, *AJ*, 116, 293
- Bally, J., O'Dell, C. R., & McCaughrean, M. J. 2000, *AJ*, 119, 2919
- Bally, J. & Reipurth, B. 2001, *ApJ*, 546, 299
- Berghöfer, T. W. & Schmitt, J. H. M. M. 1994, *A&A*, 292, L5
- Berghöfer, T. W. & Schmitt, J. H. M. M. 1994, *Science*, 265, 1689
- Berghöfer, T. W., Schmitt, J. H. M. M., Danner, R., & Cassinelli, J. P. 1997, *A&A*, 322, 167
- Bieging, J. H., Abbott, D. C., & Churchwell, E. B. 1989, *ApJ*, 340, 518
- Bradt, H. V. & Kelley, R. L. 1979, *ApJ*, 228, L33
- Brinkman, A. C. et al. 2001, *A&A*, 365, L324
- Burrows, A. et al. 1997, *ApJ*, 491, 856
- Caillault, J. & Zoonematkermani, S. 1989, *ApJ*, 338, L57
- Carpenter, J. M., Hillenbrand, L. A., & Skrutskie, M. F. 2001, *AJ*, 121, 3160
- Chandra Proposers' Observatory Guide, Version 3.0 (Cambridge:Chandra X-ray Center)
- Cohen, D. H., Cassinelli, J. P., & Macfarlane, J. J. 1997, *ApJ*, 487, 867
- D'Antona, F. & Mazzitelli, I. 1997, *Mem. Soc. Astron. Ital.*, 68, 807
- den Boggende, A. J. F., Mewe, R., Gronenschild, E. H. B. M., Heise, J., Grindlay, J. E., 1978, *A&A*, 62, 1
- Dobrzycki, A., Ebeling, H., Glotfelty, K., Freeman, P., Damiani, F., Elvis, M. & Calderwood, T. 1999, *Chandra detect 1.0 User Guide* (Cambridge:SAO)
http://asc.harvard.edu/ciao/documents_manuals.html

- Drake, J. J., Peres, G., Orlando, S., Laming, J. M., & Maggio, A. 2000, *ApJ*, 545, 1074
- Drake, J. J., Brickhouse, N. S., Kashyap, V., Laming, J. M., Huenemoerder, D. P., Smith, R., & Wargelin, B. J. 2001, *ApJ*, 548, L81
- Feigelson, E. D. & DeCampli W. M. 1981, *ApJ*, 243, L89
- Feigelson, E. D. & Kriss, G. A. 1981, *ApJ*, 248, L35
- Feigelson, E. D. 1990, in *Errors, Bias and Uncertainties in Astronomy*, ed. C. Jaschek & F. Murtagh (Cambridge:CUP), 213
- Feigelson, E. D., Giampapa, M. S., & Vrba, F. J. 1991, in *The Sun in Time*, ed. C. P. Sonnett, M. S. Giampapa & M. S. Matthews (Tucson:Univ. Arizona), 658
- Feigelson, E. D. 1992, in *Statistical Challenges in Modern Astronomy*, ed. E. D. Feigelson & G. J. Babu (New York:Springer), 221
- Feigelson, E. D., Casanova, S., Montmerle, T., & Guibert, J. 1993, *ApJ*, 416, 623
- Feigelson, E. D., Montmerle, T. 1999, *ARA&A*, 37, 363
- Feigelson, E. D., Garmire, G. & Pravdo, S. P. 2002, *ApJ*, 572, in press
- Feigelson, E. D., Gaffney, J. A. Garmire, G., Hillenbrand, L. A. 2002, *ApJ*, in preparation
- Feldmeier, A., Puls, J., & Pauldrach, A. W. A. 1997, *A&A*, 322, 878
- Felli, M., Taylor, G. B., Catarzi, M., Churchwell, E., & Kurtz, S. 1993, *A&AS*, 101, 127
- Fleming, T. A., Schmitt, J. H. M. M., & Giampapa, M. S. 1995, *ApJ*, 450, 401
- Freeman, P. E., Kashyap, V., Rosner, R., & Lamb, D. Q. 2002, *ApJS*, 138, 185
- Gagné, M. & Caillault, J. 1994, *ApJ*, 437, 361
- Gagné, M., Caillault, J.-P. & Stauffer, J. R., 1995, *ApJ*, 445, 280
- Garmire, G., Feigelson, E. D., Broos, P., Hillenbrand, L. A., Pravdo, S. H., Townsley, L., & Tsuboi, Y. 2000, *AJ*, 120, 1426
- Geier, S., Wendker, H. J. & Wisotzki, L. 1995, *A&A*, 229, 39
- Genzel, R., Reid, M. J., Moran, J. M., & Downes, D. 1981, *ApJ*, 244, 884
- Gezari, D. Y., Backman, D. E. & Werner, M. W. 1998, *ApJ*, 509, 283

- Giacconi, R., Murray, S., Gursky, H., Schreier, E., Tananbaum, H. 1972, ApJ, 178, 281
- Gizis, J. E., Monet, D. G., Reid, I. N., Kirkpatrick, J. D., Liebert, J., & Williams, R. J. 2000, AJ, 120, 1085
- Güdel, M., Guinan, E. F., & Skinner, S. L. 1997, ApJ, 483, 947
- Güdel, M. et al. 2001, A&A, 365, L336
- Hamaguchi, K., Terada, H., Bamba, A., & Koyama, K. 2000, ApJ, 532, 1111
- Harnden, F. R. et al. 1979, ApJ, 234, L51
- Herbst, W., Rhode, K. L., Hillenbrand, L. A., & Curran, G. 2000, AJ, 119, 261
- Herbst, W., Bailer-Jones, C. A. L., & Mundt, R. 2001, ApJ, 554, L197
- Hillenbrand, L. A. 1997, AJ, 113, 1733
- Hillenbrand, L. A., Strom, S. E., Calvet, N., Merrill, K. M., Gatley, I., Makidon, R. B., Meyer, M. R., & Skrutskie, M. F. 1998, AJ, 116, 1816
- Hillenbrand, L. A. & Carpenter, J. M. 2000, ApJ, 540, 236
- Howarth, I. D. & Prinja, R. K. 1989, ApJS, 69, 527
- Imanishi, K., Koyama, K. & Tsuboi, Y. 2001, ApJ, 557, 747
- Johnstone, D. & Bally, J. 1999, ApJ, 510, L49
- Jones, B. F. & Walker, M. F. 1988, AJ, 95, 1755
- Kahn, S. M., Leutenegger, M. A., Cottam, J., Rauw, G., Vreux, J., den Boggende, A. J. F., Mewe, R., & Güdel, M. 2001, A&A, 365, L312
- Kastner, J. H., Huenemoerder, D. P., Schulz, N. S., & Weintraub, D. A. 1999, ApJ, 525, 837
- Koyama, K., Ueno, S., Kobayashi, N. & Feigelson, E. D. 1996, PASJ, 48, L87
- Krishnamurthi, A., Reynolds, C. S., Linsky, J. L., Martín, E., & Gagné, M. 2001, AJ, 121, 337
- Ku, W. H.-M. & Chanan, G. A. 1979, ApJ, 234, L59
- Ku, W. H. -, Righini-Cohen, G., & Simon, M. 1982, Science, 215, 61

- Lada, C. J., Muench, A. A., Haisch, K. E., Lada, E. A., Alves, J. ;., Tollestrup, E. V., & Willner, S. P. 2000, AJ, 120, 3162
- Leggett, S. K. 1992, ApJS, 82, 351
- Leggett, S. K., Allard, F., Geballe, T. R., Hauschildt, P. H., & Schweitzer, A. 2001, ApJ, 548, 908
- Liebert, J., Kirkpatrick, J. D., Reid, I. N., & Fisher, M. D. 1999, ApJ, 519, 345
- Lis, D. C., Serabyn, E., Keene, J., Dowell, C. D., Benford, D. J., Phillips, T. G., Hunter, T. R., & Wang, N. 1998, ApJ, 509, 299
- Lohmann, P. & Wendker, H. J. 2000, Astron. Nach. 321, 81
- Lucas, P. W. & Roche, P. F. 2000, MNRAS, 314, 858
- Luhman, K. L., Rieke, G. H., Young, E. T., Cotera, A. S., Chen, H., Rieke, M. J., Schneider, G. & Thompson, R. I. 2000, ApJ, 540, 1016
- Lucy, L. B. & White, R. L. 1980, ApJ, 241, 300
- Mamajek, E. E., Lawson, W. A., & Feigelson, E. D. 2000, ApJ, 544, 356
- Mewe, R. 1991, A&A Rev., 3, 127
- Montmerle T., Koch-Miramond, L., Falgarone, E. & Grindlay, J. E. 1983, ApJ, 269, 182
- Montmerle, T., Grosso, N., Tsuboi, Y., & Koyama, K. 2000, ApJ, 532, 1097
- Morrison, R. & McCammon, D. 1983, ApJ, 270, 119
- Mundy, L. G., Looney, L. W. & Lada, E. A. 1995, ApJ, 452, L137
- Neuhäuser R., Torres G., Sterzik, M.F. & Randich S. 1997, A&A, 325, 647
- Neuhäuser, R. et al. 1999, A&A, 343, 883
- O'Dell, C. R. & Wen, Z. 1994, ApJ, 436, 194
- O'Dell, C. R. & Wong, S. K. 1996, AJ, 111, 846
- Owociki, S. P. & Cohen, D. H. 1999, ApJ, 520, 833
- Pallavicini, R., Golub, L., Rosner, R., Vaiana, G. S., Ayres, T., & Linsky, J. L. 1981, ApJ, 248, 279

- Parenago, P. P. 1954, *Trudy Gosudarstvennogo Astron. Inst.*, 25, 1
- Peres, G., Orlando, S., Reale, F., Rosner, R., & Hudson, H. 2000, *ApJ*, 528, 537
- Pravdo, S. H. & Marshall, F. E. 1981, *ApJ*, 248, 591
- Preibisch, T. 1997, *A&A*, 320, 525
- Preibisch, T., Balega, Y., Hofmann, K., Weigelt, G., & Zinnecker, H. 1999, *New Astronomy*, 4, 531
- Preibisch, T. & Zinnecker, H. 2001, *AJ*, 122, 866
- Prigozhin, G., Kissell, S., Bautz, M., Grant, C., LaMarr, B., Foster, R. & Ricker, G. 2000, *Proc. SPIE*, 4012, 720
- Prosser, C. F., Stauffer, J. R., Hartmann, L., Soderblom, D. R., Jones, B. F., Werner, M. W., & McCaughrean, M. J. 1994, *ApJ*, 421, 517
- Randich, S. 1997, *Memorie della Societa Astronomica Italiana*, 68, 971
- Reale, F., Peres, G. & Orlando, S. 2001, *ApJ*, 557, 906
- Rodriguez-Franco, A., Martin-Pintado, J. & Wilson, T. L. 1999, *A&A*, 351, 1103
- Rosner, R., Tucker, W. H., & Vaiana, G. S. 1978, *ApJ*, 220, 643
- Rutledge, R. E., Basri, G., Martín, E. L., & Bildsten, L. 2000, *ApJ*, 538, L141
- Rutledge, R. E., Bildsten, L., Brown, E. F., Pavlov, G. G., & Zavlin, V. E. 2001, *ApJ*, 551, 921
- Savage, B. D. & Mathis, J. S. 1979, *ARA&A*, 17, 73
- Scargle, J. 1998, *ApJ*, 504, 405
- Schmitt, J. H. M. M., Golub, L., Harnden, F. R., Maxson, C. W., Rosner, R., & Vaiana, G. S. 1985, *ApJ*, 290, 307
- Schulz, N. S., Canizares, C. R., Huenemoerder, D., & Lee, J. C. 2000, *ApJ*, 545, L135
- Schulz, N. S., Canizares, C., Huenemoerder, D., Kastner, J. H., Taylor, S. C., & Bergstrom, E. J. 2001, *ApJ*, 549, 441
- Shu, F. H., Shang, H., Glassgold, A. E., & Lee, T. 1997, *Science*, 277, 1475

- Simon, M., Close, L. M., & Beck, T. L. 1999, *AJ*, 117, 1375
- Simon, T., Drake, S. A., & Kim, P. D. 1995, *PASP*, 107, 1034
- Smith, M. A. & Robinson, R. D. 1999, *ApJ*, 517, 866
- Stahler, S. W. 1983, *ApJ*, 274, 822
- Stassun, K. G., Mathieu, R. D., Mazeh, T., & Vrba, F. J. 1999, *AJ*, 117, 2941
- Stassun, K. G., Mathieu, R. D., Vrba, F. J., Mazeh, T., & Henden, A. 2001, *AJ*, 121, 1003
- Stelzer, B. & Neuhäuser, R. 2001, *A&A*, 377, 538
- Sterzik, M. F., Alcalá, J. M., Neuhäuser, R., & Schmitt, J. H. M. M. 1995, *A&A*, 297, 418
- Townsley, L. K., Broos, P. S., Garmire, G. P., & Nousek, J. A. 2000, *ApJ*, 534, L139
- Townsley, L. K., Broos, P. S., Nousek, J. A., & Garmire, G. P. 2002, *Nucl. Instr. Methods*, in press (astro-ph/0111031)
- Tsuboi, Y., Koyama, K., Murakami, H., Hayashi, M., Skinner, S., & Ueno, S. 1998, *ApJ*, 503, 894
- Tsuboi, Y., Imanishi, K., Koyama, K., Grosso, N., & Montmerle, T. 2000, *ApJ*, 532, 1089
- Tsuboi, T., Koyama, K., Hamaguchi, K., Tatematsu, K., Sekimoto, Y., Bally, J., & Reipurth, B. 2001, *ApJ*, 554, 734
- Vilhu, O. & Walter, F. M. 1987, *ApJ*, 321, 958
- Waldron, W. L. & Cassinelli, J. P. 2001, *ApJ*, 548, L45
- Walter, F. M. & Kuhi, L. V. 1981, *ApJ*, 250, 254
- Walter F. M., Brown, A., Mathieu, R. D., Myers, P. C. & Vrba, F. J., 1988, *AJ*, 96, 297
- Walter, F. M. & Barry, D. C. 1991, in *The Sun in Time*, ed. C. P. Sonnett, M. S. Giampapa & M. S. Matthews (Tucson:Univ. Arizona), 633
- Weisskopf, M. C., Brinkman, B., Canizares, C., Garmire, G., Murray, S., & Van Speybroeck, L. P. 2001, *PASP*, in press
- Yamauchi, S. & Koyama, K. 1993, *ApJ*, 405, 268
- Yamauchi, S., Koyama, K., Sakano, M., Okada, K. 1996, *PASJ*, 48, 719

Zinnecker, H. & Preibisch, T. 1994, A&A, 292, 152

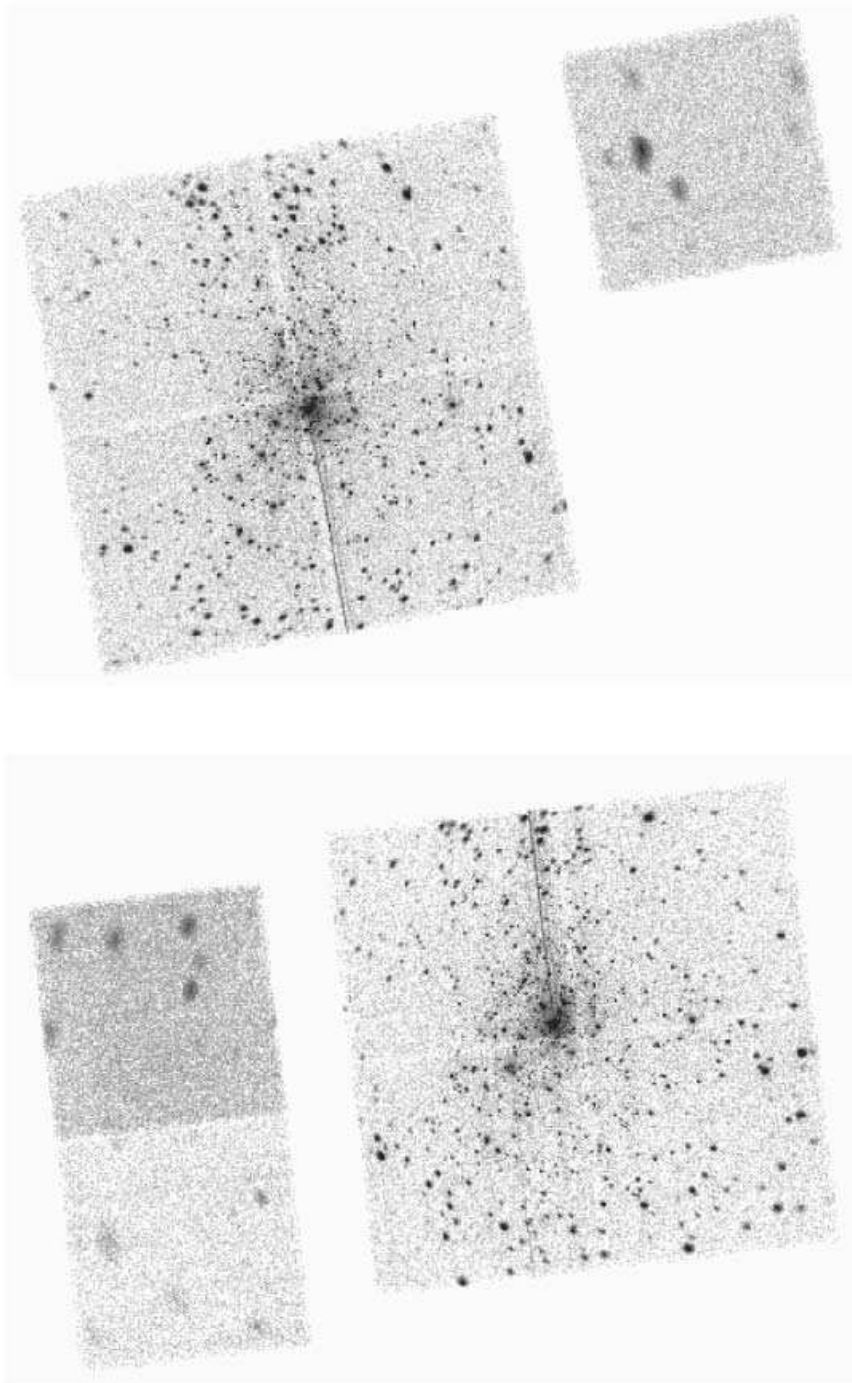


Fig. 1.— Low resolution views of the (top) October 1999 and (bottom) April 2000 ACIS-I observations of the Orion Nebula Cluster after data selection. North is up and East is to the left. Gray hues are scaled to the log of the counts in each $4''$ element. Results from the spectroscopic array chips outside of the square ACIS-I array are not discussed in this or the accompanying studies.

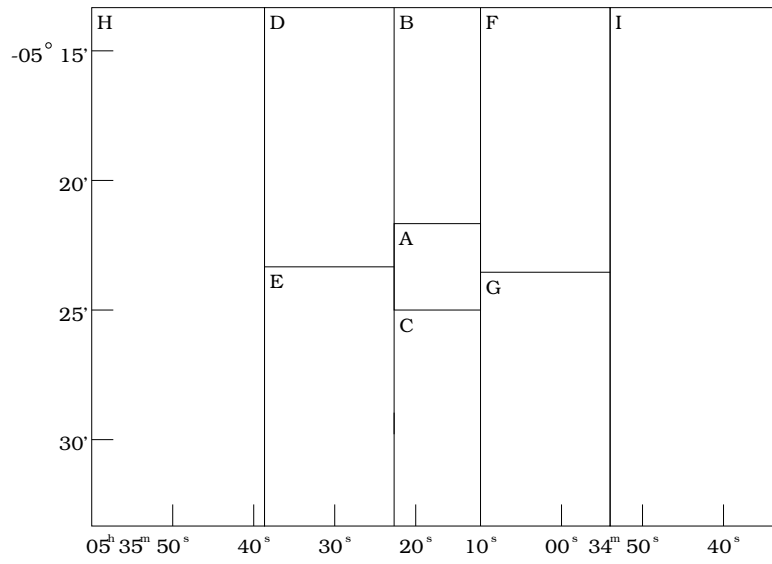


Fig. 2.— Guide to Figure 3.

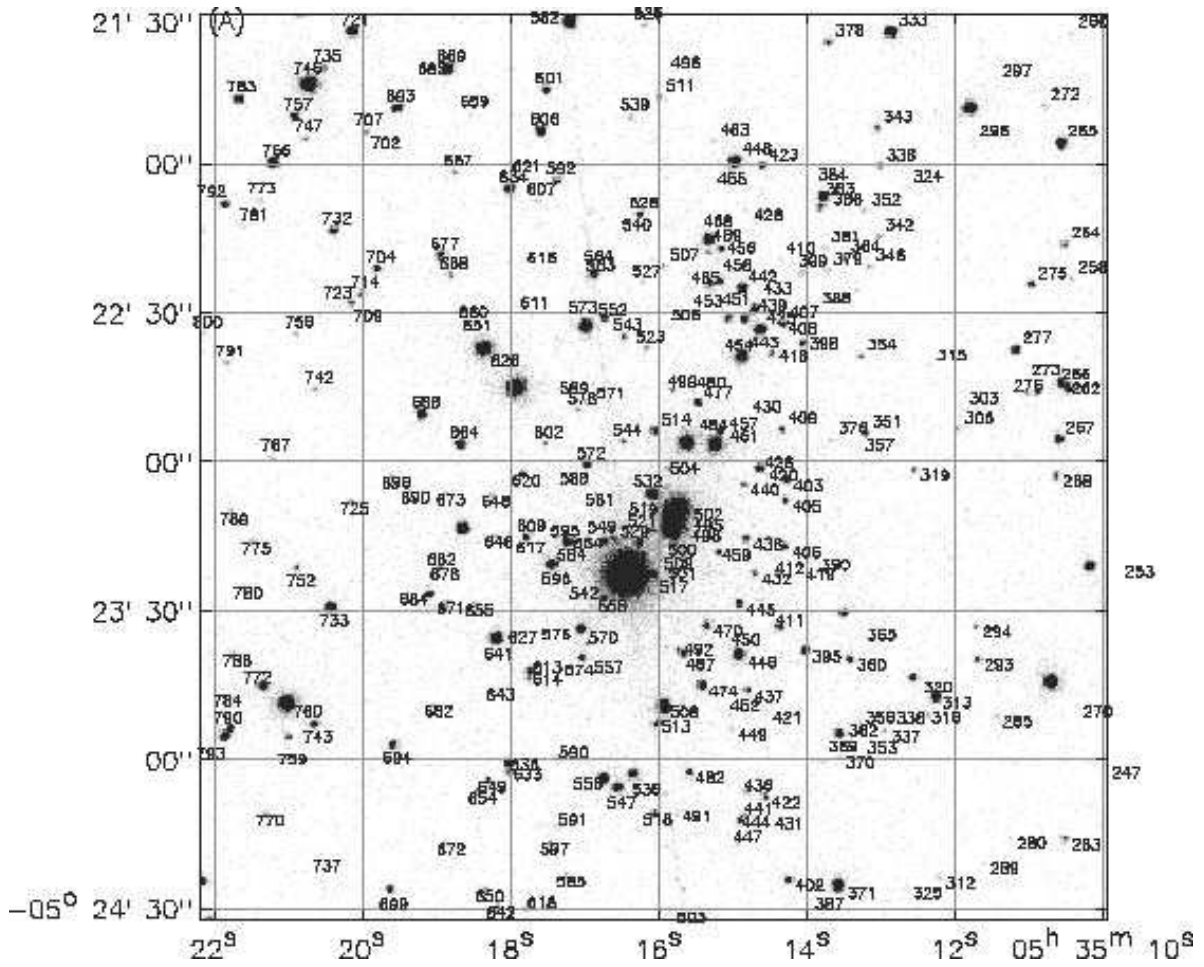
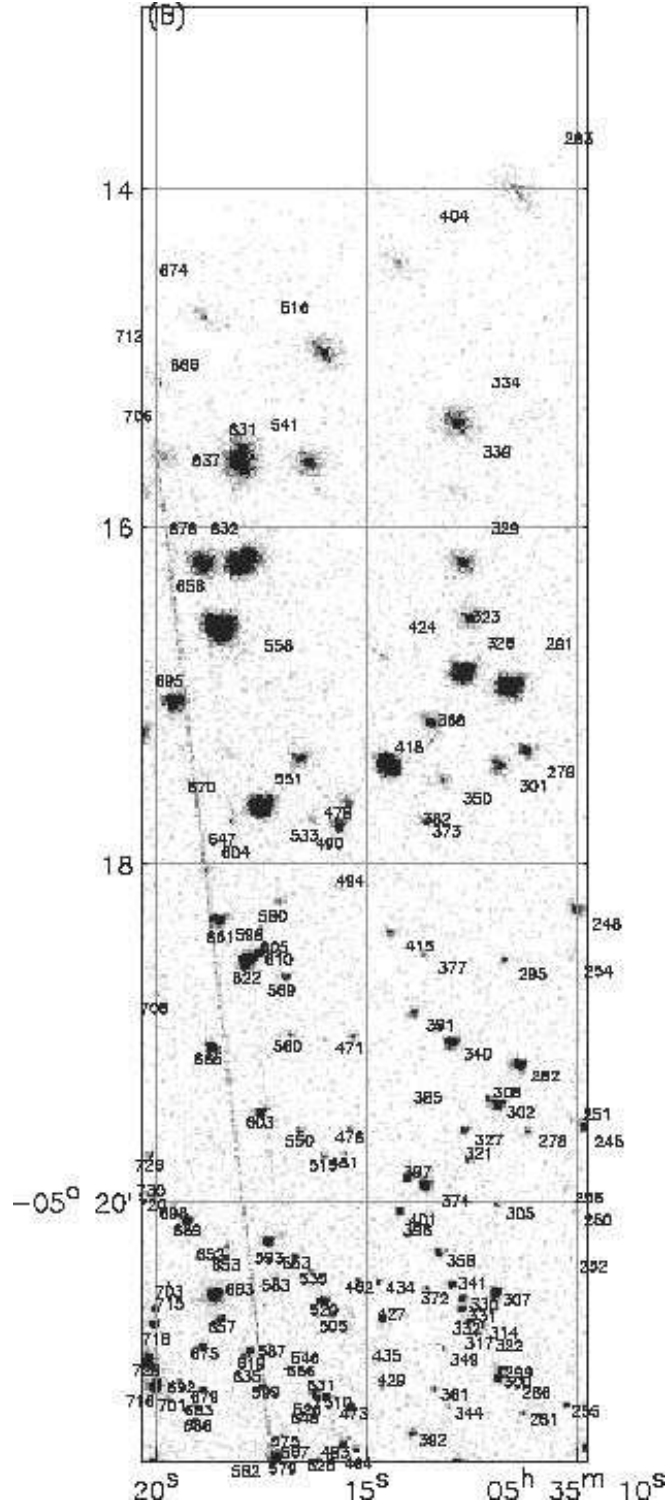
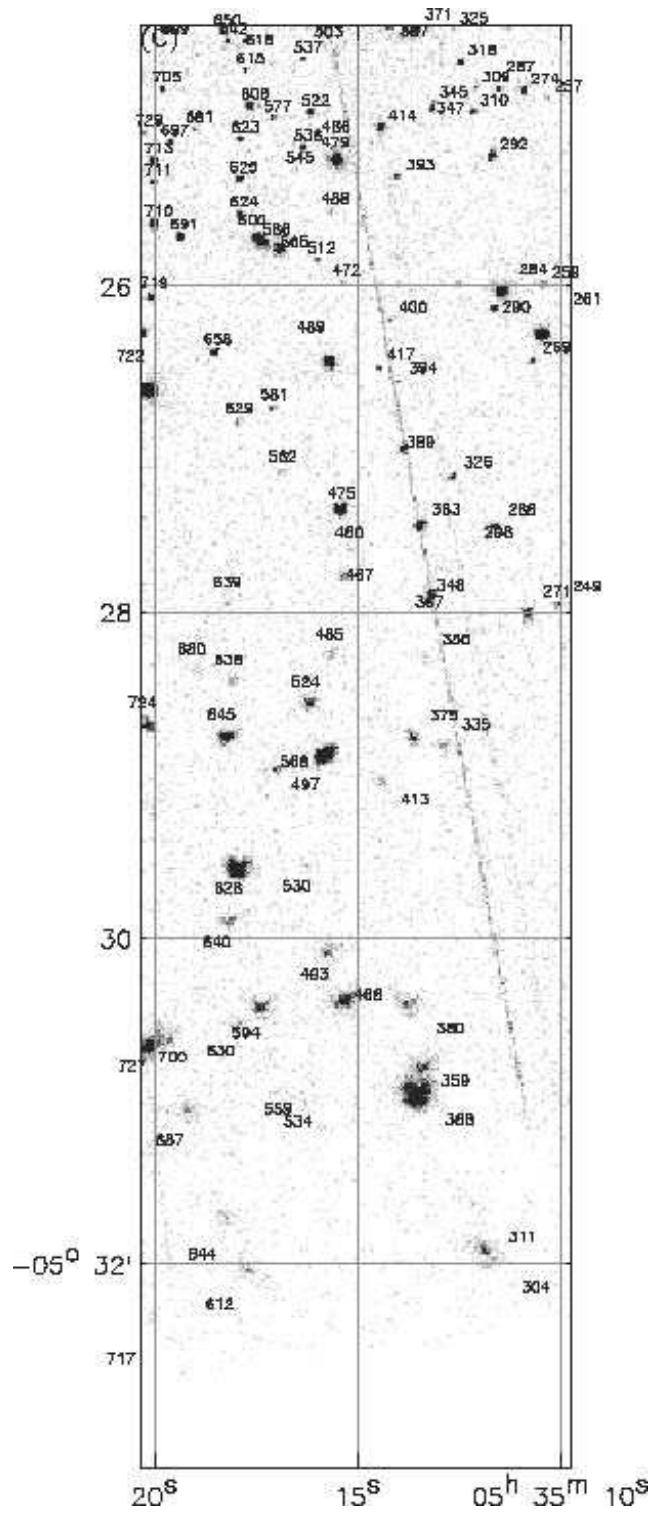
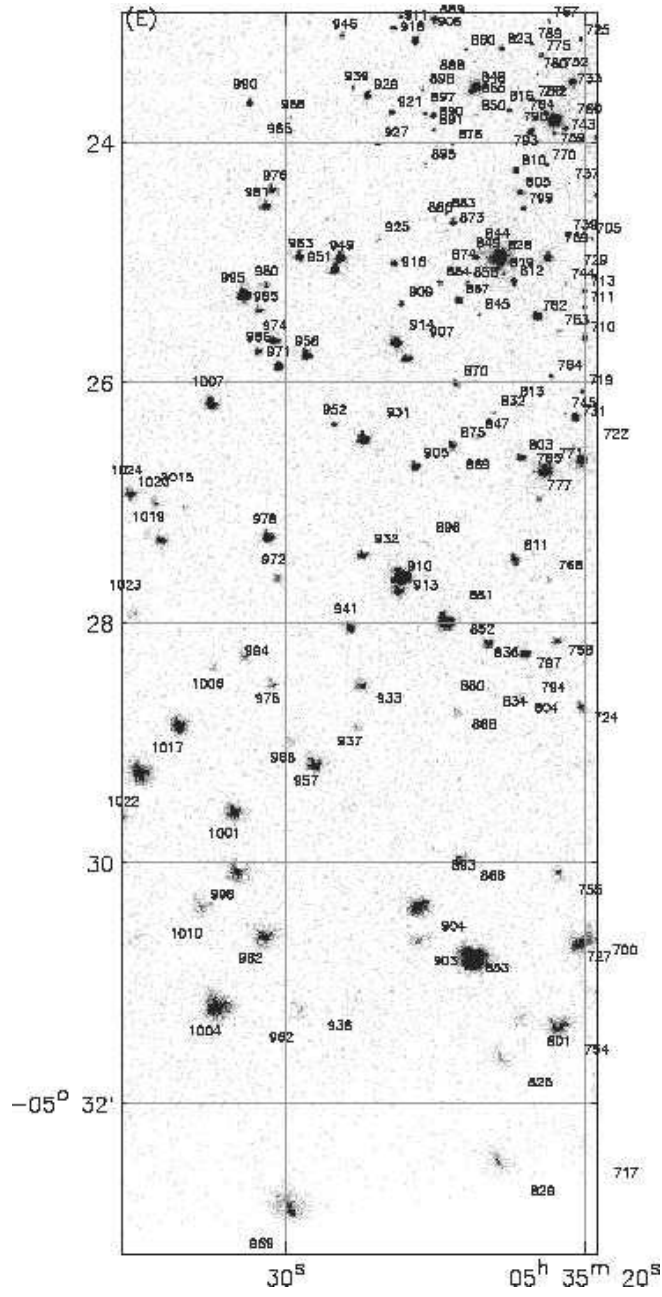
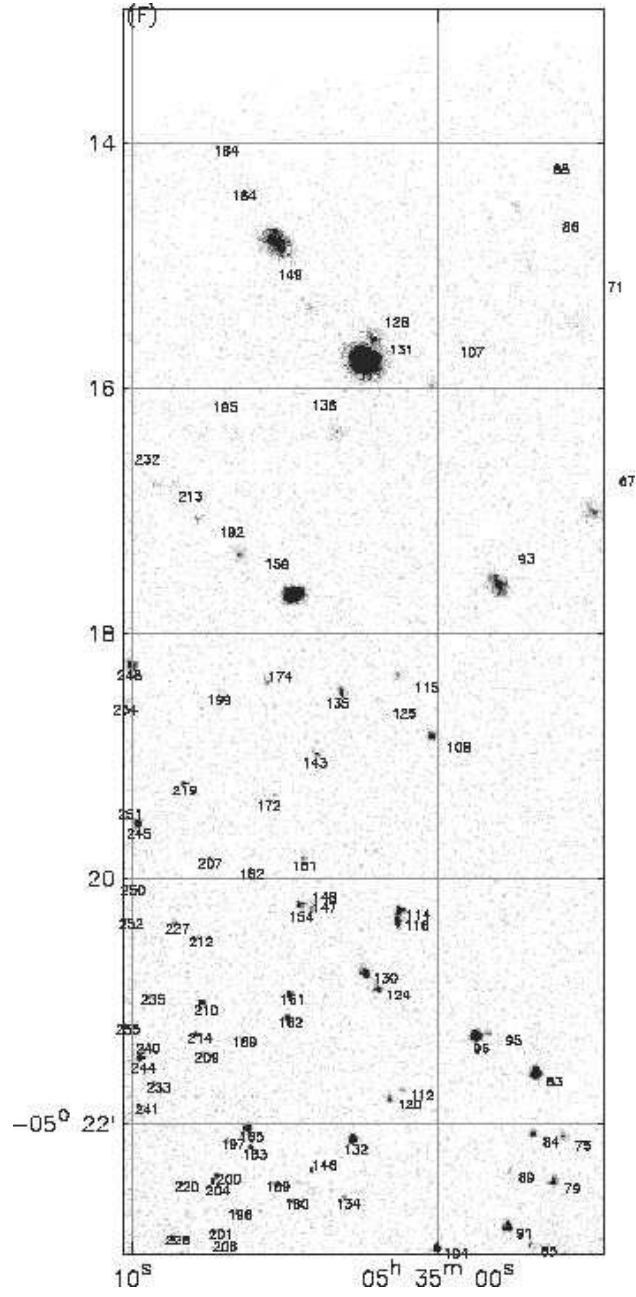


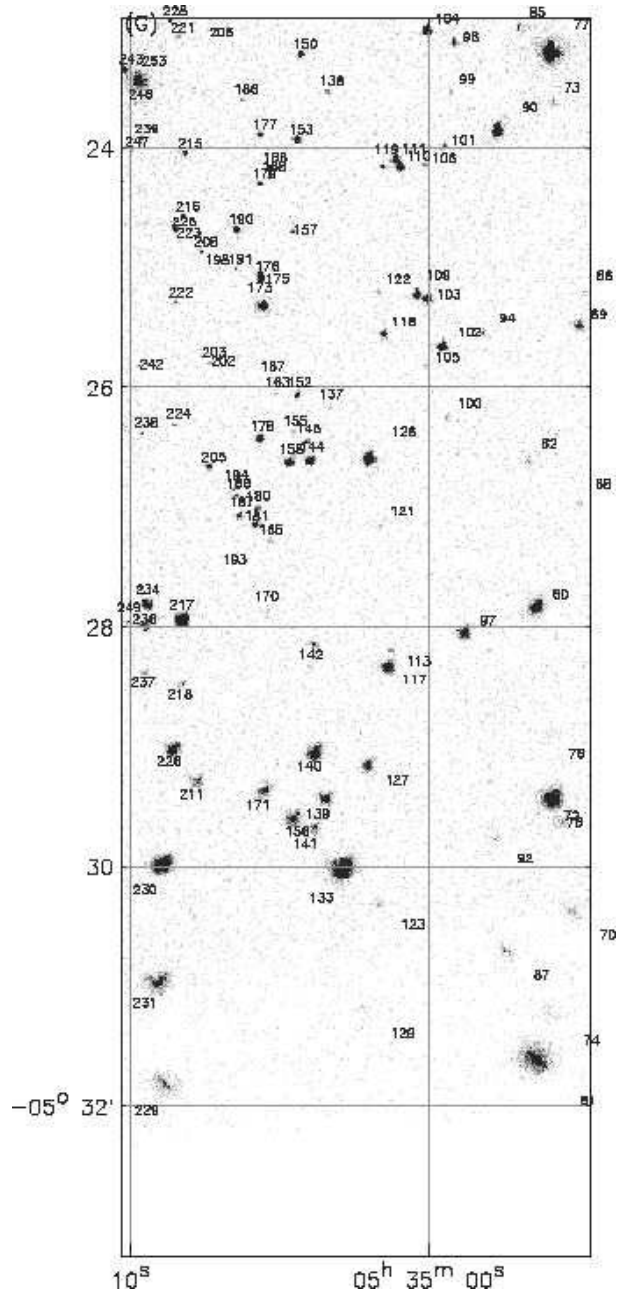
Fig. 3.— (a)-(i) Expanded view of the merged ACIS image with sources indicated.

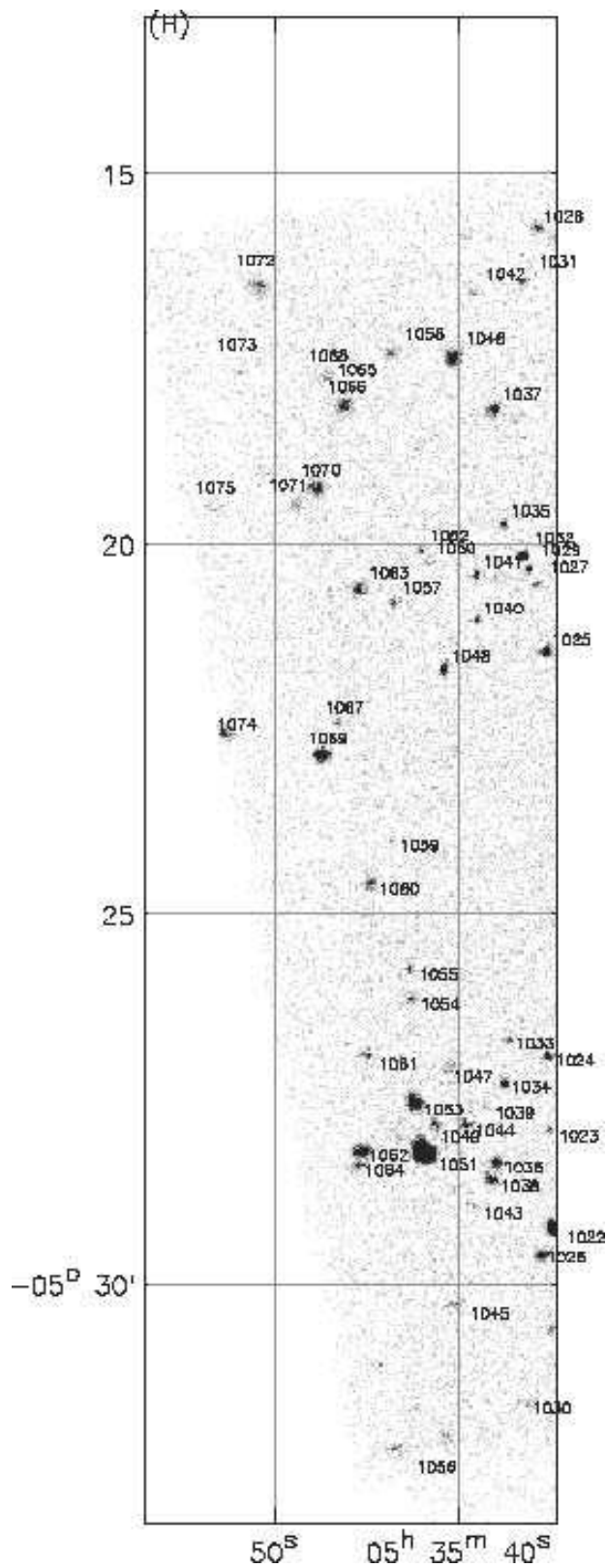


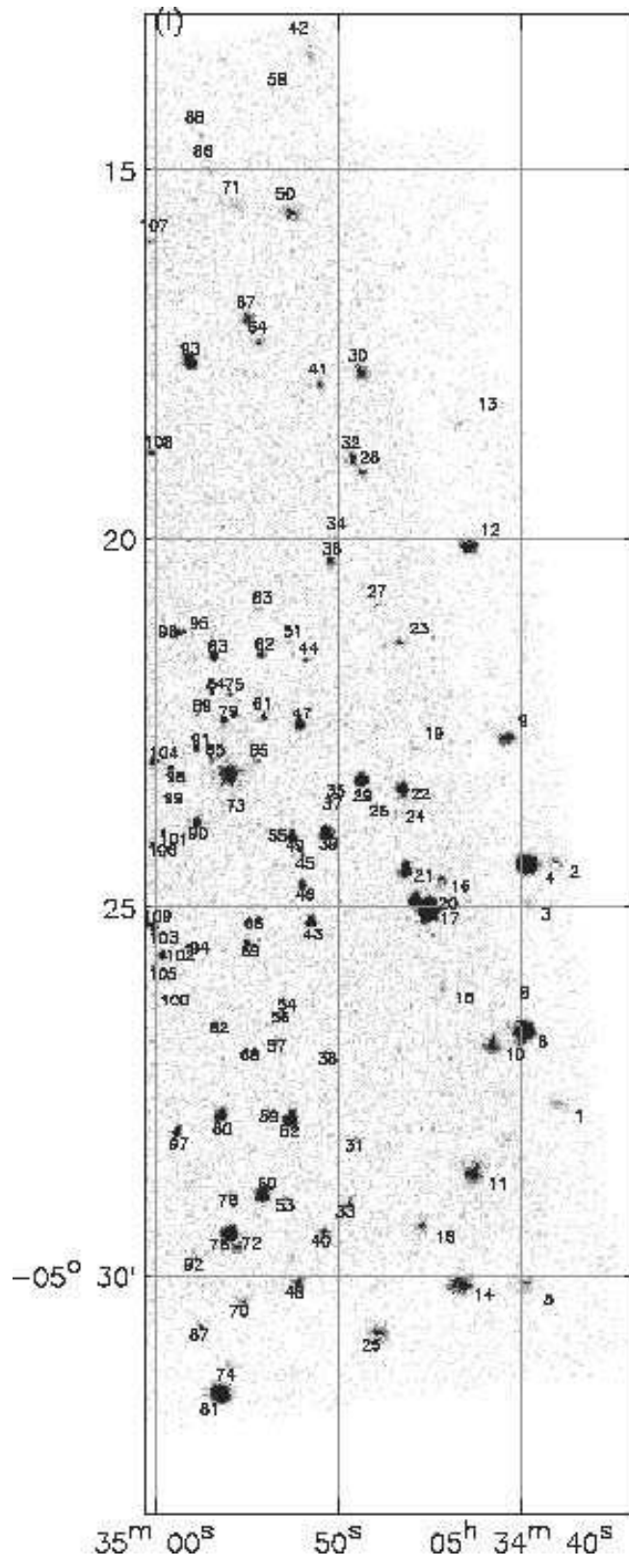












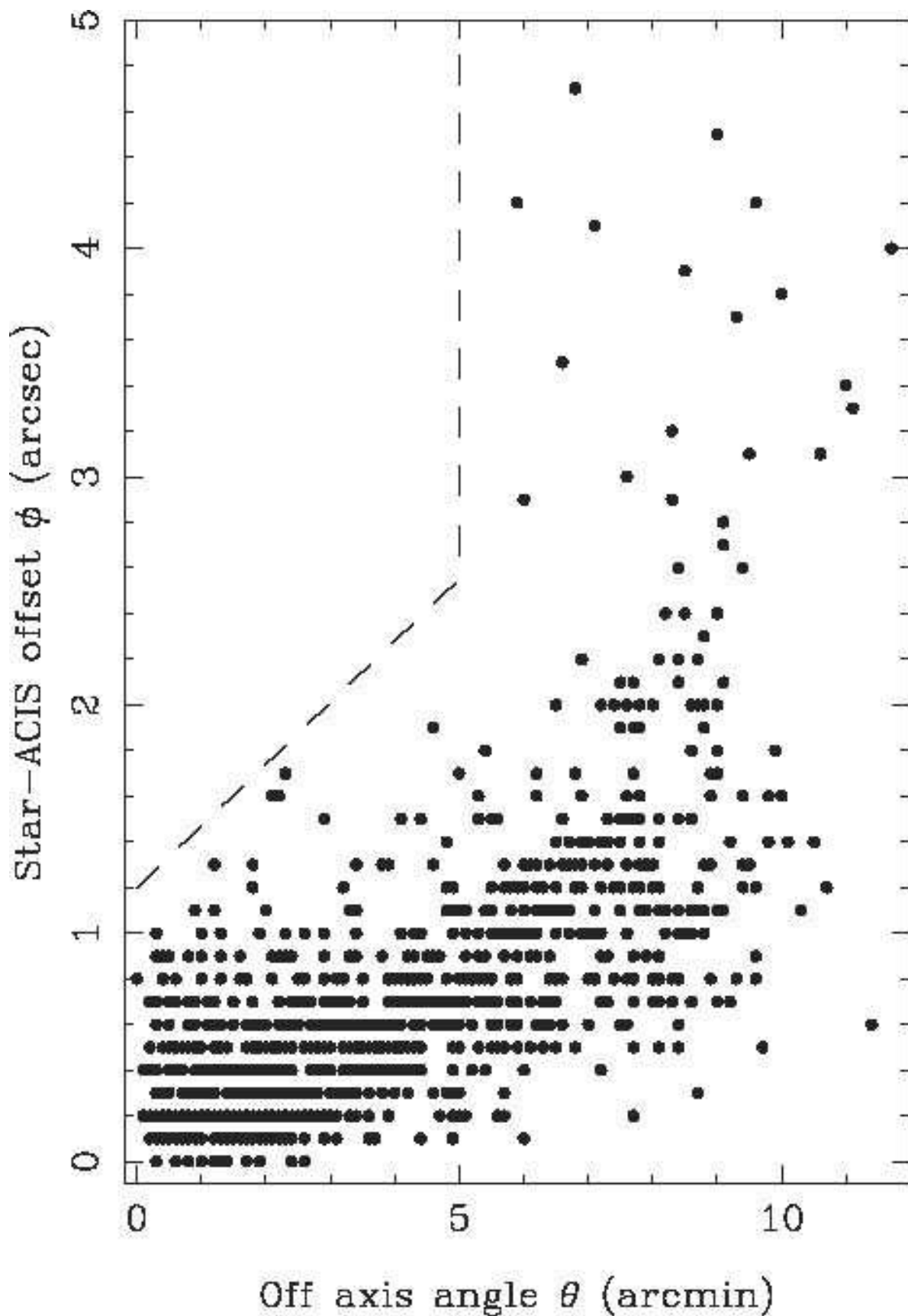


Fig. 4.— Positional offsets ϕ (in arcsec) between ACIS sources and proposed stellar counterparts plotted against the off-axis angle θ (in arcmin). Sources falling to the left of the

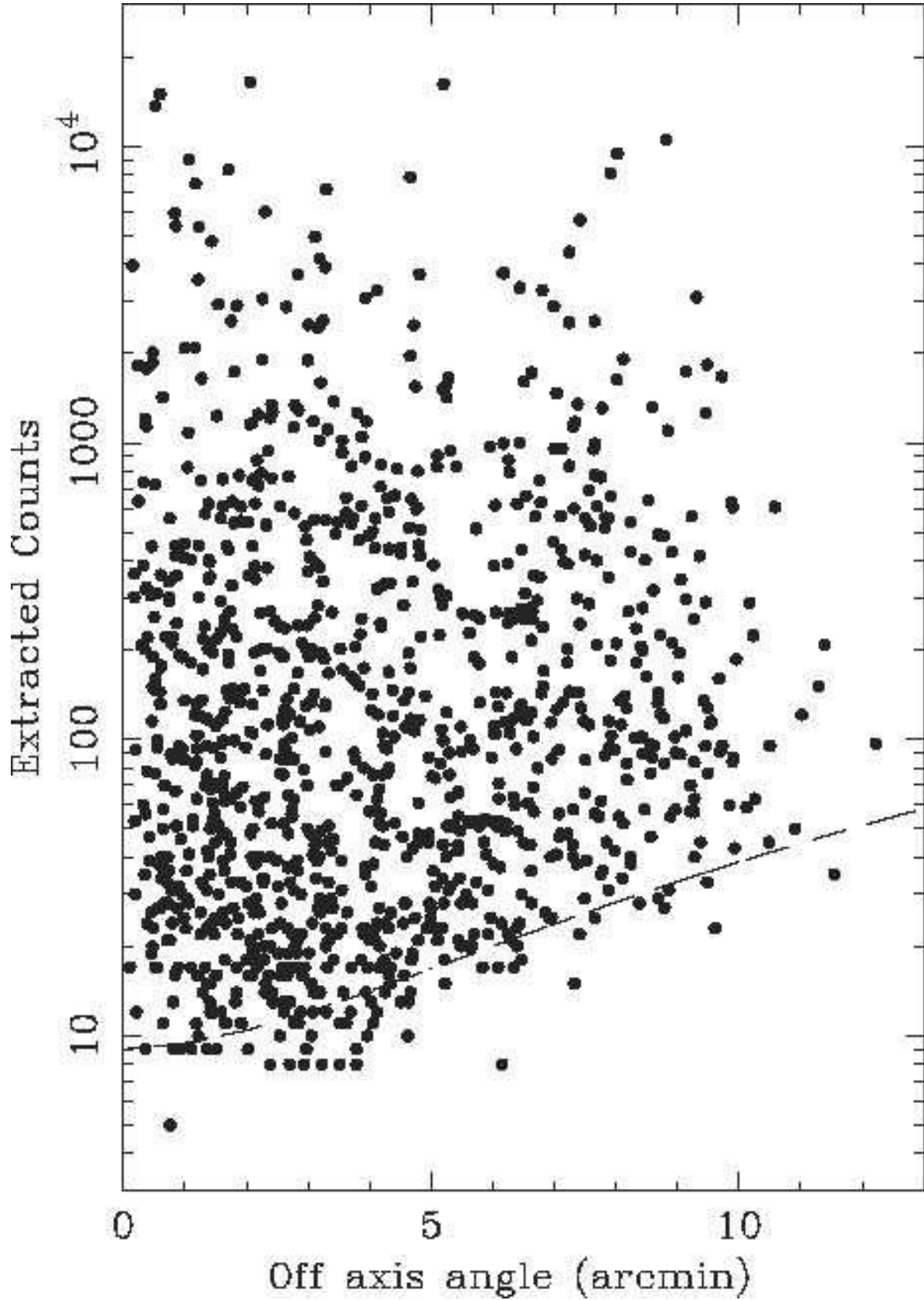


Fig. 5.— Distribution of extracted counts for ONC sources as a function of off-axis angle in the ACIS-I detector. The dashed curve shows the estimated completeness limit.

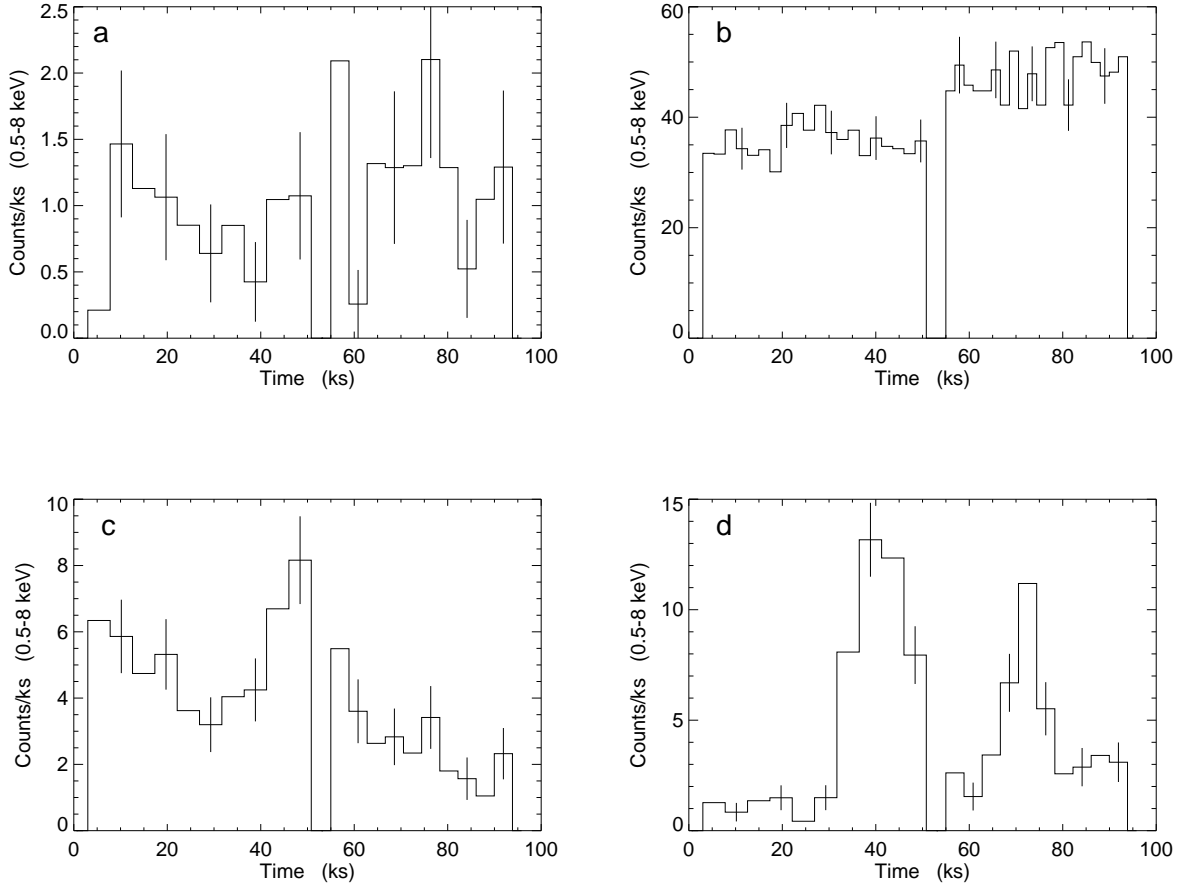


Fig. 6.— Examples of ACIS ONC variability classes: (a) Constant (source #149 = JW 240, $0.4 M_{\odot}$); (b) Long Term Variability (#663 = JW 595, $3 M_{\odot}$); (c) Possible Flare (# 466 = CHS 8664, uncharacterized $2\mu\text{m}$ source); and (d) Flare (#657 = JW 594, $M=0.2 M_{\odot}$). The ordinate gives counts ks^{-1} in the total $0.5 - 8$ keV band. Error bars show typical \sqrt{N} uncertainties. The abscissa gives time in ks, with 10 (20) bins per observation for weaker (stronger) sources. For graphical convenience, the two observations are plotted consecutively separated by 5 ks, though in fact they are separated by $\simeq 6$ months.

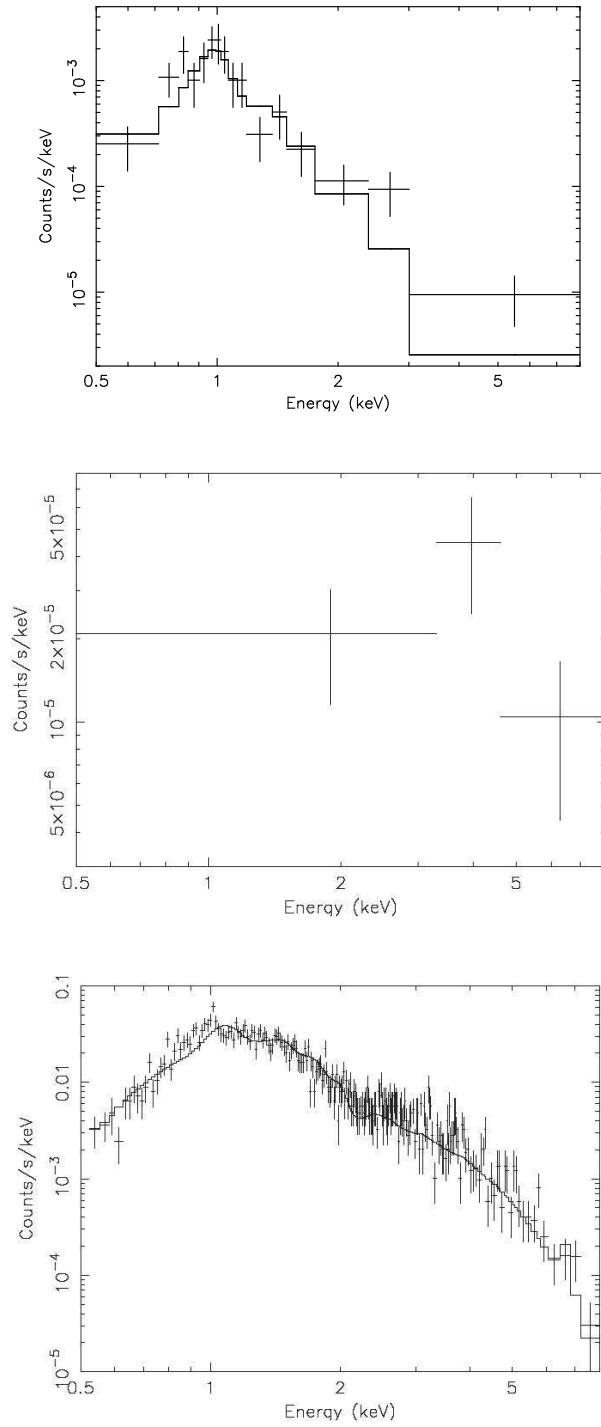


Fig. 7.— Examples of ACIS ONC X-ray spectra: (top) source #180; (middle) source # 388; and (bottom) source #573. See §2.8 for description.

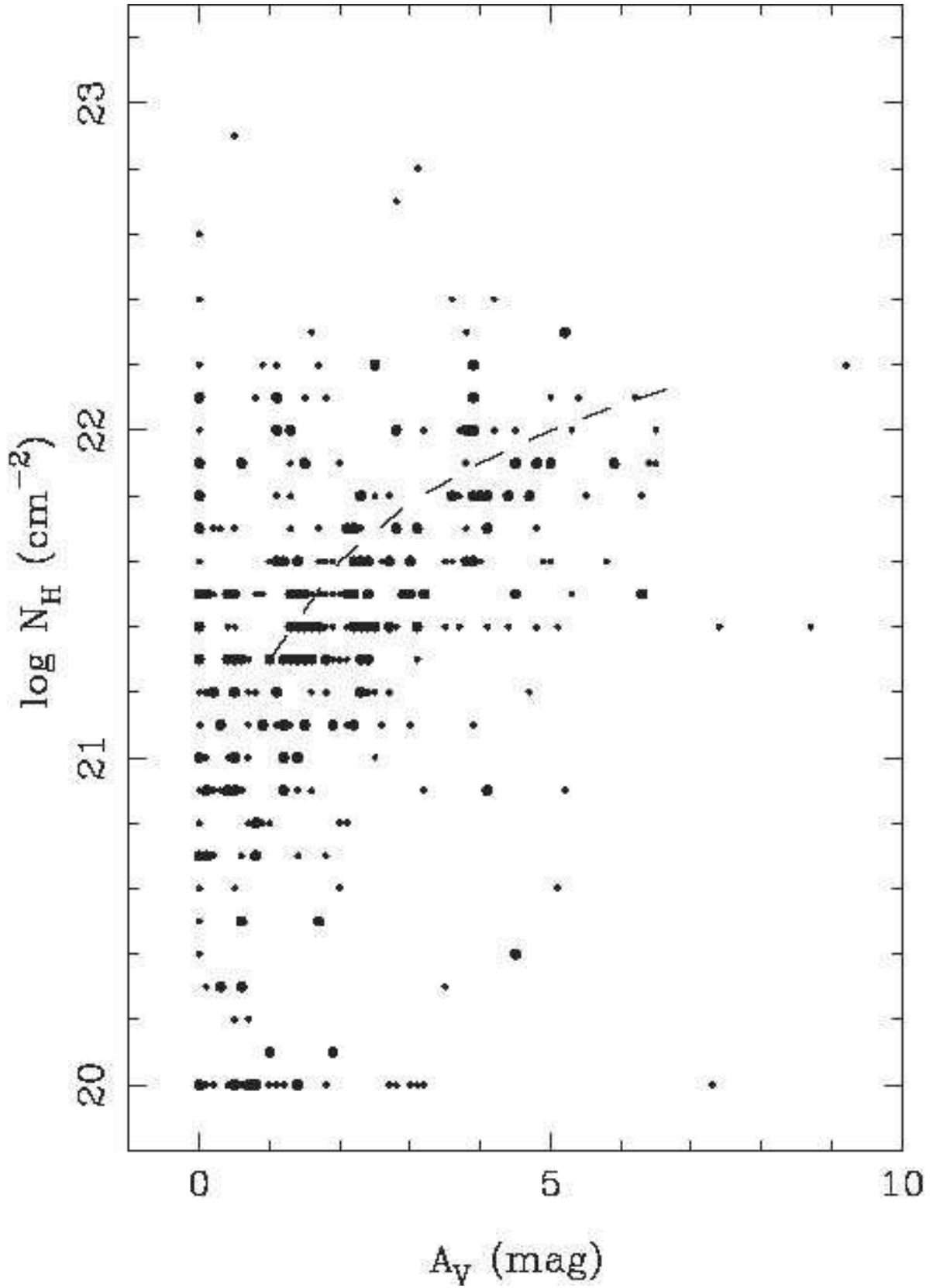


Fig. 8.— Plot of intervening column density derived from X-ray spectral analysis *vs.* visual absorption derived from optical studies for sources with both quantities known. Large circles are bright sources with > 500 counts while small circles are sources with $30 - 500$ counts.

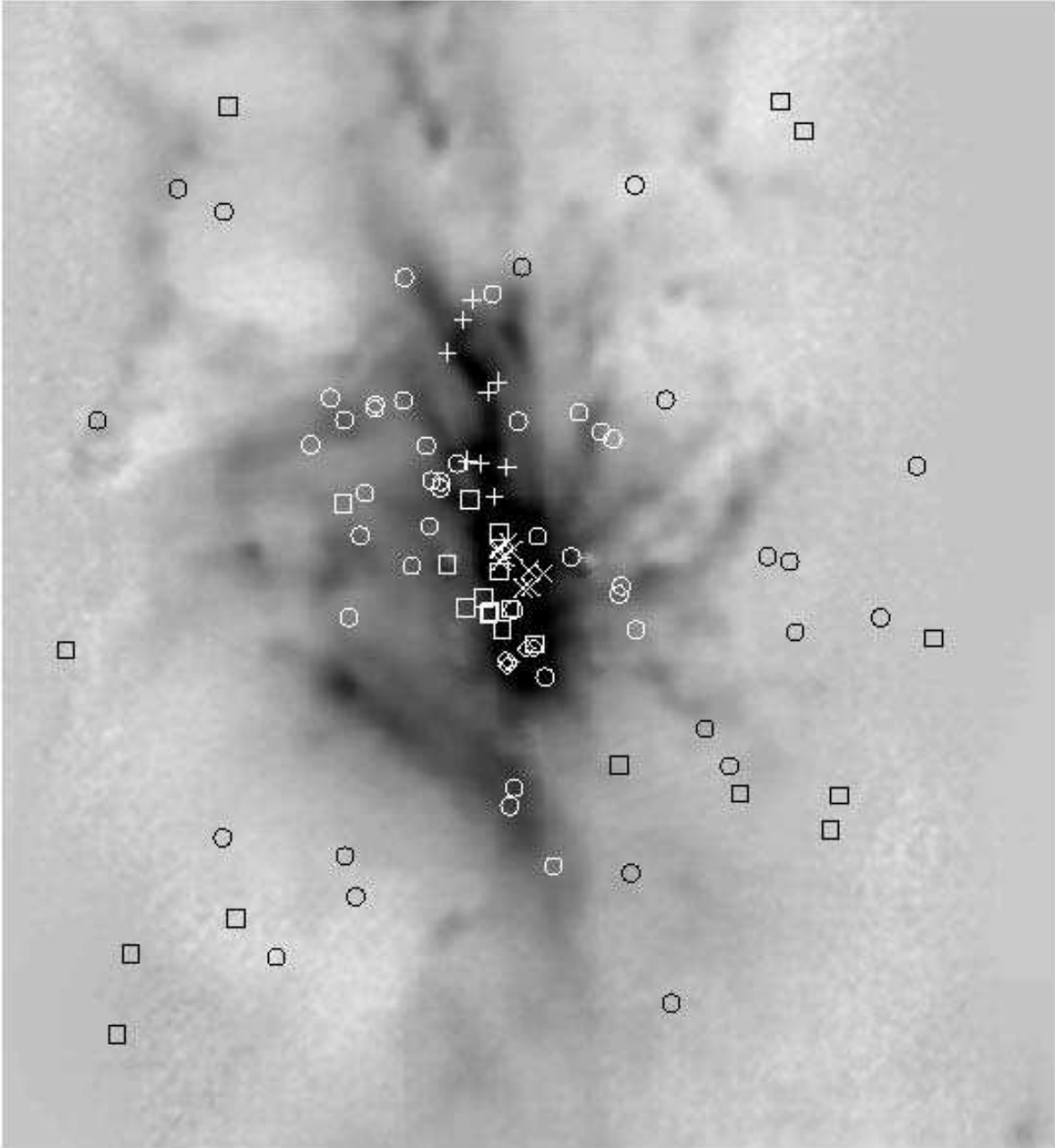


Fig. 9.— ACIS sources without stellar counterparts plotted on a greyscale SCUBA submillimeter map of the Orion Nebula showing the distribution of dense molecular material over a $17.6' \times 16.3'$ region (Johnstone & Bally 1999). The ACIS sources are coded by our suggested classification: lightly absorbed members of the ONC or other Orion OB association (squares); embedded stars associated with the OMC 1 = Orion KL core (crosses), OMC 1S = Orion S core (diamonds), and OMC 1N core (plusses); and dispersed absorbed sources with both embedded stars and Galactic and/or extragalactic background sources (circles).

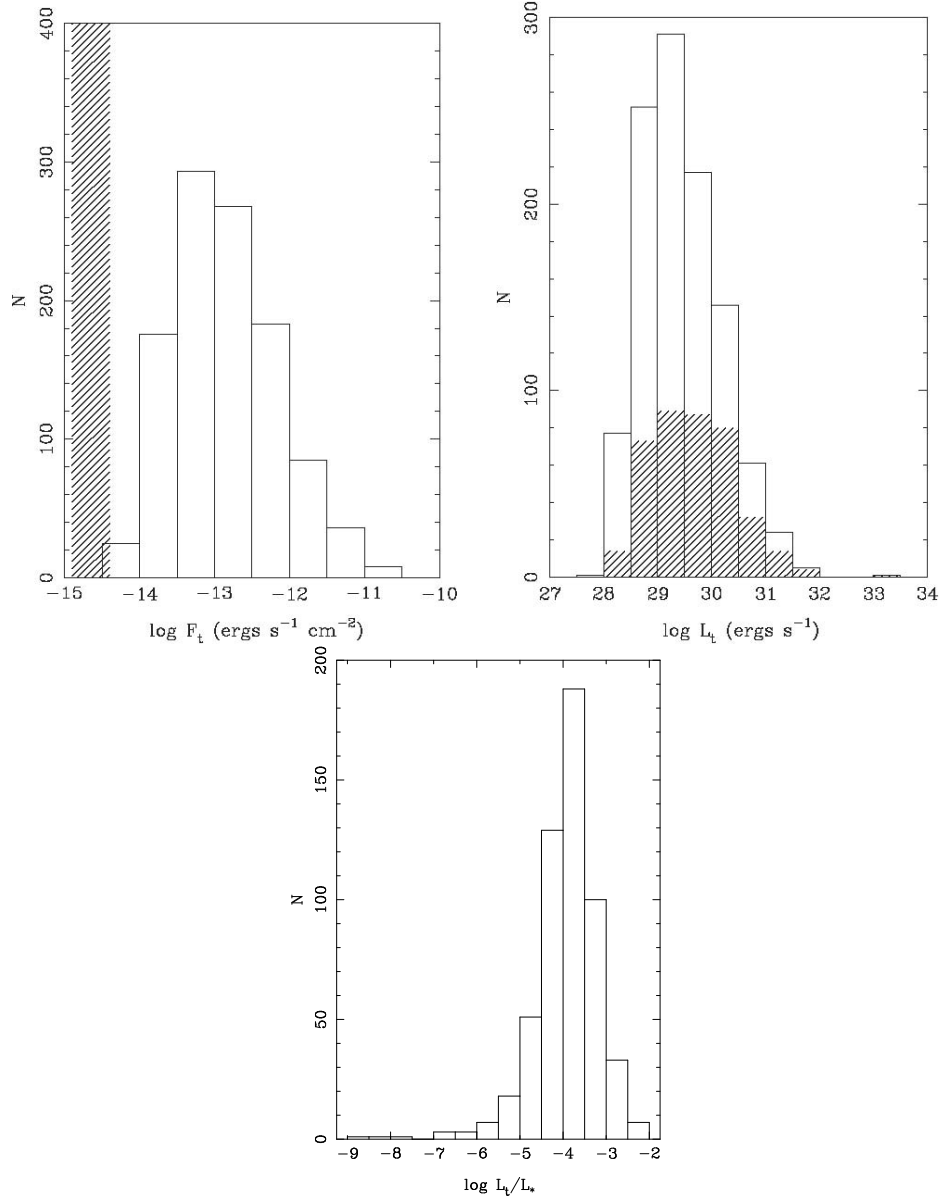


Fig. 10.— Distributions of X-ray emission (0.5 – 8 keV band) for the ACIS population: (left) flux with hatching indicating the completeness limit; (middle) luminosity with hatching indicating stars with K -band excess disks; and (right) X-ray to stellar bolometric luminosity ratio for well-characterized stars (Hillenbrand 1997).

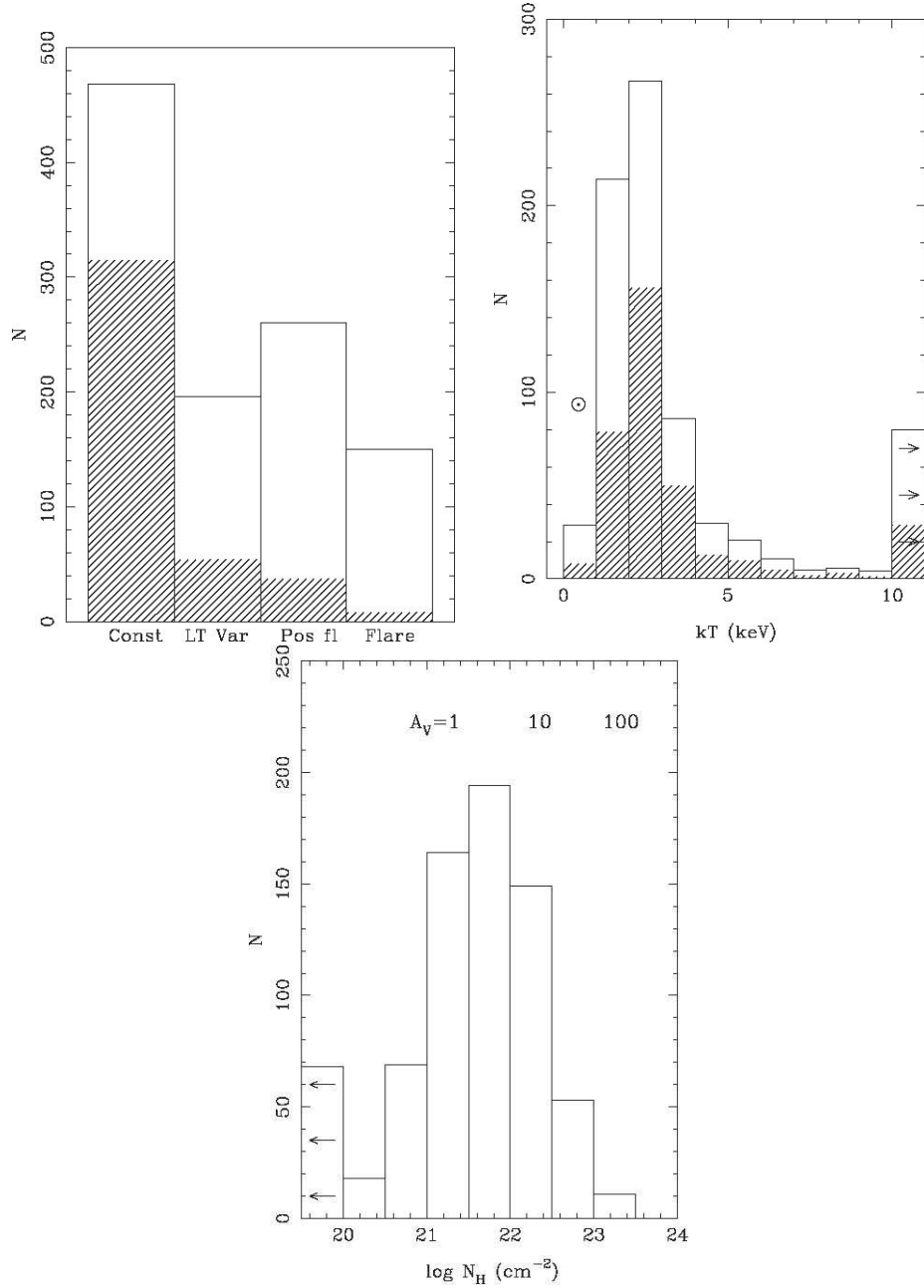
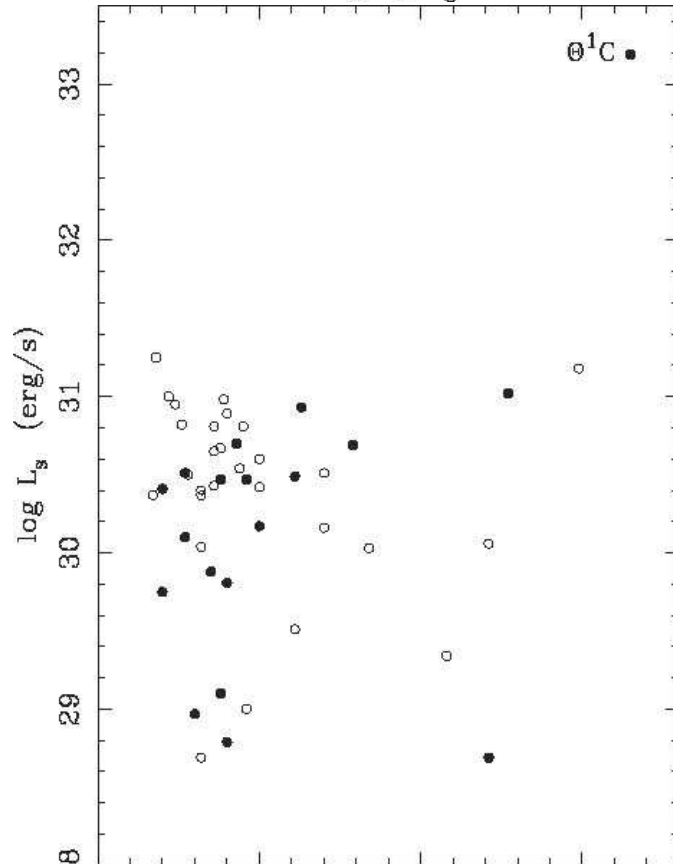
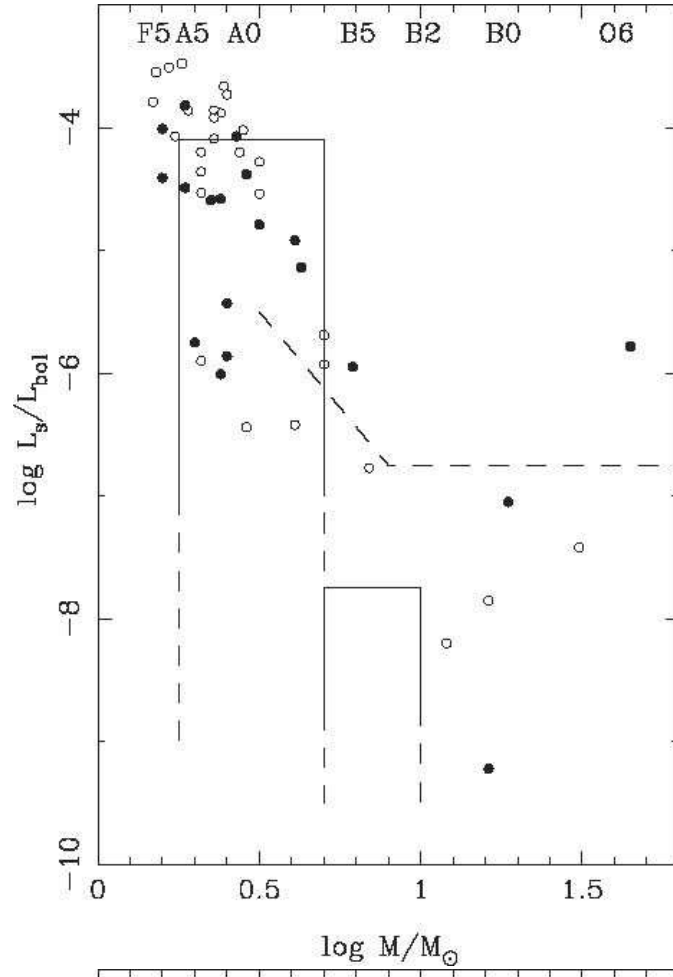


Fig. 11.— Distributions of X-ray variability and spectral properties of the ACIS sources: (left) variability classes with hatching indicating sources with < 50 extracted counts; (middle) plasma energies with hatching indicating sources with intraday variability, where \odot indicates the characteristic X-ray temperature of the contemporary flaring Sun; and (right) absorbing column densities with corresponding visual absorptions. Only sources with ≥ 30 counts are included for the spectral parameters. Bins with arrows indicate sources with very high plasma energies or very low column densities.



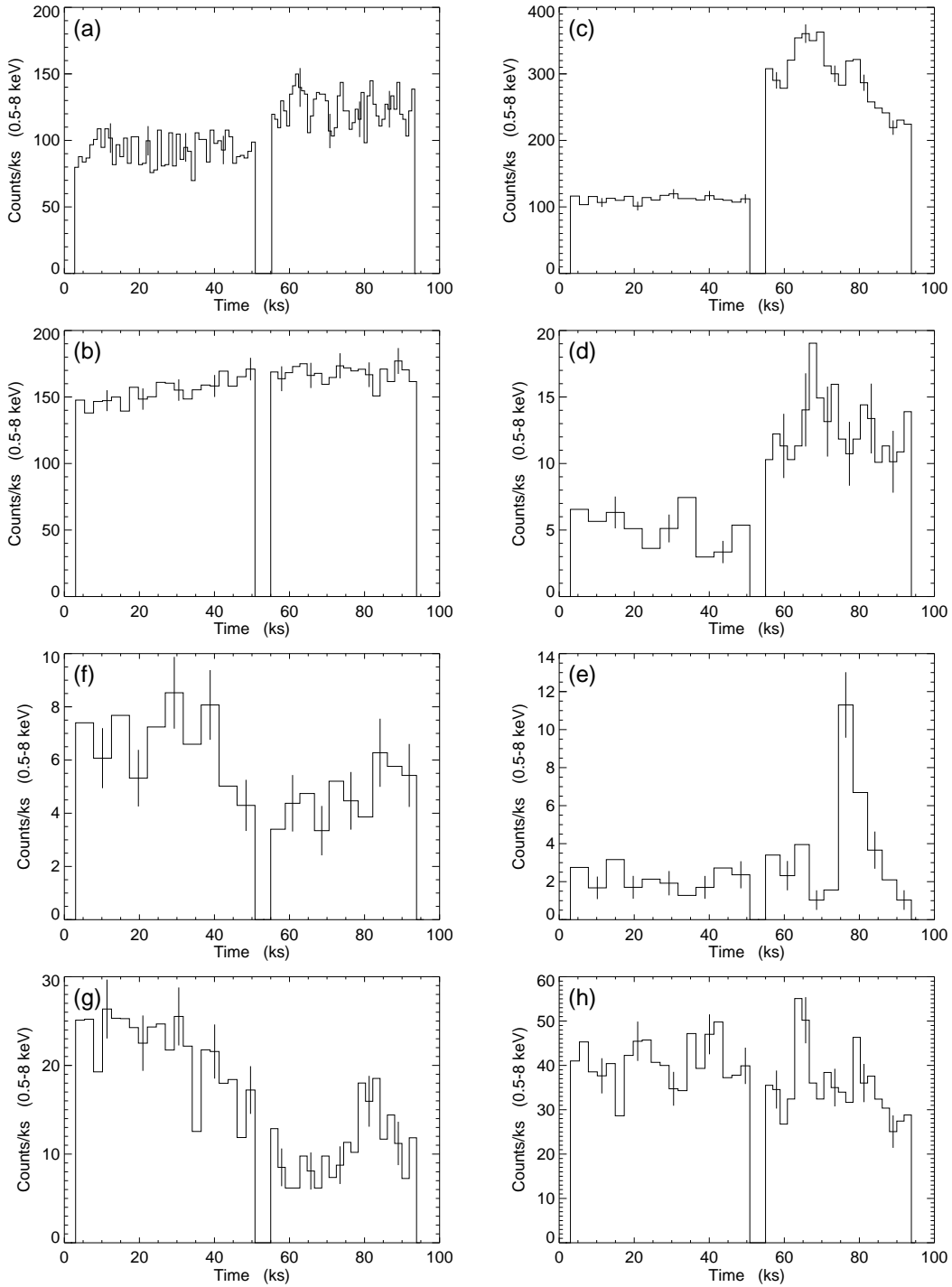


Fig. 13.— Lightcurves of massive Trapezium stars in order of decreasing mass: (a) P 1891 = θ^1 C Ori (O6, V=5.1); (b) P 1993 = θ^2 A Ori (O9.5, V=5.1); (c) P 1865 = θ^1 A Ori (O7, V=6.7); (d) P 1889 = θ^1 D Ori (B0.5, V=6.7); (e) P 2074 = NU Ori (B1, V=6.9); (f) P 2031 = θ^2 B Ori (B1, V=6.0); (g) P 1863a = θ^1 B Ori (B0, V=8.0); and (h) P 2085 = θ^2 C Ori (B4, V=8.2). Spectral types and magnitudes from SIMBAD. For graphical convenience, the two observations are plotted consecutively separated by 5 ks, though in fact they are separated by $\simeq 6$ months.

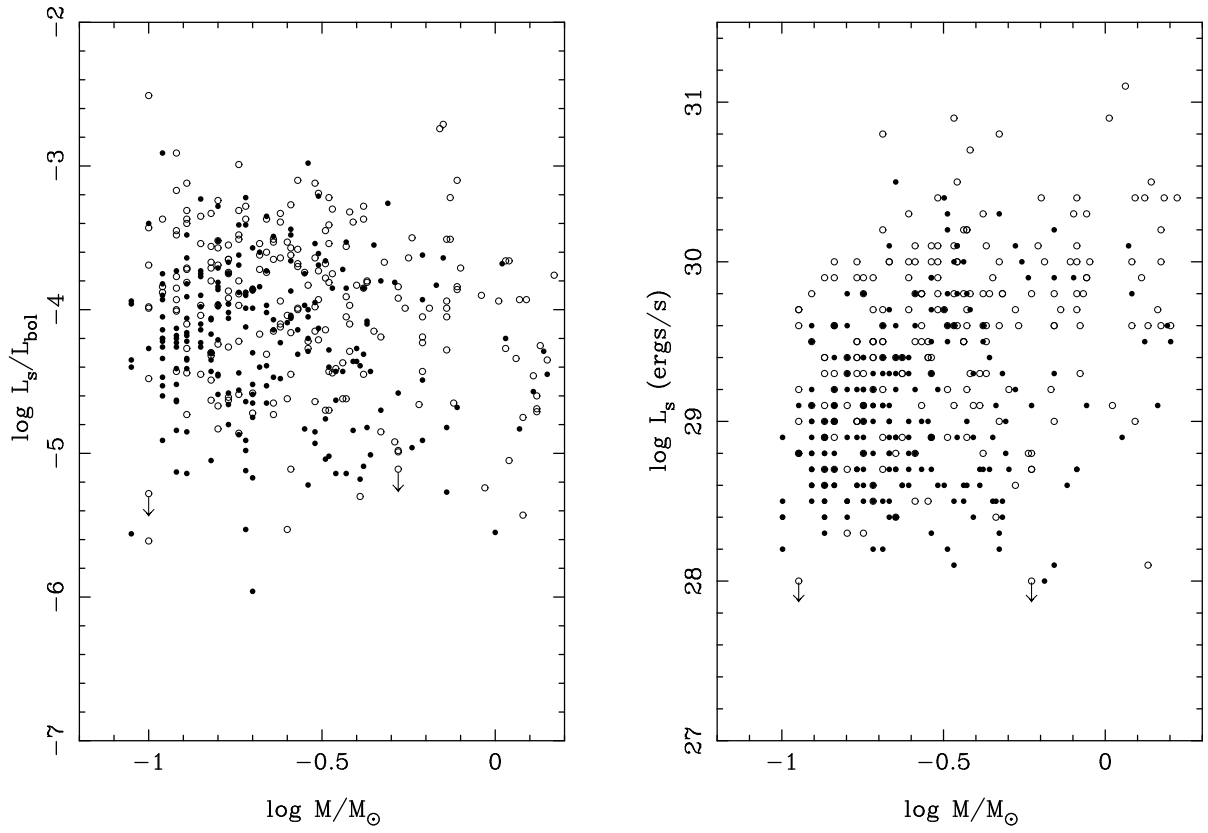


Fig. 14.— X-ray emission of low mass ONC stars: (left) soft band $\log L_s/L_{bol}$ vs. spectral type and mass; and (right) soft band $\log L_s$ vs. mass. Open circles denote stars exhibiting intra-day variability.

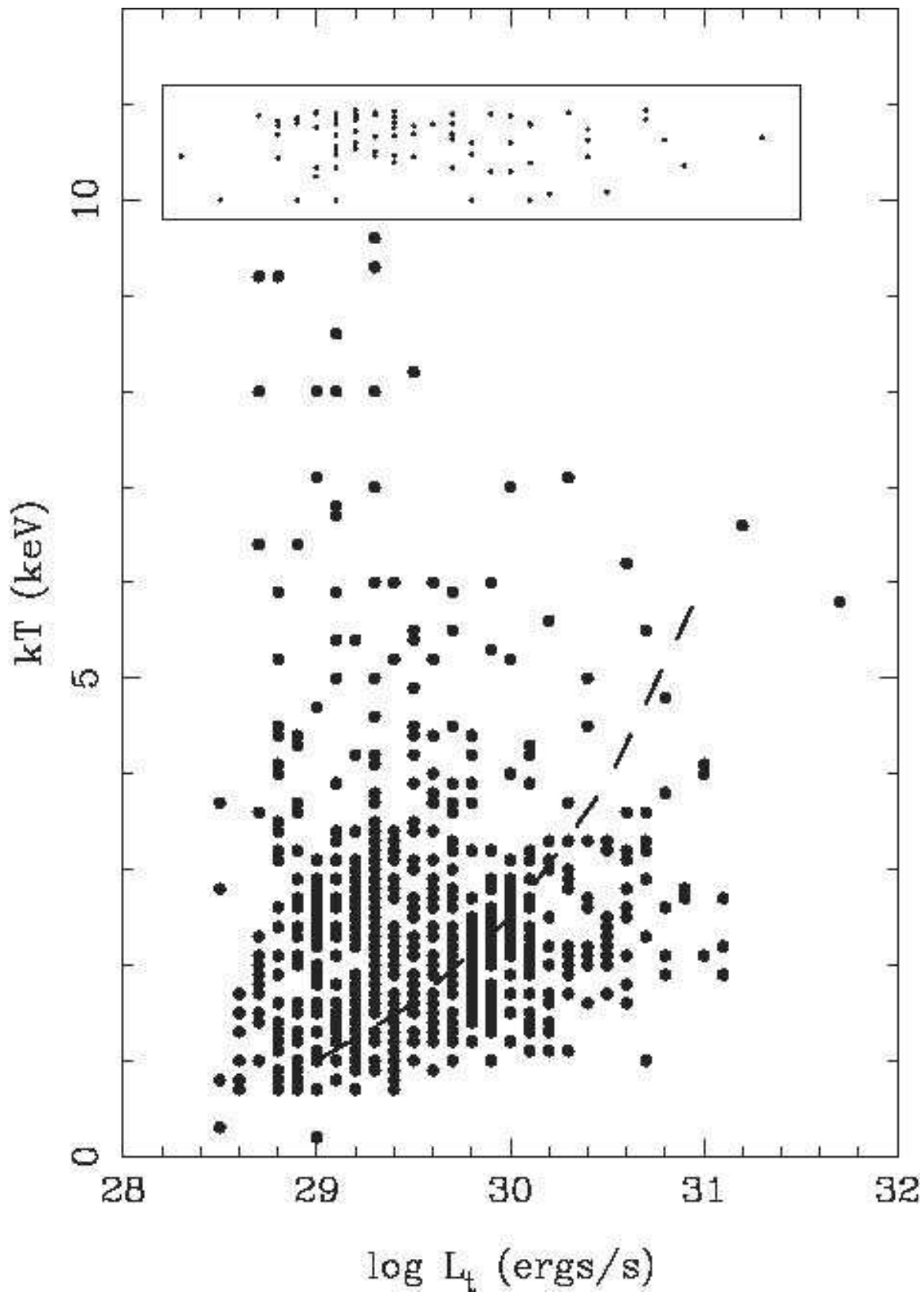


Fig. 15.— Plasma energies *vs.* full band X-ray luminosities for ONC stars. Only sources with ≥ 30 counts, masses $\leq 2 M_{\odot}$ and successful 1-temperature spectral fits are included here. The inset box shows sources with fitted plasma energies > 10 keV. The dashed curve

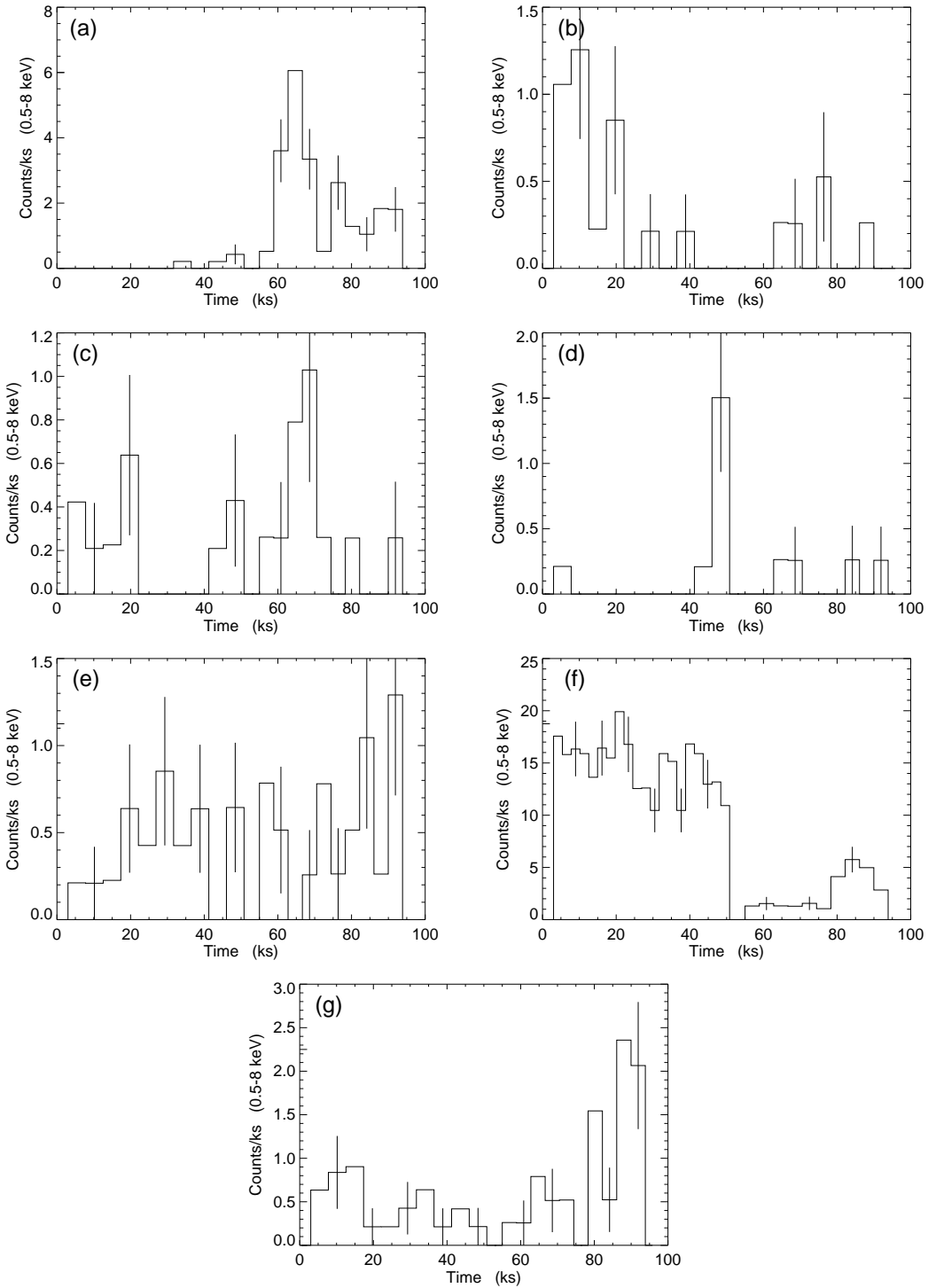


Fig. 16.— Lightcurves of very low mass ONC objects with ‘Flare’ or ‘Possible flare’ variability classifications: (a) CHS 7273 ($M \simeq 0.07 M_{\odot}$); (b) HC 741 ($M \simeq 0.02 M_{\odot}$); (c) PSH 298 ($M \simeq 0.08 M_{\odot}$); (d) PSH 116 ($M \simeq 0.04 M_{\odot}$); (e) CHS 9480 ($M \simeq 0.06 M_{\odot}$); (f) HC 756 ($M \simeq 0.07 M_{\odot}$); and (g) CHS 11663 ($M \simeq 0.03 M_{\odot}$). For graphical convenience, the two observations are plotted consecutively separated by 5 ks, though in fact they are separated by $\simeq 6$ months.

Table 1. ACIS-I observations of the Orion Nebula Cluster

<i>Chandra</i>		Exposures			Background ^a (cts arcsec ⁻²)		
ObsID	T (°C)	Start/stop times (UT)	Eff. exp. (ks)	Soft (0.5 – 2 keV)	Hard (2 – 8 keV)	Total (0.5 – 8 keV)	
18	-110	1999 Oct 12.43-13.04	45.3	0.025	0.049	0.074	
1522	-120	2000 Apr 1.73-2.20	37.5	0.014	0.027	0.042	
Merged	82.8	0.039	0.076	0.116	

^aThese values apply $\theta > 3'$ away from the bright Trapezium star θ^1 C Ori. See §2.6 for the elevated background values in the inner region of the field.

Table 2. ACIS ONC sources and stellar counterparts (sample page)

X-ray source						Stellar ID		Stellar properties										Note
Src	CXOONC J	R.A.	Dec.	θ	Prev.	ID	ϕ	$\log T_{eff}$	$\log L_{bol}$	A_V	$\log M$	$\log t$	ΔK	Other	P	P ref.		
		(J2000)		'			"	(°K)	(L_{\odot})	(mag)	(M_{\odot})	(yr)	(mag)		(day)			
367	053513.5-052757	83.80637	-5.46596	4.6	...	JW 418	0.7	
368	053513.5-053057	83.80653	-5.51605	7.6	abe	JW 421	0.8	3.643	0.51	0.51	-0.26	5.35	0.80	
369	053513.5-052355	83.80662	-5.39866	0.9	ef	HC 192	0.1	L	
370	053513.5-052400	83.80663	-5.40000	0.9	...	HC 178	0.7	L	
371	053513.6-052425	83.80669	-5.40711	1.3	ce	JW 417	0.1	3.568	-0.16	1.58	-0.48	5.72	0.56	...	7.4	H	...	
372	053513.6-052031	83.80676	-5.34212	2.9	e	PSH 47	0.4	3.535	-0.25	5.26	-0.66	5.27	-0.91	
373	053513.6-051745	83.80679	-5.29593	5.7	e	CHS 8393	1.0	
374	053513.6-051954	83.80694	-5.33188	3.5	be	JW 413	0.7	3.633	-0.84	0.00	-0.16	7.65	...	L	10.1	H	...	
375	053513.6-052846	83.80695	-5.47960	5.4	c	JW 422	0.4	6.4	S	...	
376	053513.6-052255	83.80703	-5.38221	0.8	e	
377	053513.6-051832	83.80704	-5.30914	4.9	e	CHS 8404	1.0	
378	053513.7-052135	83.80724	-5.35998	1.9	e	HC 602	0.1	L	
379	053513.7-052221	83.80732	-5.37278	1.2	e	JW 420	0.3	3.546	0.35	3.09	-0.72	4.20	...	L pd	...	43	...	
380	053513.7-053024	83.80733	-5.50682	7.1	e	JW 428	0.8	3.524	-0.39	0.65	-0.70	5.42	0.00	
381	053513.7-052217	83.80743	-5.37151	1.3	e	HC 499	0.1	
382	053513.7-051743	83.80746	-5.29550	5.7	
383	053513.8-052207	83.80754	-5.36862	1.4	e	JW 423	0.2	3.535	0.11	0.00	-0.72	4.54	1.31	pd	
384	053513.8-052202	83.80756	-5.36746	1.5	e	JW 424	0.2	
385	053513.8-051925	83.80759	-5.32377	4.0	e	JW 419	0.5	
386	053513.8-052209	83.80767	-5.36921	1.4	e	HC 525	0.2	
387	053513.8-052425	83.80781	-5.40722	1.2	e	HC 130	0.2	
388	053513.9-052229	83.80795	-5.37495	1.1	...	HC 451	0.7	FIR	id	
389	053513.9-052701	83.80803	-5.45034	3.7	e	CHS 8453	0.5	x	
390	053513.9-052319	83.80806	-5.38888	0.6	e	HC 314	0.2	pd	
391	053513.9-051853	83.80810	-5.31482	4.5	ce	JW 425	0.7	
392	053513.9-052123	83.80826	-5.35647	2.1	ae	PSH 53	0.8	
393	053514.0-052520	83.80837	-5.42229	2.0	e	PSH 93	1.1	pd	
394	053514.0-052636	83.80842	-5.44337	3.3	...	JW 434	0.9	x	
395	053514.0-052338	83.80854	-5.39400	0.7	ef	JW 431	0.1	3.513	0.22	0.68	-0.82	4.10	...	r	
396	053514.0-052012	83.80862	-5.33689	3.2	
397	053514.0-051951	83.80863	-5.33110	3.6	ace	JW 429	0.4	3.753	0.57	2.67	0.20	6.85	...	pd	
398	053514.0-052236	83.80867	-5.37682	1.0	ef	JW 432	0.0	3.513	0.31	1.94	-0.82	3.94	0.93	r	
399	053514.0-052222	83.80873	-5.37289	1.2	ef	BN Obj	0.6	FIR r	
400	053514.2-052613	83.80924	-5.43699	2.9	e	

Note. — The full table of 1075 sources is available only on-line as a machine-readable table

Notes to Table 2 (sample page)

053513.9-052229 This is one of the high-mass, high-luminosity ($L_{FIR} \sim 1000 L_{\odot}$) deeply embedded stars in the BN/KL region. Other designations include IRc 3 and “Source i”.

053513.9-052701 This source lies near a readout trail.

053514.0-052636 This faint source lies near a readout trail.

053514.0-052222 This X-ray source is associated with the Becklin-Neugebauer Object, which coincides with K-band source HC 705 and radio source B. The $1.1''$ offset between the ACIS position and radio position reported by Garmire et al. (2000) is now $0.6''$, consistent with a true coincidence.

Table 3. X-ray properties of ONC sources (sample, 1075 total)

X-ray extraction						Variability			Spectrum				Luminosity				Note
Src	CXOONC	C_{xtr}	B_{xtr}	R_{xtr}	f_{PSF}	CR_1	CR_2	Var Cl	$\log N_H$	kT	kT_1/kT_2	Feat	$\log L_s$	$\log L_h$	$\log L_t$	$\log L_c$	
		(counts)		($''$)		(ct ks $^{-1}$)			(cm $^{-2}$)	(keV)			(erg s $^{-1}$)				
367	053513.5-052757	17	4	3.2	0.95	0.2	0.2	Const	<20.0	2.9	28.3	...	f s
368	053513.5-053057	1350	15	6.5	0.92	11.6	24.0	Flare	21.5	2.6	30.1	30.2	30.5	30.6	v
369	053513.5-052355	340	3	1.8	0.92	7.3	0.7	Flare	22.7	5.0	28.7	30.4	30.4	30.8	v
370	053513.5-052400	21	3	1.8	0.93	0.4	0.1	LT Var	22.4	1.8	28.9	...	f
371	053513.6-052425	2086	5	2.3	0.96	9.9	45.1	Pos fl	21.3	2.6	30.3	30.3	30.6	30.7	...
372	053513.6-052031	51	2	2.2	0.95	0.7	0.4	Const	21.5	1.8	28.8	28.7	29.0	29.2	...
373	053513.6-051745	37	1	1.7	0.54	0.9	0.5	Const	22.6	1.3	<28.0	29.0	29.2	30.1	...
374	053513.6-051954	1178	6	4.0	0.97	21.6	5.2	Flare	22.1	2.5	30.0	30.5	30.7	31.0	v
375	053513.6-052846	108	6	4.1	0.94	0.1	2.8	LT Var	21.6	4.0	29.1	29.5	29.6	29.8	...
376	053513.6-052255	28	4	1.8	0.93	0.5	0.1	LT Var	22.7	1.9	29.0	...	f
377	053513.6-051832	32	5	3.6	0.95	0.6	0.0	LT Var	20.1	3.6	28.5	28.5	28.8	28.8	...
378	053513.7-052135	146	2	1.9	0.93	1.8	1.9	Const	22.7	2.3	28.5	29.9	29.9	30.5	...
379	053513.7-052221	30	3	1.8	0.94	0.4	0.3	Const	21.3	6.4	28.4	28.7	28.9	29.0	...
380	053513.7-053024	151	14	6.3	0.95	1.4	2.2	Const	20.7	1.3	29.1	28.6	29.3	29.3	...
381	053513.7-052217	26	3	1.8	0.93	0.3	0.4	Const	22.4	2.8	29.0	...	f
382	053513.7-051743	10	0	1.1	0.34	0.6	0.0	Const	22.4	>10	28.8	...	f
383	053513.8-052207	634	0	1.0	0.89	8.2	8.6	Const	21.5	2.3	29.7	29.9	30.1	30.3	...
384	053513.8-052202	15	2	1.9	0.94	0.3	0.1	Const	22.0	3.0	28.6	...	f
385	053513.8-051925	18	2	2.5	0.93	0.3	0.1	Const	<20.0	1.9	28.5	...	f
386	053513.8-052209	137	0	1.0	0.87	1.1	2.6	Pos fl	22.2	1.7	29.0	29.5	29.6	30.1	...
387	053513.8-052425	93	3	1.8	0.93	1.4	0.9	Pos fl	2/>10	...	28.4	29.5	29.6
388	053513.9-052229	13	3	1.8	0.92	0.1	0.3	Const	22.8	2.8	28.9	...	f
389	053513.9-052701	42	1	1.2	0.68	0.9	0.6	Const	22.2	>10	28.1	29.3	29.3	29.5	...
390	053513.9-052319	36	5	1.9	0.95	0.5	0.4	Const	<20.0	4.5	28.4	28.6	28.8	28.8	...
391	053513.9-051853	87	4	3.3	0.94	1.1	0.9	Const	21.7	2.9	28.9	29.2	29.4	29.5	...
392	053513.9-052123	250	2	1.9	0.93	2.7	3.7	Const	22.2	3.1	29.2	29.9	30.0	30.3	...
393	053514.0-052520	41	2	1.9	0.96	0.4	0.5	Const	<20.0	1.4	28.6	28.1	28.7	28.7	...
394	053514.0-052636	9	2	2.6	0.96	5.0	7.1	LT Var	<20.0	3.0	27.9	...	f s
395	053514.0-052338	359	4	1.9	0.96	3.9	4.9	Pos fl	21.0	1.4	...	*	29.5	29.1	29.7	29.8	...
396	053514.0-052012	25	2	2.3	0.93	0.1	0.6	Flare	23.1	1.1	29.2	...	f v
397	053514.0-051951	485	2	2.5	0.96	5.0	7.2	LT Var	<20.0	1.5	...	*	29.8	29.3	29.9	29.9	...
398	053514.0-052236	218	3	1.8	0.96	1.2	4.4	Pos fl	21.3	1.3	29.4	29.0	29.6	29.8	...
399	053514.0-052222	45	3	1.8	0.92	0.5	0.6	Const	22.6	>10	<28.0	29.4	29.4	29.6	...
400	053514.2-052613	17	2	2.1	0.93	0.2	0.2	Const	22.6	2.8	28.8	...	f

Note. — The full table of 1075 sources is available only on-line as a machine-readable table

Notes to Table 3 (sample page)

053513.5-052757 The spectral fit does not account for most of the emission below 1 keV.

053513.5-053057 Flares seen during both observations. First, the source rose from $CR_q \sim 0.005$ cts s⁻¹ to $CR_p = 0.018$ cts s⁻¹, remaining high for > 6 hours. Second, a short-duration (2 hours) event is seen with $CR_p = 0.037$ cts s⁻¹ superposed on a quiescent level $CR_q = 0.02$ cts s⁻¹.

053513.5-052355 High amplitude flare towards the end of the observation with $CR_q = 0.003$ cts s⁻¹ rising to $CR_p > 0.03$ cts s⁻¹ in $\simeq 3$ hours.

053513.6-051954 A very short flare with $CR_p = 0.03$ cts s⁻¹ and duration < 1 hour appears to be superposed on the > 12 hour decay of a larger flare.

053514.0-052636 The spectral model was obtained by fixing the plasma energy at 3 keV.

053514.0-052012 The observation begins during a flare with $CR_p > 0.0024$ cts s⁻¹ and decays to $CR_q \sim 0.0003$ cts s⁻¹ over 2 hours.

053514.2-052004 Flare lasting several hours with $CR_p \simeq 0.0055$ cts s⁻¹ follows a quiescent level $CR_q \simeq 0.0015$ cts s⁻¹.

053514.2-052304 The spectral fit for this source is poor.

053514.3-052308 The spectra fit may have overestimated the soft absorption for this source.

053514.3-052317 Dramatic flare at the end of an observation from $CR_q = 0.002$ cts s⁻¹ to $CR_p > 0.016$ cts s⁻¹ with a rise of 3 hours. The spectral fit has greatly overestimated the soft band absorption for this source.

053514.3-052232 The emission rises from $CR_q \sim 0.002$ cts s⁻¹ to $CR_p \simeq 0.008$ cts s⁻¹ with rise time 2 hours. The broad-band spectrum of the source is unusual with a nearly flat distribution across the *Chandra* band. It can be interpreted as a very hard component with high absorption ($\log N_H \sim 22.5$ cm⁻²) plus a soft unabsorbed component. The luminosity of the latter component is underestimated in the spectral fit and tabulated L_s value.

053514.3-052219 The spectral model was obtained by fixing the plasma energy at 3 keV.

053514.3-052333 Rise to $CR_p \simeq 0.009$ cts s⁻¹ from $CR_q \simeq 0.002$ cts s⁻¹ over several hours.

053514.4-052903 A hard spectral component not included in the spectral fit above 2 keV may be present.

Table 4. X-ray sources without stellar identifications

Src	CXOONC	C_{xtr}	Var Cl	$\log N_H$ (cm^{-2})	kT (keV)	$\log L_t$ (erg s^{-1})	Suggested class
3	053439.6-052458	45	Const	21.6	>10	29.4	ONC
24	053446.8-052342	29	Const	<20.0	>10	28.7	ONC
27	053447.9-052054	35	Const	22.6	>10	29.1	Embd/Bk
35	053450.2-052323	36	Const	22.0	>10	29.2	Embd/Bk
54	053452.9-052617	30	Const	21.4	>10	28.9	ONC
57	053453.4-052650	44	Const	21.7	>10	29.1	ONC
58	053453.6-051354	43	Const	...	5/>10	29.2	ONC
71	053455.5-051529	87	Const	...	0.1/>10	29.4	ONC
73	053455.8-052337	44	Const	22.6	>10	29.5	Embd/Bk
79	053456.2-052228	123	Const	22.3	>10	29.8	Embd/Bk
86	053457.0-051500	59	LT Var	...	0.1/>10	29.0	ONC
89	053457.7-052223	23	Const	22.1	>10	29.0	Embd/Bk
100	053459.4-052615	27	Const	21.9	>10	29.0	ONC
105	053500.1-052549	13	Const	22.3	2.7	28.6	Embd/Bk
122	053501.7-052512	21	Const	22.3	>10	29.0	Embd/Bk
141	053503.8-052941	170	Pos fl	22.2	>10	29.9	Embd/Bk
151	053504.4-051951	28	Const	22.0	>10	29.0	Embd/Bk
186	053506.3-052335	16	Const	22.4	>10	29.1	Embd/Bk
193	053506.5-052734	10	Const	22.1	4.2	28.3	Embd/Bk
195	053506.6-051622	31	LT Var	22.3	>10	29.0	Embd/Bk
201	053507.3-052253	13	Const	23.2	1.8	28.9	Embd/Bk
202	053507.3-052547	14	Const	21.1	0.7	28.2	ONC
206	053507.4-052301	8	Const	22.0	3.0	28.3	Embd/Bk
212	053507.8-052029	14	Const	23.2	2.1	28.8	Embd/Bk
227	053508.6-052022	23	Pos fl	22.0	2.9	28.8	Embd/Bk
250	053510.1-052004	11	Const	23.0	0.9	28.6	Embd/Bk
258	053510.4-052223	28	Pos fl	22.5	>10	29.3	Embd/Bk
288	053511.6-052729	57	Pos fl	22.1	4.1	29.3	Embd/Bk
312	053512.2-052424	26	LT Var	23.1	6.7	29.4	Embd/Bk
315	053512.3-052241	12	Const	22.3	1.1	28.4	OMC 1
324	053512.6-052205	11	Const	22.5	1.4	28.6	Embd/Bk
336	053512.9-052351	17	Const	<20.0	>10	28.6	ONC
337	053512.9-052354	27	LT Var	23.2	>10	29.5	OMC 1S
351 ^a	053513.2-052254	121	LT Var	23.4	>10	30.2	OMC 1
354	053513.2-052239	74	Pos fl	22.8	>10	30.0	OMC 1
362	053513.4-052354	5	Const	22.0	3.0	28.2	OMC 1S
376	053513.6-052255	28	LT Var	22.7	1.9	29.0	OMC 1
382	053513.7-051743	10	Const	22.4	>10	28.4	Embd/Bk
396	053514.0-052012	25	Flare	23.1	1.1	29.2	Embd/Bk
400	053514.2-052613	17	Const	22.6	2.8	28.8	Embd/Bk
406	053514.3-052317	221	Flare	23.3	>10	30.3	Embd/Bk
410	053514.3-052219	9	Const	23.1	3.0	28.6	OMC 1
417	053514.5-052630	22	LT Var	23.2	1.1	29.2	Embd/Bk
419	053514.5-052315	70	Const	...	0.3/3	29.5	ONC
422	053514.5-052407	131	Flare	23.2	>10	30.1	OMC 1S
428	053514.6-052210	74	LT Var	...	4/>10	29.9	OMC 1
431	053514.7-052412	50	Pos fl	...	0.7/>10	29.7	OMC 1S

Table 4—Continued

Src	CXOONC	C_{xtr}	Var Cl	$\log N_H$ (cm^{-2})	kT (keV)	$\log L_t$ (erg s^{-1})	Suggested class
435	053514.8-052057	11	Const	22.0	4.9	28.5	OMC 1N
436	053514.8-052406	94	LT Var	22.7	>10	29.8	OMC 1S
442	053514.9-052225	625	Pos fl	23.1	>10	30.7	OMC 1
450	053515.0-052336	9	Const	<20.0	3.0	28.2	ONC
453 ^b	053515.1-052229	35	Const	...	0.1/>10	29.3	OMC 1
454	053515.1-052238	8	Const	<20.0	3.0	28.3	ONC
455	053515.1-052201	41	Const	20.6	1.9	28.8	ONC
456	053515.1-052217	222	Pos fl	...	0.5/6	30.2	OMC 1
469	053515.3-052218	71	Pos fl	...	0.9/>10	29.8	OMC 1
476	053515.4-051934	18	Const	22.1	>10	28.9	OMC 1N
483	053515.6-052126	378	Const	23.3	>10	30.5	OMC 1N
494	053515.7-051808	24	LT Var	22.3	2.1	29.0	Embd/Bk
500	053515.8-052318	171	Const	20.5	2.0	29.4	ONC
509 ^c	053515.9-052319	39	Const	<20.0	2.0	28.7	ONC
515	053516.0-051944	38	Const	23.1	>10	29.5	OMC 1N
532	053516.2-052306	11	Const	<20.0	>10	28.4	ONC
546	053516.5-052054	12	Const	22.6	>10	28.8	OMC 1N
579	053517.1-052129	64	LT Var	21.5	3.9	29.1	ONC
580	053517.1-051813	53	Const	22.5	4.2	29.3	OMC 1N
587	053517.3-052051	8	Const	22.6	3.0	28.5	OMC 1N
595	053517.4-052315	17	Const	<20.0	0.8	28.4	ONC
610	053517.7-051833	317	LT Var	22.4	2.5	29.9	OMC 1N
635	053518.0-052056	17	Const	22.9	2.3	28.9	Embd/Bk
660	053518.5-052232	17	Const	<20.0	5.1	28.6	ONC
665	053518.7-051905	597	Flare	23.2	>10	30.7	OMC 1N
683	053519.1-052112	16	Const	22.2	>10	29.1	Embd/Bk
686	053519.1-052118	28	Pos fl	23.5	0.9	29.3	Embd/Bk
701	053519.7-052110	22	Const	22.8	>10	29.3	Embd/Bk
702	053519.7-052155	9	Const	22.0	3.0	28.3	Embd/Bk
715	053520.0-052038	131	LT Var	22.9	1.4	29.8	Embd/Bk
756	053520.9-052234	36	Const	22.6	3.4	29.3	Embd/Bk
776	053521.5-051752	17	Const	22.0	>10	28.6	Embd/Bk
779	053521.6-051952	57	Flare	23.1	>10	29.7	Embd/Bk
839	053523.4-051957	44	Pos fl	23.0	1.2	29.2	Embd/Bk
842	053523.4-052001	72	Pos fl	22.4	1.4	29.1	Embd/Bk
862	053524.0-052125	10	Const	22.6	1.1	28.4	Embd/Bk
872	053524.3-052206	12	Const	22.5	>10	28.6	Embd/Bk
881	053524.6-052759	3703	Const	22.2	>10	31.3	Embd/Bk
888	053525.0-052326	26	Const	22.7	1.6	29.0	Embd/Bk
896	053525.3-052720	23	Const	22.0	>10	28.9	Embd/Bk
899	053525.4-052012	24	Const	23.2	1.2	29.0	Embd/Bk
902	053525.5-052136	282	Const	21.6	2.2	29.7	ONC
915	053526.3-051950	19	Const	22.8	2.4	28.9	Embd/Bk
935	053527.6-052038	14	Const	22.0	5.9	28.6	Embd/Bk
966	053529.8-052859	64	Const	22.1	>10	29.4	Embd/Bk
1006	053532.4-052822	52	LT Var	21.9	>10	29.2	ONC
1014	053533.3-051508	95	Const	21.9	>10	29.9	ONC

Table 4—Continued

Src	CXOONC	C_{xtr}	Var Cl	$\log N_H$ (cm^{-2})	kT (keV)	$\log L_t$ (erg s^{-1})	Suggested class
1015	053533.4-052702	34	Const	22.3	5.0	29.1	Embd/Bk
1016	053533.5-051651	40	Const	22.2	>10	29.3	Embd/Bk
1031	053536.5-051628	58	LT Var	22.1	>10	28.8	Embd/Bk
1043	053539.2-052856	45	LT Var	21.8	>10	28.8	ONC
1045	053540.1-053016	102	LT Var	21.9	>10	29.4	ONC
1050	053541.7-052015	40	Const	22.3	>10	29.1	Embd/Bk
1059	053543.7-052400	25	Const	21.8	>10	28.7	ONC

^aRadio source Q, 2.5 mJy at 2 cm (Felli et al. 1993)

^bThis X-ray source lies 1.5'' from IRC 14, a luminous mid-infrared member of the OMC 1 cluster (Gezari et al. 1998).

^cThis X-ray source coincides with a SIMBAD listing for Parenago 1867 ($V=15.8$). However, examination of the original charts of Parenago (1954) indicates that the SIMBAD position is probably incorrect: Parenago 1867 corresponds to HC 304 $\simeq 3''$ to the south. The X-ray position is resolvable from other stars in the region and has no counterpart with $V < 20$ or $K < 18$.

Table 5. High- and intermediate-mass ONC stars

Src	CXOONC	Optical properties						X-ray properties						
		ID	Name	V (mag)	Sp.Ty.	$\log L_{bol}$ (L_{\odot})	$\log M$ (M_{\odot})	C_{xtr}	Var Cl	$\log N_H$ (cm^{-2})	kT (keV)	$\log L_s$ (erg s^{-1})	$\log L_t$	$\log L_t/L_{bol}$
542	053516.4-052322	P 1891	θ^1 C Ori	5.13	O6 pe	5.38	1.65	21596	LT Var	...	0.3/2	33.2	33.3	-5.8
828	053522.8-052457	P 1993	θ^2 A Ori	5.08	O9.5 Vpe	5.02	1.49	16525	Flare	...	0.2/6	31.2	31.6	-7.4
498	053515.8-052314	P 1865	θ^1 A Ori	6.73	O7	4.49	1.27	13676	LT Var	...	1.0/5	31.0	31.5	-7.1
584	053517.2-052316	P 1889	θ^1 D Ori	6.71	B0.5 Vp	4.33	1.21	724	Pos fl	20.47	0.6	30.1	30.1	-7.8
996	053531.4-051602	P 2074	NU Ori	6.87	B1 V	4.33	1.21	490	Const	21.54	7.0	28.7	29.3	-9.2
916	053526.4-052500	P 2031	θ^2 B Ori	5.02	B1 V	3.96	1.08	242	Flare	21.20	1.4	29.3	29.5	-8.2
...	...	P 1772	LP Ori	8.43	B1.5 Vp	3.26	0.85	<28.4	<28.7	<-8.5
519	053516.0-052307	P 1863a	BM Ori	7.96	B0.5	3.23	0.84	1427	Pos fl	21.48	2.5	30.0	30.4	-6.8
746	053520.7-052144	JW 660	V1230 Ori	9.66	B8 IV	3.06	0.79	6020	LT Var	21.64	2.5	30.7	31.1	-6.0
728	053520.2-052057	JW 640	TU Ori	...	G9	2.26	0.70	1895	Pos fl	21.80	2.2	30.2	30.6	-5.7
995	053531.4-052516	P 2085	θ^2 C Ori	8.24	B4 V	2.86	0.70	3261	Flare	...	0.1/2	30.5	30.7	-5.9
495	053515.7-052309	P 1864	...	11.10	...	2.48	0.63	14968	Const	...	0.9/>10	30.9	31.7	-5.1
164	053505.3-051449	JW 260	V1230 Ori	11.07	G5	1.83	0.61	1833	Const	21.44	2.1	30.5	30.8	-4.9
1046	053540.3-051728	JW 945	...	14.60	B6	2.35	0.61	484	Pos fl	21.94	2.5	29.5	30.1	-6.4
...	...	JW 108	...	10.27	A2 Vp	1.98	0.55	<28.6	<28.9	<-7.0
670	053518.8-051728	JW 599	A9	1.84	0.54	23	Const	20.96	3.6	...	28.6	-7.3
291	053511.6-051657	JW 364	LT Ori	...	K0	1.37	0.50	2883	Pos fl	21.73	1.8	30.4	30.8	-4.5
508	053515.9-052349	JW 499	θ^1 E Ori	13.79	K0	1.30	0.50	3965	Flare	21.70	6.6	30.6	31.1	-4.3
1004	053532.3-053111	JW 887	...	11.77	...	1.38	0.50	1319	LT Var	...	0.2/1	30.2	30.3	-4.8
663	053518.6-052033	JW 595	MV Ori	1.26	0.46	3504	LT Var	21.73	2.6	30.5	30.9	-4.4
70	053455.2-053022	JW 153	...	9.01	B9	1.86	0.46	93	Pos fl	20.29	1.0	29.0	29.1	-6.4
651	053518.3-052237	JW 589	V1229 Ori	13.38	M0	1.25	0.45	5352	Pos fl	...	0.9/4	30.8	31.2	-4.0
914	053526.3-052540	JW 799	AK Ori	...	G5	1.16	0.44	4161	Flare	...	0.8/3	30.5	31.0	-4.2
484	053515.6-052256	JW 479	V348 Ori	...	K0	1.18	0.43	5954	LT Var	21.50	2.5	30.7	31.1	-4.1
...	...	P 1892	...	11.50	B8	1.85	0.45	<28.9	<29.2	<-6.5
103	053500.0-052515	JW 197	KS Ori	10.19	A0	1.66	0.40	665	LT Var	20.74	1.6	29.8	30.0	-5.4
910	053526.1-052737	JW 795	V1232 Ori	11.59	K0	1.03	0.40	7891	Flare	21.98	0.2/2	30.9	31.1	-3.7
347	053513.1-052455	JW 401	K1	1.06	0.40	94	Const	21.80	2.6	28.8	29.3	-5.9
...	...	JW 531	MR Ori	10.30	A2 Vp	1.68	0.42	<28.2	<28.5	<-7.1
1051	053541.9-052813	JW 959	AN Ori	...	K11 Ve	1.05	0.39	8141	Pos fl	...	0.8/3	31.0	31.2	-3.7
81	053456.4-053136	JW 165	KO Ori	1.47	0.38	1256	Const	20.91	1.7	30.5	30.7	-4.6
461	053515.2-052256	JW 468	...	13.22	G7	0.97	0.38	5401	Pos fl	21.39	2.1	30.7	31.0	-3.9
952	053528.4-052621	JW 831	V1073 Ori	9.52	B9.5 V	1.52	0.38	125	Const	<20.0	1.0	29.1	29.2	-6.0
261	053510.4-052618	JW 348	LR Ori	11.90	...	0.94	0.36	2499	Pos fl	21.40	1.8	30.4	30.7	-4.1

Table 5—Continued

Src	CXOONC	Optical properties						X-ray properties						
		ID	Name	V (mag)	Sp.Ty.	$\log L_{bol}$ (L_{\odot})	$\log M$ (M_{\odot})	C_{xtr}	Var Cl	$\log N_H$ (cm^{-2})	kT (keV)	$\log L_s$ (erg s^{-1})	$\log L_t$	$\log L_t/L_{bol}$
760	053521.0-052349	JW 669	V1399 Ori	12.30	...	1.15	0.36	7476	Pos fl	...	0.8/3	30.8	31.2	-3.9
722	053520.1-052639	JW 641	V1338 Ori	0.93	0.36	4954	Flare	21.20	2.8	30.6	31.0	-3.9
104	053500.1-052301	JW 193	KR Ori	...	K0 e	0.89	0.35	844	Const	20.14	2.0	29.8	30.1	-4.6
173	053505.6-052519	JW 273	LL Ori	10.70	K0 e	1.15	0.32	2449	Pos fl	...	0.7/3	30.4	30.6	-4.4
320	053512.5-052343	JW 385	LV Ori	12.10	...	1.01	0.32	413	Pos fl	...	0.6/2	28.7	28.5	-5.9
993	053531.4-051533	JW 866	V1294 Ori	...	K1 IV	1.01	0.32	1611	Pos fl	21.44	2.0	30.4	30.7	-4.2
576	053517.0-052334	JW 538	K1	0.99	0.32	1830	Pos fl	22.23	3.7	30.0	31.0	-4.5
513	053516.0-052353	JW 503	AC Ori	12.50	...	1.14	0.30	302	LT Var	22.41	4.1	29.0	30.1	-5.7
573	053517.0-052233	JW 536	V1333 Ori	14.60	K1	0.78	0.28	3555	Pos fl	21.45	2.1	30.5	30.8	-3.9
6	053439.8-052642	JW 46	...	12.57	K3e var	0.75	0.27	1674	LT Var	21.11	1.3	30.5	30.6	-3.8
14	053443.3-051828	JW 64	...	11.13	F2 IV	1.00	0.27	608	Const	21.32	2.8	30.1	30.5	-4.5
853	053523.7-053048	JW 747	V358 Ori	12.20	G8 V	0.72	0.26	5651	Pos fl	...	0.8/2	30.8	31.0	-3.5
...	...	JW 608	...	11.89	A5	0.98	0.25	<28.2	<28.5	<-6.4
131	053502.4-051547	JW 221	V403 Ori	1.44	0.24	10505	Flare	...	0.9/3	30.9	31.4	-4.1
17	053445.1-052503	JW 75	K2	0.92	0.22	9461	Flare	...	0.9/3	31.0	31.3	-3.5
133	053502.9-053001	JW 232	KZ Ori	0.84	0.20	2544	Const	21.31	1.6	30.4	30.6	-4.0
397	053514.0-051951	JW 429	G	0.57	0.20	485	LT Var	<20.0	1.5	29.7	29.8	-4.4
77	053455.9-052312	JW 157	KM Ori	...	K1	1.22	0.18	16231	Flare	...	0.8/3	31.2	31.5	-3.6
769	053521.2-052457	JW 678	V377 Ori	12.80	...	0.58	0.17	2580	Flare	21.09	2.1	30.4	30.6	-3.8

Table 6. X-ray detections of very low mass ONC objects

Src	CXOONC	Optical-IR properties					X-ray properties					
		ID	K (mag)	$H - K$ (mag)	M_K (mag)	Mass (M_\odot)	C_{xtr}	Var Cl	$\log N_H$ (cm^{-2})	kT (keV)	$\log L_t$ (erg s^{-1})	$\log L_t/L_{bol}$
34	053450.1-051959	JW 110	13.82	0.40	5.39	0.07	25	Const	...	0.3/>10	28.4	-3.7
55	053453.1-052400	CHS 6221	13.76	0.43	5.28	0.07	41	Const	20.6	2.3	28.7	-3.4
56	053453.3-052627	CHS 6210	13.70	0.44	5.20	0.07	30	Const	...	0.2/5	29.0	-3.2
65	053454.5-052300	CHS 6351	13.86	0.42	5.40	0.07	30	Const	<20.0	>10	28.8	-3.3
74	053455.9-053113	JW 159	13.24	0.14	4.88	0.09	57	Const	<20.0	1.4	29.2	-3.1
112	053501.2-052144	JW 205	11.68	0.75	2.42	0.65 ^a	26	Const	<20.0	3.6	28.6	-4.7
142	053503.9-052809	CHS 7273	14.05	0.53	5.43	0.07	91	Pos fl	22.4	2.7	29.5	-2.6
169	053505.4-052230	H 5096	13.31	0.81	4.20	0.13 ^b	15	Const	20.9	>10	28.7	-3.9
196*	053506.6-052243	HC 741	16.26	...	<7.90	>0.02	23	Pos fl	22.6	2.4	28.9	<-2.2
197*	053506.8-052209	PSH 298	13.66	0.45	5.15	0.08	22	Pos fl	20.8	0.4	28.5	-3.7
198*	053506.9-052501	HC 64	14.52	0.73	5.63	0.06	8	Const	22.0	3.0	28.3	-3.7
199	053507.1-051828	H 5064	13.44	0.31	5.08	0.08 ^c	17	Const	<20.0	6.1	28.3	-3.9
241*	053509.7-052152	HC 748	16.22	1.96	5.61	0.06	10	Const	22.3	2.6	28.5	-3.5
309*	053512.1-052447	HC 95	15.92	...	<7.56	>0.03	16	Const	22.8	1.7	28.9	<-2.3
339	053513.0-051547	CHS 8315	13.77	0.48	5.22	0.07	52	LT Var	<20.0	5.2	28.8	-3.4
413	053514.4-052903	JW 446	13.56	-0.04	5.20	0.07	42	LT Var	<20.0	0.8	28.5	-3.7
503*	053515.8-052431	PSH 116	12.55	0.87	3.21	0.35 ^d	13	Pos fl	23.3	1.5	28.8	-4.2
561*	053516.8-052307	PSH 153	13.19	0.12	4.83	0.08	37	Const	<20.0	9.2	28.8	-3.5
643*	053518.2-052346	PSH 215	14.46	0.71	5.61	0.06	19	Const	<20.0	>10	28.5	-3.5
755	053520.9-053005	CHS 9480	14.45	0.57	5.77	0.06	116	Flare	21.2	2.7	29.2	-2.7
774	053521.4-051710	CHS 9558	13.99	...	<5.63	>0.06	143	LT Var	22.8	1.6	29.9	<-2.1
806	053522.1-051857	CHS 9657	13.96	...	<5.60	>0.06	32	Const	21.7	>10	28.9	<-3.1
838	053523.4-052038	CHS 9819	14.57	...	<6.21	>0.04	11	Const	22.7	1.6	28.6	<-3.2
852	053523.7-052804	H 5131	13.75	...	<5.39	>0.07	20	Const	...	0.2/>10	28.6	<-3.5
869	053524.3-052647	CHS 9924	13.83	0.45	5.33	0.07	17	Const	<20.0	1.2	28.2	-3.9
873*	053524.4-052440	HC 756	14.29	0.77	5.33	0.07	790	Pos fl	22.1	3.3	30.4	-2.7
886*	053525.0-052438	HC 114	13.94	0.49	5.37	0.07	16	Const	<20.0	1.1	28.2	-3.9
936	053527.6-053109	CHS 10299	14.61	0.39	6.18	0.05	55	LT Var	21.9	>10	29.1	-2.7
1047	053540.8-052707	CHS 11663	14.97	0.32	<6.61	>0.03	56	Pos fl	...	0.2/>10	28.9	<-2.7
1052	053542.1-052005	JW 958	13.41	0.24	5.05	0.08	66	Const	...	0.2/>10	29.0	-3.2

^aSpectroscopic mass estimate of 0.04 M_\odot
^bSpectroscopic mass estimate of 0.05 M_\odot
^cSpectroscopic mass estimate of 0.07 M_\odot
^dSpectroscopic mass estimate of 0.04 M_\odot